Universidade de Aveiro Departamento de Física,
2020

SÍLVIA MARIA GOUVEIA RODRIGUES

MODELAÇÃO E SIMULAÇÃO DE FENÓMENOS NÃO-LINEARES EM FIBRAS ÓPTICAS MICROESTRUTURADAS

Universidade de Aveiro Departamento de Física,
2020

SÍLVIA MARIA GOUVEIA RODRIGUES

MODELLING AND SIMULATION OF NONLINEAR PHENOMENA IN MICROSTRUCTURED OPTICAL FIBRES

Universidade de Aveiro Departamento de Física,
2020

SÍLVIA MARIA GOUVEIA RODRIGUES

MODELLING AND SIMULATION OF NONLINEAR PHENOMENA IN MICROSTRUCTURED OPTICAL FIBRES

Dissertação apresentada à Universidade de Aveiro para cumprimento dos requisitos necessários à obtenção do grau de Doutor em Física, realizada sob a orientação científica do Doutor Mário F.S. Ferreira, Professor associado com agregação do Departamento de Física da Universidade de Aveiro e da Doutora Margarida M.R.V. Facão, Professora auxiliar do Departamento de Física da Universidade de Aveiro.

Este trabalho foi financiado por fundos nacionais pela FCT - Fundação para a Ciência e a Tecnologia, através dos projectos: UID/EEA/50014/2019 e UID/CTM/50025/2019, e através das bolsas de investigação: PD/BI/52527/2014, PD/BD/108650/2015, e "BI-14 (7409/2018)".

o júri

presidente

Doutor **João Manuel Nunes Torrão**

Professor Catedrático, Universidade de Aveiro

vogais

Doutor **João Lemos Pinto**

Professor Catedrático, Universidade de Aveiro

Doutor **Michael Scott Belsley**

Professor Associado c/ Agregação, Universidade do Minho

Doutor **José Manuel Marques Martins de Almeida**

Professor Associado c/ Agregação, Universidade de Trás-os-Montes e Alto Douro

Doutora **Maria Inês Barbosa de Carvalho**

Professora Associada, Universidade do Porto - Faculdade de Engenharia

Doutor **Mário Fernando dos Santos Ferreira** (orientador)

Professor Associado c/ Agregação, Universidade de Aveiro

palavras-chave Fibras ópticas, fibras ópticas microestruturadas, efeitos não-lineares, geração do supercontínuo, transparência induzida electromagneticamente.

resumo Este trabalho de doutoramento englobou o estudo de fenómenos ópticos não-lineares que ocorrem em fibras ópticas microestruturadas (MOFs), também chamadas fibras de cristais fotónicos (PCFs). Nestas fibras, temos as fibras microestruturadas de núcleo sólido (SC-MOFs) e as fibras microestruturadas de núcleo oco (HC-MOFs), que permitem a guiagem de luz numa diversidade de condições não atingidas com as fibras convencionais. Estudou-se os mecanismos de guiagem de luz nestas fibras, o que quer para as SC-MOFs quer para as HC-MOFs incluiu a obtenção dos modos de propagação, e para estas últimas incluiu ainda o cálculo das bandas fotónicas, bandas proíbidas, e densidade de estados. Por outro lado, as curvas de dispersão e os coeficientes não-lineares de SC-MOFs e HC-MOFs preenchidas com gases foram calculados. Também se efectuou a modelação e a simulação da propagação não-linear de impulsos ultra-curtos nestas fibras. Com as simulações deste trabalho, foi prevista a geração do supercontínuo e de luz ultravioleta em certas condições. Na última parte deste trabalho o efeito da transparência electromagneticamente induzida em fibras de núcleo oco foi investigado em detalhe.

keywords Optical fibres, microstructured optical fibres, nonlinear effects, supercontinuum generation, electromagnetically induced transparency.

abstract This Ph.D. embraced the study of the nonlinear optical phenomena occurring in microstructured optical fibres (MOFs), also called photonic crystal fibres (PCFs). In these fibres, there are the solid-core MOFs (SC-MOFs) and the hollow-core MOFs (HC-MOFs), which allow guided propagation of light in a diversity of conditions that are not possible with conventional fibres. The mechanisms of guidance of these fibres were studied, which for SC-MOFs and HC-MOFs included the computation of the guided modes, and for the latter included also the calculation of photonic bands, bandgaps, and density of states. In addition, the dispersion curves and the nonlinearity coefficients of SC-MOFs and of gas-filled HC-MOFs were calculated. The nonlinear propagation of ultra-short pulses of light in those fibres was modeled and simulated. With the simulations of this work, the supercontinuum generation, and the UV-light generation were predicted in certain conditions. In the last part of this work the electromagnetically induced transparency effect in hollow core fibres was investigated in detail.

TABLE OF CONTENTS

LIST OF FIGURES

LIST OF TABLES

LIST OF ACRONYMS

AFF – *Air filling fraction*

AS – *Archimedean spiral*

ASC – *Air suspended core*

BPMs – *beam propagation methods*

CW – *Continuous wave*

DOS – *Density of states*

EIT – *Electromagnetically induced transparency*

ES – *Equiangular spiral*

FEMs – *Finite element methods*

FoL – *Flower of life*

FT – *Fourier transform*

FWM – *Four wave mixing*

FWHM – *Full width at half maximum*

GNLSE – *Generalized nonlinear Schrödinger equation*

GVD – *Group velocity dispersion*

HC-MOF /HC-fibre – *Hollow-core MOF*

IFT – *Inverse Fourier transform*

JASR – *Jacket air suspended rod*

LS-MOF – *Layered spiral (SC-)MOF*

MOF – *Microstructured optical fibre*

MPB – *MIT photonic bands (software)*

NLSE – *Nonlinear Schrödinger equation*

NSR – *Nonsolitonic radiation*

ODE – *Ordinary differential equation*

PBG – *Photonic band gap*

PCF – *Photonic crystal fibre*

RWA – *Rotating wave approximation*

SC-MOF /SC-fibre – *Solid-core MOF*

SPM – *Self-phase modulation*

SCG – *Supercontinuum generation*

SEM – *Scanning electron microscopy*

SRS – *Stimulated Raman scattering*

SSFS – *Soliton self frequency shift*

SST – *Self-steepening*

TIR – *Total internal reflection*

TE – *Transverse electric*

TM – *Transverse magnetic*

UV – *Ultra-violet*

WDM – *Wavelength division multiplexing*

X-FROG – *Cross-correlation frequency-resolved optical gating*

XPM – *Cross-phase modulation*

ZD – *Zero dispersion*

ZDW – *Zero dispersion wavelength*

1 INTRODUCTION

1.1 Introduction

The optical fibres represent an important tool for the communication systems, with a significant impact on the society. The phenomenon that allows the light guidance in conventional optical fibres is the total internal reflection (TIR) known since XIX century [21, 111]: the first experiment that demonstrated this kind of light guidance was made in 1854 by J. Tyndall. He demonstrated that light can be guided through a jet of water by suffering successive total internal reflections.

The first optical fibres were fabricated in 1920's [48], however, they had impracticable huge losses. At that time, the fabrication processes did not prevent material impurities. The optical fibres became more common during the 50's of XX century, when the fibre's core was involved by a cladding. The first applications of optical fibres were in the area of medicine for guidance of light in short distances [31, chapt. 1]. In the year of 1966, Dr. C. Kao has suggested that optical fibres could be used to transfer information in communication systems, [56] which has granted him the Nobel prize in 2009. With the technological advances, it was possible to reduce the attenuation of optical fibres to only 0.2 dB/km in the spectral region of 1.55μm, by 1979 [76]. The first fibre systems in optical communications appeared in 1980's. With the technological evolution, in 1990's bit transfer rates of 1Tb/s were obtained for multi-channel systems [31]. The usage of erbium dopped fibres amplifiers (EDFA) allowed a revolution in the communication systems, such that the transmission through optical fibres has reached long distances in the beginning of 90's.

The posterior progresses lead to a wide spread of the optical communication systems: nowadays, the optical fibres are used in the infrastructures of the internet, worldwide.

In 1996, a new class of optical fibres has appeared, the so-called microstructured optical fibres (MOFs) or photonic crystal fibres (PCFs). The microstructured optical fibres have a micro-structured geometry in the cross-section over the entire fibre's length [12, 59, 93, 119]. The idea for fabricating MOFs has come from photonic crystals, firstly proposed in 1987 [55, 118]. In fact, the first proposed MOFs were fibres with a photonic crystal in their cladding and whose core is called a defect, i.e. a zone without the same surrounding periodicity. After the initial idea of fabricating MOFs with the format of 2D photonic crystals, about 4 years of studies were carried out. The experiments as well as numerical studies for finding the bandgaps were taken simultaneously. Then, in fact, the 1st MOF that was fabricated for testing the ocurrence of photonic bandgaps effect guided by means of modified TIR effect [93]. After that, various types of MOFs have successively appeared.

In particular, different microstructured details of MOFs can lead to different properties and to different guidance mechanisms. In fact, the characteristics of light propagation such as dispersion, nonlinearity, or even loss [9, 119] can be tailored by the fibre's design.

These novel fibres can be divided into two main categories: the solid core MOFs (SC-MOFs) and the hollow-core MOFs (HC-MOFs) [31, chapt. 13]. In the SC-MOFs category, the guidance of the light is generally due to the effect of modified total internal reflection, which is analogous to the guidance mechanism of the conventional optical fibres, but more complex [60]. On the other hand, in the HC-MOFs category, the photonic crystal that composes the cladding only allows propagation of light in certain frequency bands. The bands where propagation is not permitted are caled photonic bandgaps and the core guidance occur at frequencies within those bandgaps [61]. In some other HC-MOFs the guidance mechanism is not really a bandgap in the cladding but low density of states in the cladding or very low coupling between cladding and core modes [6].

Nowadays, various laboratories worldwide can produce their own MOFs using different fabrication techniques [29], and there are MOFs commercially available. In order to fabricate a MOF the first step is to produce a "preform" (a macroscopic piece with the planned microstructure), and the second step is to draw down to the fibre with the desired dimensions. There are various techniques to achieve this: stacking of capillaries and rods, extrusion, sol-gel casting, and injection moulding and drilling.

The propagation of light in MOFs has been studied and experimentally realized by con-

sidering various materials in the fibre cross-section, however, silica is still the more common solid material for MOFs. Nevertheless, the core and/or the cladding of SC-MOFs can be made of glasses of higher nonlinearity than silica, namely lead-silicate, bismuth oxide, tellurite, and chalcogenide glasses [27, 63, 64, 66, 89], or the core of HC-MOFs can be filled with liquids [65, 83, 113] or gases [8, 109]. In addition, the cladding of those fibres can be composed of a pattern of different materials. The possibility of having various materials in the cross-section of the fibre gives them peculiar characteristics, which are far from the bulk materials' characteristics.

For standard fibres, when the intensity of the light is high enough, the response of the medium is no longer linear. With the expansion of usage of optical fibres in the whole world, the nonlinear optical phenomena become more relevant. Nevertheless, the first experimental work showing nonlinear effects in optical fibres was done by E. Ippen with a CS_2-core fibre, in 1970 [53].

In fibre communications, the nonlinear phenomena appeared at first as a phenomenon that distorts the signals, which for propagation purposes leads to certain restrictions. However, for the manipulation of the signals we usually need nonlinear effects: such that for amplification, reshaping, optical wavelength conversion, etc. which are very important for photonic networks. This seems almost a paradox: the nonlinear effects can become a problem or an important solution. The nonlinear optical processes offer a potential solution to the construction of future full "photonic networks"[97]. In particular, the nonlinearity of silica-based fibres can be responsible for a wide range of nonlinear phenomena, being used and proposed for diverse all-optical signal processing devices [31].

The optical fibre's nonlinearity can be increased through the tailoring of the fibre's design by changing the design of the structure or their parameters, for instance by reducing the fibre core or increasing the index contrast, or by using materials such as highly nonlinear glasses.

Amongst the nonlinear phenomena, one particularly studied in this thesis is the supercontinuum generation [25, 26, 105]. This effect occurs when a narrow band signal passing through a medium suffers an extreme spectral broadening due to a combination of dispersive and nonlinear effects. With highly nonlinear fibres, the required fibre length to achieve the supercontinuum generation was experimentally reduced to the order of cm [31], whereas in this thesis numerical simulations show that for the layered spiral MOF (LS-MOF) model [92] this may happen in 0.3 mm only.

With gas-filled HC-MOFs the generation and propagation of new frequencies may occur in

the UV region, since the gases are transparent at the UV region. It is also possible to tune this process. This effect has several applications, namely in ultrafast spectroscopy, multiphoton microscopy and remote sensing [4, 71]. Furthermore, the interaction of reasonable intense light with a gas may generate a plasma [49, 99]. The plasma is created when the ionization of the gas exceeds a certain threshold, leading to the separation of positive and negative charges of the material.

HC-MOFs, with their ability to host atoms and molecules and to strongly confine light over very long interaction lengths, provide an ideal medium for performing low-power nonlinear optics. Nonlinear optics at ultra low-light levels is critical for quantum information processing and cryptography, which require single-photon or quasi single photon manipulation, generation, and storage [13].

The interaction of light in atomic vapours resonantly inside of the core of a HC-MOF is also very advantageous, since inside the core the light is diffraction free. In particular, the phenomenon of electromagnetically-induced transparency (EIT) [10, 84] has been experimentally realized in HC-MOFs. This effect can be observed when a material is subjected to two laser signals: one strong laser signal and a weak probe laser signal both near to a resonance. The interaction between the material and the strong laser signal will produce a different energy levels layout, in such a way that the probe laser is not absorbed as it would be in the absence of the strong laser. In an EIT configuration, we can obtain slow-light and fast-light, as well as high nonlinearity.

1.2 Thesis outlook

In chapt. 2, we will introduce the guidance mechanisms of solid-core microstructured optical fibres (SC-MOFs) and hollow-core microstructured optical fibres (HC-MOFs). We will distinguish these two types of fibres, and we will explain the distinct phenomena that can occur in those fibres, namely the modified total internal reflection, the photonic bandgaps, and the low density of states.

In chapt. 3, we will present our methods for studying SC-MOFs and HC-MOFs, which include work with Comsol multiphysics software, Matlab programming language (and C++), as well as MIT photonic bands (MPB) software. We will distinguish the methods used to describe a fixed geometry with non-periodic boundary conditions, and with periodic boundary conditions. The former can be applied to both SC-MOFs and HC-MOFs, and the latter can

be applied to HC-MOFs, which guide light due to periodicity of the cladding that leads to the existence of bandgaps.

In chapt. 4, we will present the properties of some SC-MOFs and HC-MOFs. We will study various models, including the layered spiral SC-MOF, and the kagomé HC-MOF. In addition, we will present several results for light propagation in those fibres, including the supercontinuum generation, and the UV light generation. The output characteristics that are relevant to our studies are, in the case of SCG, the band width of the output and the necessary fibre length for observing the phenomena in each medium; in the case of UV light we are interested in high coherent pulses, high quality pulses, and high efficient light conversion.

In chapt. 5. we will discuss the electromagnetically induced transparency (EIT) effect, in particular in HC-MOFs. We will describe the main theory of the EIT phenomenon, that can occur in a bulk or in a guided medium. In our case, we will proceed by studying the impact of confining the medium of EIT in a HC-MOF. We will analyse the properties in such conditions, by describing the variation of the refractive index of a HC-MOF with a periodic structure in the cladding and with a EIT medium in the core, whose properties depend on the pump and probe lasers of the EIT phenomena.

Finally, we end in chapt. 6 with our conclusions and suggestions for future work in these subjects.

1.3 List of publications

– **papers in international journals:**

– S.M.G. Rodrigues, M. Facão, and M.F.S. Ferreira, "Modelling and simulation methods for microstrutured optical fibres" - in preparation.

– S.M.G. Rodrigues, M. Facão, M.I. Carvalho, and M.F.S. Ferreira, "Modelling and simulation of electromagnetically induced transparency in hollow-core microstructured optical fibres", Optics Communications, vol. 468, pp. 125791 (2020).
DOI: 10.1016/j.optcom.2020.125791

– S.M.G. Rodrigues, M. Facão, and M.F.S. Ferreira, "Light propagation in gas-filled kagomé hollow core photonic crystal fibres", Optics Communications, vol. 412, pp. 102-107 (2018).
DOI: 10.1016/j.optcom.2017.11.025

– S.M.G. Rodrigues, M. Facão, and M.F.S. Ferreira, "Supercontinuum generation in chalcogenide layered spiral microstructured optical fiber", Journal of Nonlinear Optical Physics & Materials, vol. 26 (4), pp. 1750049-1750060 (2017).
DOI: 10.1142/S0218863517500497

– S.M.G. Rodrigues, M. Facão, and M.F.S. Ferreira, "Ultraviolet light generation in gas-filled kagomé photonic crystal fiber", Fiber and Integrated Optics, vol. 34 (1-2), pp. 76-89 (2015).
DOI: 10.1080/01468030.2014.1001092

– B.D. Tiburcio, G.M. Fernandes, J. Monteiro, S. Rodrigues, M. Ferreira, M. Facão, M.I. Carvalho, and A.N. Pinto, "EIT in hollow-core fibers for optical communications devices", Microwave and Optical Technology Letters, vol. 57 (2), pp. 348-352 (2015).
DOI: 10.1002/mop.28836

– M. Facão, S. Rodrigues, and M.I. Carvalho, "Temporal dissipative solitons in a three-level atomic medium confined in a photonic band-gap fiber", Phys. Rev. A, 91:013828, (january, 2015).
DOI: 10.1103/physreva.91.013828

– S.M. Rodrigues, M.M. Facão, S.C. Latas, and M.F. Ferreira, "Highly nonlinear layered spiral microstructured optical fiber", Photonics and Nanostructures - Fundamentals and Applications, vol. 11 (3), pp. 226-233 (2013).
DOI: 10.1016/j.photonics.2013.03.001

– **book chapters:**

– Sílvia M.G. Rodrigues, Margarida M.V. Facão, and Mário F.S. Ferreira, "Dispersive and nonlinear properties of gas-filled kagomé photonic crystal fibers" - chapt. 8, Optical fibers: technology, communications and recent advances, 2017; ISBN: 978-1-53610-966-5.
https://www.novapublishers.com/catalog/product_info.php?products_id=61202

– S. Rodrigues, M. Facão, S. Latas, and M. Ferreira, "Soliton related effects in supercontinuum generation", in "Solitons: interactions, theoretical and experimental challenges and perspectives", Nova Publishers, 2013; ISBN: 978-1-62618-234-9.
https://www.novapublishers.com/catalog/product_info.php?products_id=37594

– **papers in proceedings of scientific conferences:**

– B.D. Tiburcio, G.M. Fernandes, J.M. Monteiro, S. Rodrigues, M.I. Carvalho, M. Facão, M. Ferreira, and A.N. Pinto, "Experimental setup for electromagnetically induced transparency observation in hollow-core fibers", SPIE Proc., vol 9286, 92860H, (august, 2014).
DOI: 10.1117/12.2063625

– S. Rodrigues, M. Facão, S. Latas, and M. Ferreira, "Femtosecond pulse propagation in gas-filled hollow-core photonic crystal fibers", in Photoptics 2014, pp. 51-55, SCITEPRESS (2014).
DOI: 10.5220/0004696000510055

– S.M. Rodrigues, M.M. Facão, S.C. Latas and M.F.S. Ferreira, "Design of microstructured optical fibers for supercontinuum generation", SPIE Proc., vol. 8785, RIAO-OPTILAS, 87854h (november, 2013).
DOI: 10.1117/12.2026189

– G.M. Fernandes, M. Facão, M.I. Carvalho, S. Rodrigues, J. Heidarialamdarloo, A.N. Pinto, M.F. Ferreira, "Continuous wave supercontinuum generation aided by a weaker pulse laser", SPIE Proc., vol. 8434, Nonlinear Optics and Applications VI, id 843413 (2012).
DOI: 10.1117/12.922715

– **oral communications in conferences:**

– oral presentation "Nonlinear optics in kagomé microstructured optical fibres", AOP2017, Faro, Portugal.

– oral presentation in MAP-fis annual conference, in 2015-06-26.

– oral presentation in MAP-fis annual conference, in 2014-09-25.

– oral presentation "Light propagation in xenon filled kagomé hollow core photonic crystal fibers" (2014-05-26), AOP2014: II international conference on applications of optics and photonics, Aveiro, Portugal.

– oral presentation "Light guidance in microstructured optical fibres" in ENEF: "Encontro nacional de estudantes de física"2014 (2014-02-06), Aveiro, Portugal.

– oral presentation in the day of the physics department, of UA: “Nonlinear phenomena and supercontinuum generation in microstructured optical fibers” (2013-09-25).

– oral presentation in the IT meeting - V seminar in multi-gigabit optical networks: ”design and properties of microstructured optical fibers”[2012-09-14].

– **posters in conferences:**

– poster “Linear and nonlinear effects in gas-filled hollow core microstructured optical fibres”, “Encontro da ciência 2017”, Lisboa, Portugal.

– poster “The electromagnetic induced transparency effect in hollow core microstructured optical fibres”, AOP2017, Faro, Portugal.

– poster “Nonlinear optics in gas-filled kagomé microstructured optical fibres” no encontro do i3N: VI annual meeting i3N, Lisboa, 24th-25th of february, 2017.

– poster “Light guidance properties of kagomé hollow-core photonic crystal fibres”, 14th IUVSTA school – Nano-optics, at INL (2016), Braga, Portugal.

– poster in MAP-fis annual conference: “Modelling and simulation of nonlinear optical phenomena in hollow-core photonic crystal fibres” (2016-07-01).

– poster “Supercontinuum: generation in as2s3 layered spiral microstructured optical fibre”, OSA Congress: Advanced photonics 2016, Vancouver, Canada, july of 2016.

– poster “Stable temporal dissipative solitons in resonant gases confined in PBG fibers”, M. Facão, M.I. Carvalho, S. Rodrigues, and M.F. Ferreira, in the conference Photonica 2015, Serbia.

– poster “Nonlinear optical phenomena in microstructured optical fibres” in V annual meeting i3N, Aveiro, 10th-11th of april, 2015.

– poster “Light generation in the UV region in kagomé hollow-core photonic crystal fibers”, Photon14 (2014), London, UK.

– poster research day of UA: “Femtosecond pulse propagation in gas-filled hollow-core photonic crystal fibers” (2014-06-03).

– poster “Design of microstructured optical fibres for suercontinuum generation” at ”18ª Conferência nacional de física”, organized by SPF (sociedade portuguesa de física) - Aveiro, 6th-8th of september, 2012.

– poster “Design of silica fibers for the supercontinuum generation” in IV annual meeting i3N, Figueira da Foz, 9th-10th of mars, 2012.

2 PULSE PROPAGATION IN OPTICAL FIBRES

In this chapter, we will start by explaining the different mechanisms that provide light guidance in microstructured optical fibres (MOFs), dividing them in two groups: the solid-core MOFs, and the hollow-core MOFs. Then, we will derive the master equation for determining the guided modes, and an equation for pulse propagation. We will then proceed describing the fibre's main linear and nonlinear properties.

2.1 Light guidance mechanisms

In a homogeneous medium the light propagates in rectilinear direction but suffers diffraction leading to the increase of the beam width. In addition, in a real setting light suffers diffraction when it finds obstacles. However, the increase of the beam width resulting from diffraction can be overcome in certain geometrical arrangements of different dielectric materials, such as optical fibres.

Here, we analyse some of the mechanisms responsible for light guidance in optical fibres. The well-known total internal reflection (TIR) effect was used for showing light guidance for the first time in the XIX century [111], and nowadays this is the effect that supports the guidance in conventional optical fibres.

The TIR effect occurs when the light reaches an interface from a medium to another if the second medium has a lower refractive index and the light reaches the interface at an angle higher than the critical angle. This effect occurs repeatedly in a conventional optical fibre, and therefore the light is guided in the fibre's core since it is surrounded by a cladding with a lower refractive index.

The TIR effect occurs following the Snell law, also known as the refraction law:

$$n_i \sin\theta_i = n_r \sin\theta_r \tag{2.1}$$

where n_i is the refractive index of the material where the incident ray propagates, θ_i is the incidence angle, n_r is the refractive index of the material where the refracted ray propagates, and θ_r is the refraction angle. If $n_i > n_r$, and $\theta_i \geq \theta_c$, where θ_c is the critical angle given by $\theta_c = \arcsin(n_r/n_i)$, there is no refracted light, such that the TIR phenomena occurs.

In addition, in microstructured optical fibres (MOFs), new guidance mechanisms have been observed. In these fibres we have two main types of guidance: i) the modified TIR guidance, ii) the photonic band gap guidance, or other associated effects such as the low density of states (DOS).

2.1.1 Light guidance in solid-core MOFs

In solid core microstructured optical fibres (SC-MOFs), the necessary condition for the occurrence of light guidance due to the modified TIR is that the core's refractive index must be higher than the cladding's average refractive index.

In standard optical fibres with TIR and in MOFs with modified-TIR, the propagation constant $\beta = k_{//}$ is defined as the longitudinal component of the wavenumber k. In fact, the propagation constant follows the condition:

$$\text{avg}(n_{cl}) < \frac{\beta}{k_0} < n_{co}, \tag{2.2}$$

where n_{co} is the refractive index of the core, $\text{avg}(n_{cl})$ is an "average" of the refractive index of the cladding, and $k_0 = 2\pi/\lambda$ is the wavenumber in vacuum. The effective refractive index is related to the propagation constant, β, through the definition:

$$n_{\text{eff}} = \beta/k_0. \tag{2.3}$$

The refractive index of a material, $n(\mathbf{r})$, is given by:

$$n(\mathbf{r}) = \frac{c}{v(\mathbf{r})} = \sqrt{\epsilon_r(\mathbf{r})\mu_r(\mathbf{r})} \approx \sqrt{\epsilon_r(\mathbf{r})}, \tag{2.4}$$

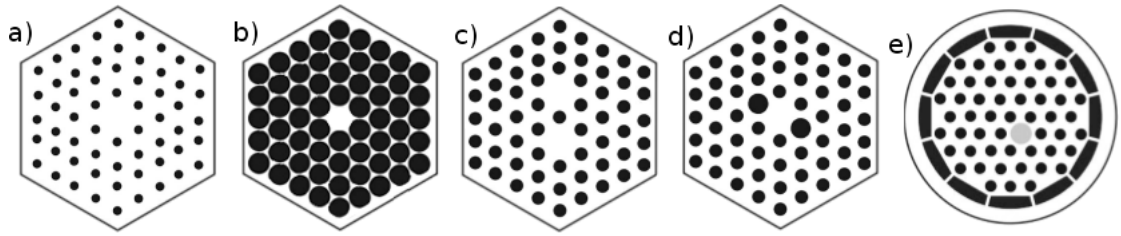

Fig. 2.1: Schematic representation of various solid-core MOFs; the white regions represent glass, the black regions represent air, and the grey regions represent doped glass; a) "endlessly single-mode" SC-MOF; b) very high air filling fraction SC-MOF; c) double core SC-MOF; d) birefringent SC-MOF; e) double cladding SC-MOF with doped and deviated core (adapted from ref. [93]).

where $\mathbf{r}$ indicates the location at the material, c is the speed of light in vacuum, $v(\mathbf{r})$ is the speed of light at the point $\vec{r}$ of the material, ϵ_r is the relative permittivity, and μ_r is the relative permeability; the approximation made here is due to the fact that $\mu_r = 1$ for most of the materials used in MOFs.

Examples of SC-MOFs can be seen in Figs. 2.1.a)-e). The fibre in a) is an endlessly single mode fibre: it guides only one propagation mode for all of its operating wavelengths; the fibre in b) has a very high air filling fraction, which leads to a high field confinement and therefore is often used for nonlinear applications; the fibre in c) is an example of a fibre with multiple cores; the fibre in d) has a high birefringence due to the asymmetry induced by the different dimensions of the holes; the fibre in e) has a double cladding and a deviated and doped core for guidance by modified TIR.

The possibility to have an endlessly single mode fibre, i.e. a fibre with only one propagation mode over a wide frequency range [112], is an important characteristic. It was found that this occurs in hexagonal MOFs for $d/\Lambda < 0.43$ [93], where d represents the holes diameters, and Λ is the pitch.

The mode with the maximum effective refractive index, $n_{\max}$, permitted in the SC-MOFs corresponds to the fundamental propagation mode. Its value depends strongly on the wavelength of the light that propagates in the fibre. In the limit of high wavelengths, the effective refractive index of the fundamental mode, $n_{\max}$ depends on the air filling fraction (AFF) and on the materials composing the fibre. In the case of a MOF composed by air and silica, $n_{\max}$ is given by [93]:

$$n_{\max} \to \sqrt{(1 - \mathrm{AFF})n_{\mathrm{glass}}^2 + \mathrm{AFF}n_{\mathrm{air}}^2}, \tag{2.5}$$

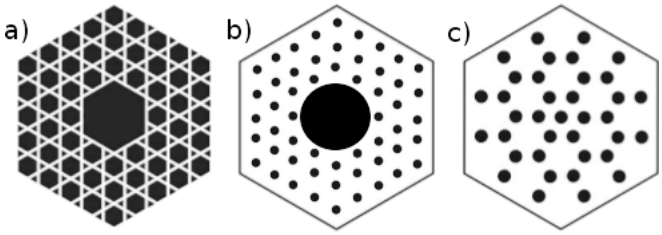

Fig. 2.2: Schematic representation of various MOFs whose refractive index of the core is lower than in the cladding; the white regions represent glass, the black regions represent air, and the grey regions represent doped glass; a) HC-MOF with kagomé structure in the cladding; b) HC-MOF with seven removed cells in the nucleus; c) HC-MOF with carbon ring structure in the cladding with a defect in the center for photonic band gaps guidance (adapted from ref. [93]).

In the limit of small wavelengths, the refractive index of the fundamental mode, $n_{\max}$, depends only on the refractive index of the glass constituting the core:

$$n_{\max} \to n_{\text{glass}}, \tag{2.6}$$

because light with a small wavelength can distinguish better the air and the glass regions, and therefore it remains well confined in the core, due to modified TIR effect.

2.1.2 Light guidance in hollow-core MOFs

The MOFs which have their core's average refractive index lower than their cladding's average refractive index are, usually, hollow-core microstructured optical fibres (HC-MOFs) and their predominant guiding mechanisms are the photonic bandgap (PBG) effect or low density of states (DOS) in the cladding, that occur due to the periodicity of the arrays of holes in the cladding. There is also the possibility of finding regimes with low coupling between the core and cladding modes [85].

The photonic bandgap regions in an optical fibre are frequency regions at which states of light propagating in the longitudinal direction are not allowed in the cladding, but they can still propagate in the core without escaping to the cladding, leading to the guidance of light in the core. In addition, even if there is not a full bandgap but if the density of states in the cladding is very low, light guidance in the core can still occur.

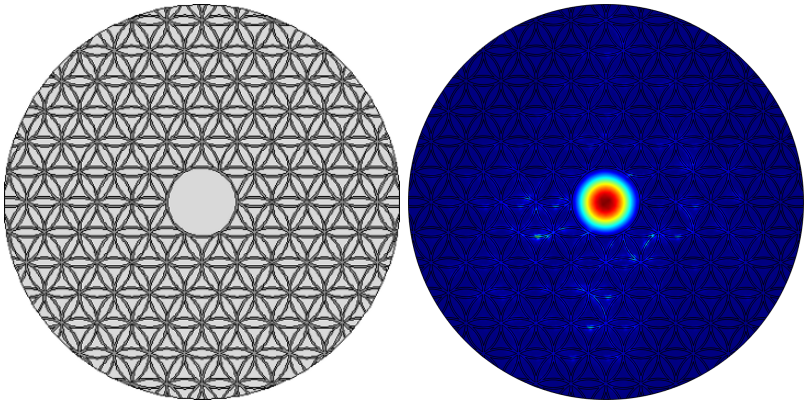

a) b)

Fig. 2.3: a) The flower of life fibre's model; b) a fundamental propagation mode confined in the core of a FoL fibre.

Examples of HC-MOFs can be seen in Figs. 2.2.a)-c).The fibre in a) has a kagomé lattice in the cladding, and in this case the guidance is due to the low density of states in the cladding; the fibre in b) is a typical hexagonal HC-MOF which guides by the photonic bandgap effect; the fibre in c) has a carbon ring structure in the cladding and a defect was inserted in the core for guidance by PBG effect.

The flower of life (FoL) fibre is a distinct fibre whose geometry is represented in Fig. 2.3.a), firstly proposed in this thesis. The flower of life structure can be found in arts patterns, but it has not yet applied to fibres. In the FoL fibre we expect theoretically to observe light guidance due to the periodicity of the cladding. This guidance may be possible due to full photonic band gaps or partial photonic band gaps, i.e. low density of states. In Fig. 2.3.b) we see a guided mode, which corresponds to the first prediction of hollow-core light guidance in this type of fibres.

2.2 Wave equations

The study of optical fibres is done in distinct ways if we are considering conventional fibres or MOFs. In fact the former can be studied with semi-analytical methods, whereas the latter require the use of numerical methods. In this section, we will introduce a general formalism, then we proceed by studying conventional optical fibres, and finally we will demonstrate an evolution equation for pulse propagation which can be used for studying both types of fibres.

The propagation of light can be described by various theories with different degrees of accuracy, namely geometric optics, wave optics, electromagnetic wave optics, or quantum

optics. In this section, we focus on the electromagnetic wave optics theory which is based on the Maxwell's equations [11, chapt. 2]:

$$\nabla.\mathbf{D} = \rho; \tag{2.7}$$

$$\nabla.\mathbf{B} = 0; \tag{2.8}$$

$$\nabla \times \mathbf{E} = -\frac{\partial \mathbf{B}}{\partial t}; \tag{2.9}$$

$$\nabla \times \mathbf{H} = \mathbf{J} + \frac{\partial \mathbf{D}}{\partial t}. \tag{2.10}$$

where $\mathbf{E}$ and $\mathbf{H}$ are respectively the electric-field and the magnetic-field, and $\mathbf{D} = \epsilon_0\mathbf{E} + \mathbf{P}$ is the electric displacement, and $\mathbf{B} = \mu_0\mathbf{H}$ is the magnetic induction; here ϵ is the permittivity or dielectric constant, μ is the permeability, ρ is the charge density, $\mathbf{J}$ is the current density, and $\mathbf{P}$ is the polarization vector;

The effects of light-matter interaction studied in this thesis result from the induced polarization of the medium by the electromagnetic field of light. When the light propagates in a dielectric material it disturbs the bound electrons causing a polarization response. The light, being an electromagnetically field oscillation, causes an oscillation in the bound electrons.

The polarization can be separated in two parts, corresponding to the linear and the nonlinear polarization:

$$\mathbf{P} = \mathbf{P}_L + \mathbf{P}_{NL}, \tag{2.11}$$

where $\mathbf{P}_L$ is the linear part of polarization given by:

$$\mathbf{P}_L(\mathbf{r}, t) = \epsilon_0 \int_{-\infty}^{t} \chi^{(1)}(t - t_1)\mathbf{E}(\mathbf{r}, t_1)dt_1. \tag{2.12}$$

where $\chi^{(1)}$ is the first order susceptibility.

On the other hand, close to resonances a semi quantum-mechanical treatment is necessary, as we will do in the Chapter 5, which is dedicated to the electromagnetically induced transparency (EIT) phenomena.

For fused silica, the most common material for fibres, the second order susceptibility term vanishes due to the centro-symmetry of the molecule [81, chapt. 1]. In addition, the noble gases, which will be studied here in the context of hollow-core fibres, are monoatomic so that their second order susceptibility term also vanishes. Therefore for the considered optical fibres in this thesis the lowest term of the nonlinear polarization is the third order, which is given by: [106]

$$\mathbf{P}_{\mathrm{NL}}^{(3)}(\mathbf{r},t) = \epsilon_0 \int\int\int_{-\infty}^{t} \chi^{(3)}(t-t_1,t-t_2,t-t_3)\vdots\mathbf{E}(\mathbf{r},t_1)\mathbf{E}(\mathbf{r},t_2)\mathbf{E}(\mathbf{r},t_3)dt_1dt_2dt_3, \quad (2.13)$$

where the vertical dots represent the tensorial product.

From Maxwell's equations (Eqs. 2.7-2.10) and Eq. (2.13), we obtain the following nonlinear wave equation (appendix (A.1)):

$$\nabla \times (\nabla \times \mathbf{E}) = -\frac{1}{c^2}\left(\frac{\partial^2 \mathcal{F}^{-1}\{\tilde{\epsilon_{\mathrm{r}}}\tilde{\mathbf{E}}\}}{\partial t^2} + \frac{1}{\epsilon_0}\frac{\partial^2 \mathbf{P}_{\mathrm{NL}}}{\partial t^2}\right) \quad (2.14)$$

where $\tilde{\mathbf{E}}$ denotes the Fourier transform of $\mathbf{E}$, and $\tilde{\epsilon_r} = \epsilon_0(1+\chi^{(1)})$.

In the following, in order to study the propagation of light in fibres we will do a separation of the analysis in two parts: in the first part (section 2.2.1.) we assume that the cross section is constant in all the longitudinal direction of the fibre, and that the fibre response is linear; and in the second part (section 2.2.2) we enlarge our assumption to consider that the fibre response is nonlinear and the light is in the form of short pulses, obtaining an equation for a slowly varying envelope of the electric field describing its evolution along the longitudinal direction in such a fibre.

2.2.1 Fibre modes

Let us consider monochromatic solutions that then may be used as a basis for describing the non-monochromatic solutions. The monochromatic solutions are of the form:

$$\mathbf{H}(\mathbf{r},t) = \mathbf{H}(\mathbf{r})e^{-i\omega t} \quad (2.15)$$

$$\mathbf{E}(\mathbf{r},t) = \mathbf{E}(\mathbf{r})e^{-i\omega t} \quad (2.16)$$

Using this separation of variables, and after a mathematical manipulation of Eqs. (2.7)-(2.10) assuming a linear response (appendix A.2), we obtain the equations for the electric-field and the magnetic-field, which depend on the transverse distribution of the relative electric permittivity $\tilde{\epsilon_r}$:

$$\nabla \times \left[\frac{1}{\epsilon_r(\mathbf{r},\lambda)}\nabla \times \mathbf{H}(\mathbf{r},\lambda)\right] = \left(\frac{\omega}{c}\right)^2 \mathbf{H}(\mathbf{r},\lambda); \quad (2.17)$$

$$\mathbf{E}(\mathbf{r},\lambda) = \frac{i}{\omega\epsilon_0\varepsilon_r(\mathbf{r},\lambda)}\nabla \times \mathbf{H}(\mathbf{r},\lambda); \quad (2.18)$$

or alternatively:

$$\nabla \times \nabla \times \mathbf{E}(\mathbf{r}, \lambda) = \left(\frac{\omega}{c}\right)^2 \epsilon_r(\mathbf{r}, \lambda)\mathbf{E}(\mathbf{r}, \lambda); \tag{2.19}$$

$$\mathbf{H}(\mathbf{r}, \lambda) = -\frac{i}{\omega\mu_0}\nabla \times \mathbf{E}(\mathbf{r}, \lambda); \tag{2.20}$$

where Eq. (2.17) is known as the master equation [54] with which we can find the fibre modes, assuming a relative electric permittivity in each point of the fibre cross-section. After solving Eq. (2.17), we obtain the optical field distribution with the Eq. (2.18). With these two equations we can obtain the optical guided modes and the corresponding propagation constant of an optical fibre.

In fact, we can choose to solve Eq. (2.17) or Eq. (2.19) only, i.e. to compute one of the fields, and then from Eq. (2.18) or Eq. (2.20) we know the form of the other field, and consequently the electromagnetic field distribution.

In general, in order to solve the master equation, Eq. (2.17), for a microstructured optical fibre or a photonic crystal, it is necessary to use numerical methods.

2.2.2 The nonlinear pulse propagation equation

In order to solve Eq. (2.14) for predicting the evolution of a pulse in fibres it is usual to consider a perturbative approach, by assuming that the nonlinear effects may be accounted as a small perturbation to the refractive index [26, 31]. Let us consider that the electric field is linearly polarized and do a scalar approach. The electric field and its Fourier transform are:

$$E = f(x, y)a(z, t)e^{-i\omega_c t + i\beta_c z} \rightarrow \mathcal{F}\{E\} = f(x, y)\tilde{a}(z, \omega - \omega_c)e^{i\beta_c z} \tag{2.21}$$

where $f(x, y)$ is the spatial mode field distribution along the cross section with coordinates x and y, $a(z, t)$ is the amplitude of the mode field along the direction z and the time t, and ω_c and β_c are the carrier frequency and the propagation constant, respectively. Here, we use $\mathcal{F}$ and the tilde of a function to denote the Fourier transform of that function, which is studied in the frequency, ω, domain.

Inserting this expression in (2.14) we obtain two equations:

$$\frac{1}{f}\nabla_t^2 f + \frac{\omega^2}{c^2}(n^2 + 2n\Delta n) = \beta^2; \tag{2.22}$$

$$-\frac{1}{\tilde{a}}\left(\frac{\partial^2\tilde{a}}{\partial z^2}+2i\beta_c\frac{\partial\tilde{a}}{\partial z}-\beta_c^2\tilde{a}\right)=\beta^2. \tag{2.23}$$

where $\nabla_t=\frac{\partial}{\partial x}\vec{e}_x+\frac{\partial}{\partial y}\vec{e}_y$ is the transverse component of the nabla operator, and Δn contains the losses and the nonlinear effects.

We shall compare Eq. (2.19) and Eq. (2.22). The Eq. (2.19) is deduced from Maxwell's equations, including the components x, y, z, but neglecting the nonlinear term, with $P_{NL}=0$. The Eq. (2.22) includes the nonlinear term as a perturbative variation of n; in addition this equation includes the propagation constant, β - this constant appears mathematically since the problem presents a solution to which we can apply a separation of variables approach, such that: $f_{xy}(x,y)=f_z(z)=\beta$; in practice this constant corresponds to $\beta=n_{\text{eff}}k$, including the property of dispersion due to the fact that different components of the wave propagate with distinct velocities in the medium; usually β is obtained by solving Eq. (2.19) and after that it is used to solve Eq. (2.23).

From Eq. (2.23), and using the slowly varying envelope approximation, we obtain the pulse propagation equation (appendix A.4):

$$\begin{aligned}\frac{\partial u(z,\tau)}{\partial z}-i\left[\sum_{k>1}\frac{1}{k!}\beta_k i^k\frac{\partial^k}{\partial\tau^k}u(z,\tau)\right]+\frac{\alpha}{2}u(z,\tau)=\\ =i\gamma\left(1+i\tau_{shock}\frac{\partial}{\partial\tau}\right)\int_{-\infty}^{\tau}R(\tau')|u(z,\tau-\tau')|^2dt'u(z,\tau),\end{aligned} \tag{2.24}$$

where u is the normalized amplitude of the optical field, z is the distance along the fibre, $\tau=t-\beta_1 z$ such that we transform to a co-moving frame, τ_{shock} is a timescale associated with effects such as the self-steepening and the optical shock formation, the β_k terms represent the several orders of dispersion, α represents the fibre losses, R represents the nonlinear response (including Kerr and Raman terms), and γ is the fibre's nonlinear parameter defined as:

$$\gamma=\frac{2\pi n_K}{\lambda a_{\text{eff}}}, \tag{2.25}$$

where n_K is the Kerr nonlinear coefficient and a_{eff} is the effective mode area, given by:

$$a_{\text{eff}}=\frac{\left(\int\int|f(x,y)|^2dxdy\right)^2}{\int\int|f(x,y)|^4dxdy}. \tag{2.26}$$

The nonlinear response function $R(t)$ in Eq. (2.24) can be written as [26]:

$$R(t)=(1-f_R)\delta(t)+f_R h(t), \tag{2.27}$$

where the Dirac δ-function respresents the instantaneous electron response (responsible for the Kerr effect), $h(t)$ represents the delayed ionic response (reponsible for the Raman scattering), and f is the fractional contribution of the delayed Raman response, which for silica is around 0.18 [26]. Also for silica, it is common to approximate $h(t)$ in the form: [26]

$$\frac{\tau_1^2+\tau_2^2}{\tau_1\tau_2^2}\exp(-t/\tau_2)\sin(t/\tau_1)\Theta(t), \tag{2.28}$$

where $\tau_1 = 12.2$ fs and $\tau_2 = 32.0$ fs, and $\Theta(t)$ is the Heaviside step function.

Here, $\beta_n = \frac{d^n\beta(\omega)}{d\omega^n}\Big|_{\omega=\omega_c}$ are the terms used in the Taylor series for β around $\omega = \omega_c$:

$$\beta(\omega) = \beta_c + \sum_{n=1}^{+\infty}\frac{1}{n!}\beta_n(\omega-\omega_0)^n. \tag{2.29}$$

In particular, β_c is the propagation constant at the central wavelength, β_1 is the inverse of the group velocity, and the parameter β_2 represents the group velocity dispersion of the fibre, both at ω_c.

When we neglect the higher order dispersion terms, the shock term, and the Raman effect, in Eq. (2.24) we obtain:

$$\frac{\partial}{\partial z}u(z,\tau) + i\frac{\beta_2}{2}\frac{\partial^2 u(z,\tau)}{\partial\tau^2} = i\gamma|u(z,\tau)|^2u(z,\tau), \tag{2.30}$$

This Eq. (2.30) is the so-called nonlinear Schrödinger equation (NLSE), due to a mathematical similarity between this equation and the Schrödinger equation from quantum mechanics.

In general, when we consider additional effects such as higher-order dispersion, Raman effect, self-steepening, and losses, such as in Eq. (2.24), we have the so-called generalized nonlinear Schrödinger equation (GNLSE).

In nonlinear optics, the Kerr effect may be seen as a refractive index that is dependent on the intensity of light. In the optical fibers, it can cause: self phase modulation (SPM), cross phase modulation (XPM), and four wave mixing (FWM). The Kerr coefficient depends on the particular material. In particular, some values for materials used in solid-core fibres are: [23, 42, 86]

- 2.6x10^{-20}m^2/W, for silica;
- 5.72x10^{-18}m^2/W, for arsenic trisulfide;
- 4.1x10^{-19}m^2/W, for SF57.

2.3 Linear and nonlinear effects

group velocity dispersion

The group velocity dispersion effect (GVD) is a linear effect and a consequence of the wavelength dependence of the refractive index. In a fibre the dispersion can be defined as the changing of the effective refractive index, $n_{\text{eff}}(\lambda)$, of each mode with the wavelength. In fact, $n_{\text{eff}}(\lambda)$ depends on both material and waveguide contributions, so that it can be tailored by adjusting the design parameters of a MOF.

The main order of dispersion that affects the pulses is the second order, usually called group velocity dispersion which is characterized by the parameter β_2 mentioned above. However, in practice it is common to use the dispersion parameter D related to β_2 by:

$$D = -\frac{2\pi c}{\lambda^2}\beta_2, \tag{2.31}$$

As with other dispersion terms, the group velocity dispersion depends on the chromatic dispersion of the materials and on the waveguide dispersion [46]. In Fig. 2.4, we compare the dispersion curve for pure silica and the dispersion curve for a standard silica step-index fibre, where we may see that the zero dispersion wavelength (ZDW) is located close to 1.31μm, in both cases.

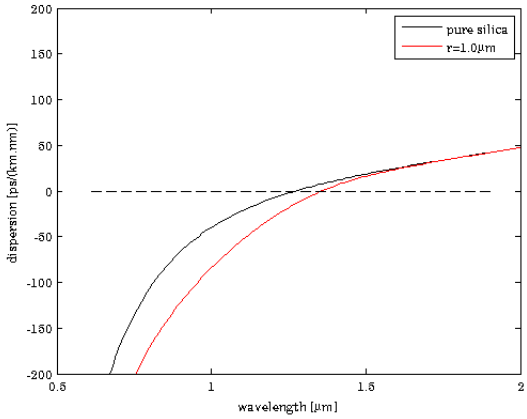

Fig. 2.4: Dispersion curves: i) for pure silica; ii) for a *standard* optical fibre with r_{core}=1.0μm with silica dopped with germanium dioxide at 6.3mol% in the core, and pure silica in the cladding.

As mentioned above, in spite of the fact that the dispersion is a linear effect, it influences which new wavelengths can be created nonlinearly, namely through the four wave mixing effect. In this case, the necessary phase-matching for power transfer between different wave-

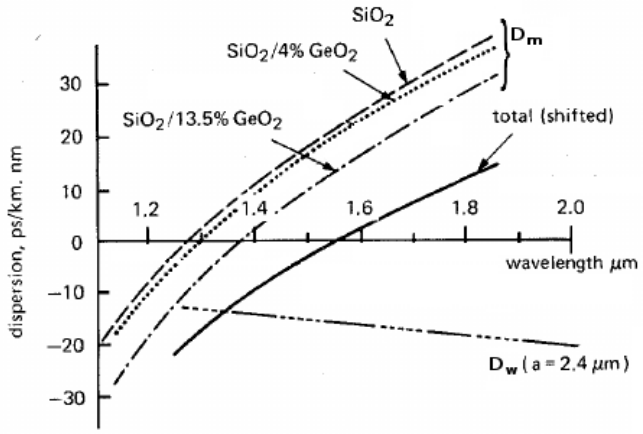

Fig. 2.5: Material dispersion for SiO_2, and $SiO_2/4\%GeO_2$; and material dispersion, waveguide dispersion, and total dispersion ($D = D_m + D_w$) for a dispersion shifted fibre ($SiO_2/13.5\%GeO_2$), where a is the core radius [adapted from ref. [2]].

lengths depends on the dispersion curve.

The sign of β_2 is critical for the light behaviour. The wavelength range for $\beta_2 > 0$ ($D < 0$) is called the normal dispersion regime, whereas for $\beta_2 < 0$ ($D > 0$) is called the anomalous dispersion regime. In the normal-dispersion regime, the higher frequency components of an optical pulse travel slower than the lower frequency components. In the anomalous-dispersion regime the opposite occurs. The wavelength for which the dispersion is zero, i.e. in the transition between these two regimes, is called the zero dispersion wavelength (ZDW).

The minimum loss for a standard silica fibre is located at 1.55μm[1, chapt. 2]. It is possible to shift the ZDW into the main low loss spectral region of the fibre, by combining the material dispersion, D_m, and the waveguide dispersion, D_w.[19]. Fig. 2.5 shows the group velocity dispersion of such a dispersion shifted fibre. This type of fibre is particularly important because it has a coincidence between the zero dispersion and the minimum of attenuation at 1.55μm.

Now we focus on the effects of second order dispersion only. For this purpose we neglect the fibre nonlinearity and reduce the NLSE to:

$$\frac{\partial u}{\partial z} = -i\frac{1}{2}\beta_2\frac{\partial^2 u}{\partial t^2}. \tag{2.32}$$

In the frequency domain, using the relation $\frac{\partial}{\partial t} \leftrightarrow -i\omega$, Eq. (2.32) reads:

$$\frac{\partial \tilde{u}}{\partial z} = \frac{i}{2}\beta_2\omega^2\tilde{u}, \tag{2.33}$$

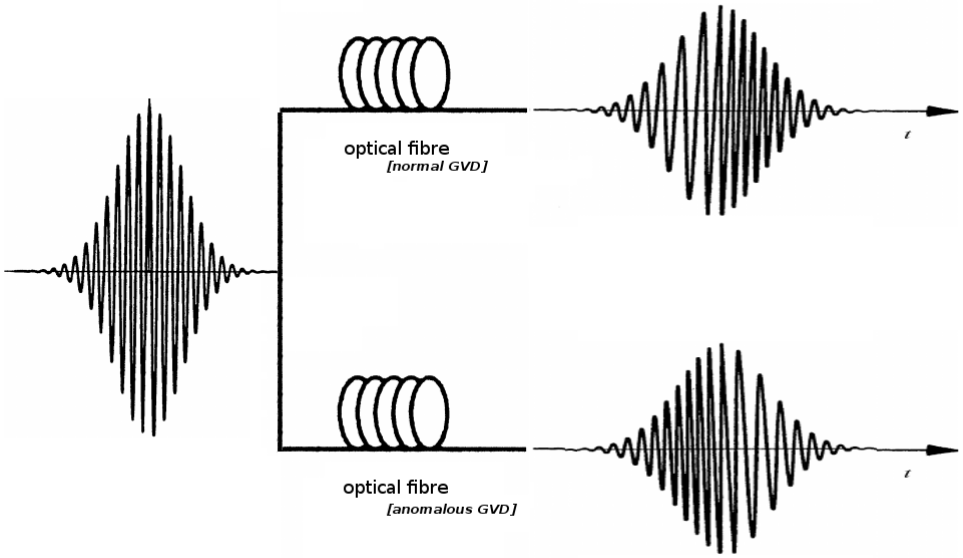

Fig. 2.6: Schematic illustration of the pulse's dispersion induced-chirp in the normal GVD regime and in the anomalous GVD regime.

where the tilde denotes the Fourier transform. The solution of Eq. (2.33) is:

$$\tilde{u}(z,\omega) = \tilde{u}(0,\omega)e^{\frac{i}{2}\beta_2\omega^2 z} \tag{2.34}$$

$$\begin{aligned} u(z,t) &= \mathcal{F}^{-1}\left\{\tilde{u}(z,\omega)\right\} \\ &= \textstyle\int_{-\infty}^{\infty} u(0,\omega)e^{\frac{i}{2}\beta_2\omega^2 z - i\omega t}d\omega. \end{aligned} \tag{2.35}$$

Normal dispersion or anomalous dispersion distort the pulses that travel along the fibre in a different way, as illustrated in Fig. 2.6, but in both cases there is pulse broadening. As an example, we show the spectral and temporal evolution of a pulse under the group velocity dispersion in Fig. 2.7.

It is convenient to define length scales after which the effects become significant. For the dispersion effects we define the dispersion length as the distance after which a maximal temporal phase excursion of 1 rad is accumulated, which corresponds to: $l_D = t_0^2/|\beta_2|$ [1], where t_0 is a variable related to the full width at half maximum (FWHM) of the pulse. In particular, for the hyperbolic secant pulses we have that: $t_{\mathrm{FWHM}} = 2\ln(1+\sqrt{2})t_0 \approx 1.762747t_0$.

When the second order dispersion is low, the third order dispersion becomes more relevant. In fact, when the dispersion curve is considerably away of a flat line various higher

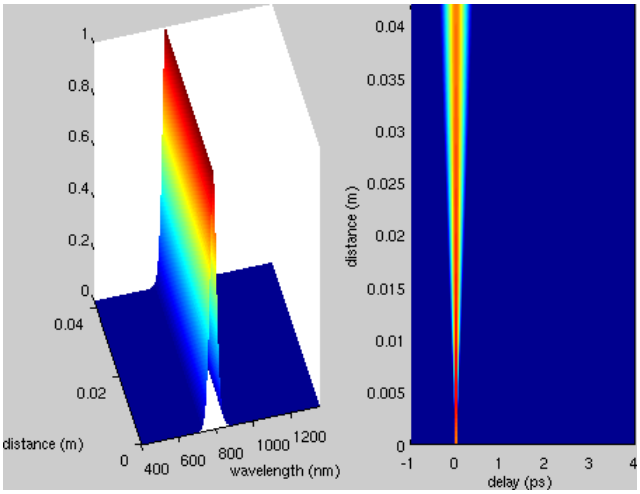

Fig. 2.7: Spectral and temporal evolution of a pulse, by considering the 2nd order dispersion term.

order dispersion terms are necessary to be taken into account.

fibre losses

When we launch a light pulse in an optical fibre, after some distance the pulse power will be lower than the initial power due to losses in the fibre:

$$P = P_0 e^{-\alpha l}, \tag{2.36}$$

where P_0 is the initial power, P is the power of the light pulse after a distance l and α is the attenuation constant. Is is more common to measure the losses in dB/km, such that the following relation is used:

$$\alpha_{dB} = -\frac{10}{l} \log\left(P/P_0\right) = 4.343\alpha. \tag{2.37}$$

We can evaluate the confinement losses through the imaginary part of the effective refractive index, since the imaginary part of n_{eff} represents a reduction of the signal's amplitude [33]:

$$\text{conf. loss[dB/m]} = \frac{20 \times 10^6}{\ln 10} \frac{2\pi}{\lambda[\mu\text{m}]} \text{Im}(n_{\text{eff}}). \tag{2.38}$$

where $n_{\text{eff}} = \beta/k_0$.

self-phase modulation

The Kerr effect produces a phase modulation on a pulse that propagates on an optical fibre. Such phase modulation can be due to the pulse itself, known as self-phase modulation (SPM) effect, or can be due to a different pulse, known as cross phase modulation (XPM) effect. The first observation of SPM in optical fibres has ocurred in 1975 [67].

To describe the SPM effect, we reduce Eq. (2.30) to:

$$\frac{\partial}{\partial z}u(z,t) = i\gamma|u(z,t)|^2 u(z,t), \tag{2.39}$$

which is valid when the group velocity dispersion is low, for relatively long pulses or continuous waves. The general solution for this equation is:

$$u(z,t) = u(0,t)e^{i\gamma|u(0,t)|^2 z}, \tag{2.40}$$

where z is the propagation distance. This solution shows that the fibre nonlinearity changes the phase of the pulse, but does not change the intensity envelope. In addition, this phase alteration is proportional to the power of the incident wave. In Fig. 2.8 we illustrate the distortion of a pulse due to SPM, where we can notice the higher frequencies going to the trailing edge and the lower frequencies going to the leading edge. In Fig. 2.9 we can view the propagation of a pulse subject to the SPM effect in the temporal and spectral domains, where we observe spectral broadening but a constant width in the temporal domain.

By comparing Fig. 2.6 and Fig. 2.8, we notice that in the anomalous dispersion regime SPM and GVD act in different directions. In this regime, nonlinearity- and dispersion- chirps can compensate each other, partially or completely.

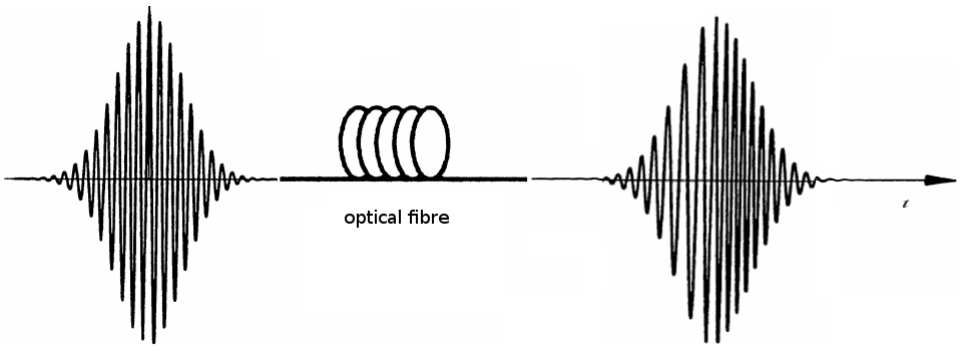

Fig. 2.8: Schematic illustration of the pulse's SPM induced-chirp.

It is also useful to define a length for which the nonlinear effects become significant. Such length corresponds to a maximum temporal phase shift of 1 rad, and it is given by:

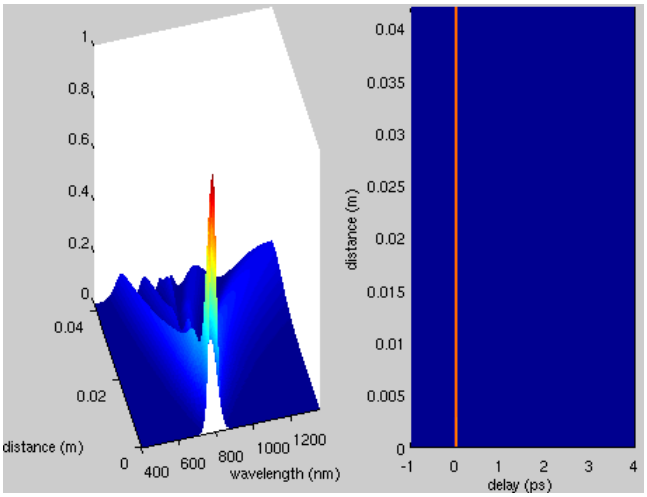

Fig. 2.9: Spectral and temporal evolution of a light pulse by considering only the SPM effect.

$l_{\mathrm{NL}} = 1/(\gamma P_0)$ [1], where P_0 is the peak power of the input pulse.

solitons

In the anomalous dispersion regime of an optical fibre, the chirp induced by SPM and the chirp induced by GVD can combine in such a way that we observe bright solitons, which correspond to stationary or periodic propagating light pulses. The existence of optical solitons in optical fibres was theoretically predicted in 1973[47], and they were indeed experimentally observed in 1980 [78]. The solitons correspond to analytic solutions of the NLSE: Eq. (2.30).

The most basic soliton is the fundamental soliton (i.e first order soliton), given by [1, chapt. 5]:

$$u(\xi, \tau) = \mathrm{sech}(\tau) \exp(i\xi/2), \tag{2.41}$$

where ξ and τ are the dimensionless variables defined as: $\xi = z/l_D$ and $\tau = t/t_0$; In this case, the SPM and the GVD cancel exactly each other, leading to a propagation of light with unchanged spectrum and unchanged pulse envelope, as seen in Fig. 2.11.a). There are also higher-order solitons, which have periodic evolutions. In Fig. 2.11 we observe the propagation of various solitons with different orders, where n_{order} is defined as:

$$n_{order} = \sqrt{l_{\mathrm{D}}/l_{\mathrm{NL}}}, \tag{2.42}$$

where l_{D} and l_{NL} are the characteristic dispersive length and characteristic nonlinear length

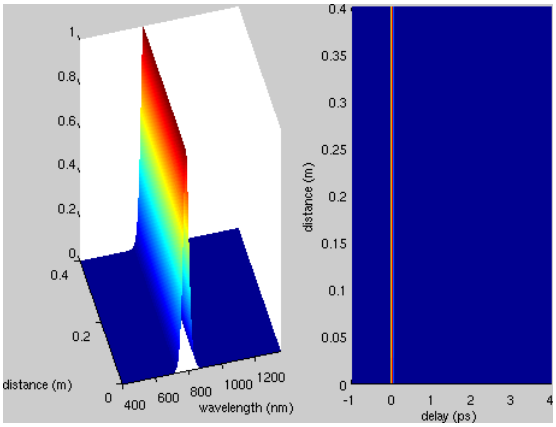

Fig. 2.10: Fundamental soliton propagation.

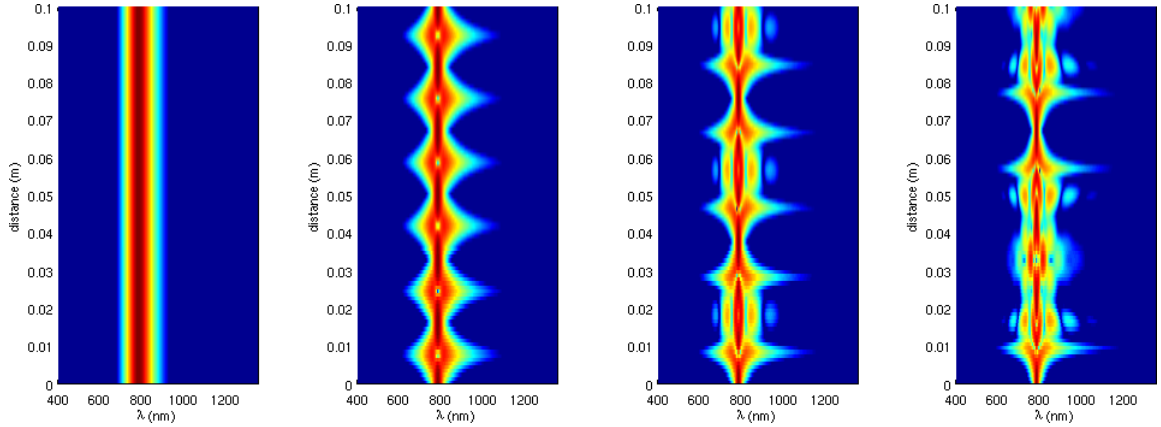

Fig. 2.11: Spectral evolution of the fundamental soliton and higher-order solitons; the same fibre was considered in these 4 graphs, the difference is on the input pulse power, whose values lead here to n_{order}={1, 2, 3, and 4}.

scales defined previously. The higher-order solitons have a periodic behaviour with a soliton period, z_0, given by [31, chapt. 9]:

$$z_0 = \frac{\pi}{2} L_D. \tag{2.43}$$

By using an input laser pulse with higher power, l_{NL} is decreased, and in consequence accordingly to Eq. (2.42) that pulse corresponds to a higher-order soliton. In fact, the propagation state will converge to a n^{th} order soliton with the closest integer value of n_{order}. [51, 70]

The fundamental soliton is very stable. In fact, even if a different pulse is launched in the fibre, with $n_{order} \approx 1$, the pulse can converge to a soliton: the pulse will release any excess of energy into linear waves rearranging its amplitude and its pulse duration to fulfill the soliton

conditions [51]. These solutions are called solitons in the sense that they are "solitary"waves, i.e. they are particular solutions which if its input energy is multiplied by a constant different from 1, the shape of the wave would not be proportional to the original shape. [75]. In fact, the soliton solutions have discrete energies corresponding to integer soliton orders, n_{order}.

If the pulse power is sufficiently higher than the required for hosting a fundamental soliton, the situation may be viewed as the lauching of more than one soliton, each of them with the same frequency, but with different pulse powers and pulse widths. This is the case for an injected pulse with $round(n_{order}) > 1$. The solution is not proportional to the fundamental solution if we increase linearly the input pulse energy, because each soliton propagation would affect the other solitons, as well. In the pulses with higher-order solitons, the multiple solitons interact with each other, in such a way that the resulting pulse will show a periodical evolution. Thus, the pulse shape can be reobtained [51], and we observe a periodical evolution instead of a stationary behaviour as with the case of the fundamental solition. This periodical behaviour is justified due to the fact that the nonlinear terms and the linear terms act with an alternative strength [106].

The higher-order solitons are unstable in the presence of small perturbations such as third- or higher- order dispersion, or Raman scattering.

The solitons launched in the anomalous dispersion regime suffer soliton fission, decaying into other sub-pulses. The soliton fission gives rise to multiple fundamental solitons each with different width and peak power [62]. The number of the multiple solitons that appear due to the soliton fission is given by n_{order}, and the distance at which the soliton fission occur is called fission length, which can be approximated by $l_{\text{fiss}} \approx l_D/n_{order}$ [109].

The intra-pulse Raman scattering (IRS) is responsible of a soliton shift due to the transfer of energy from higher to lower frequencies of the soliton spectrum. Such effect is referred to as soliton self-frequency shift (SSFS) [31, chapt. 13]. The Raman induced SSFS can be expressed by the formula [31, chapt. 13]:

$$\Delta f = -\frac{4t_R|\beta_2|z}{15\pi t_0^4}, \tag{2.44}$$

where t_R is the Ramna parameter, z is the distance, and t_0 is the soliton width.

The SSFS becomes more relevant for ultra-short pulses, since they have a large spectrum and thus they have more frequencies that can interact with each others. From Eq. (2.44) we observe that the change in the frequency increases with the distance of the travelled path.

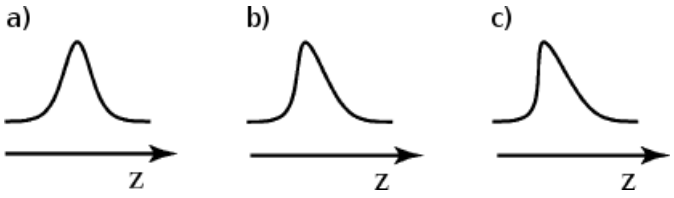

Fig. 2.12: a) The incident optical pulse with a Gaussian shape; b) the optical pulse after propagating in a nonlinear medium showing the self-steepening effect of the trailing edge; c) optical shock wave formation due to self-steepening when the change of the wave is abrupt (after ref. [11, chapt. 13]).

self-steepening

The self-steepening effect can be interpreted as a wavelength dependence of the Kerr effect [11, chapt. 13]. The spectral broadening of the pulse under the self-steepening is asymmetric, due to the different SPM for different wavelengths, and it is more pronnounced on the high-frequency side [51]. In the limit, this can cause an intensity profile of the pulse that changes instantaneously, which is called an optical shock wave [11, chapt. 13]. See the schematic representation on Fig. 2.12.

The Eq. (2.24) contains the Kerr and self-steepening terms:

$$\frac{\partial}{\partial z}u(z,t) = i\gamma\left(1+\frac{i}{\omega_0}\frac{\partial}{\partial t}\right)|u(z,t)|^2 u(z,t), \tag{2.45}$$

where we note that the self-steepening correction is proportional to ω_0^{-1} [1].

We can also define a length for which the self-steepening is observable: $l_{ss} = ct_0/(n_2 I)$ [11, chapt. 13], where I is the light intensity.

Fig. 2.12 represents a pulse evolution subject to the self-steepening effect. In Fig. 2.12.a) we show the input pulse; in b) we show the distortion of the pulse due to the self-steepening effect; and in c) we show the limit case when a optical shock wave is formed due to self-steepening. For this reason the self-steepening term is sometimes referred in the literature as the shock term, τ_{shock}.

supercontinuum generation

The supercontinnum generation (SCG) is an optical effect through which an initially narrow spectrum pulse transforms into a very broad spectrum pulse while it propagates in a nonlinear medium, such as an optical fibre.

The SCG occur due to the interplay between several dispersive and nonlinear phenomena

such as self-phase modulation (SPM), cross-phase modulation (XPM), stimulated Raman scattering (SRS) and four wave mixing (FWM).

The SCG may find several applications, namely in biomedical optics where it allows the improvement of the resolution of optical coherence tomography [80], in optical frequency metrology [80, 98], in all forms of spectroscopy [80], and as a multiwavelength source in the telecommunications [73][31, chapt. 14][101].

In this effect, the properties of the pump light pulse such as incident wavelength, peak power, and temporal width can contribute to the relative importance of these nonlinear phenomena. In addition, the fibre's dispersive characteristics also have an important role.

In order to enhance the supercontinnum generation in optical fibres, it is possible to increase the nonlinearity by decreasing the effective mode area, by adjusting the fibre's design, or by using highly nonlinear glasses in the composition of the fibre's core.

The SCG can be observed in two main regimes: i) shorter pulses with femto-second durations, and ii) longer pulses with pico-, and nano-second pulses, as well as with continuous wave (CW) light. On another hand, regarding the dispersion regime, SCG can be observed in the normal or in the anomalous dispersion pumping regimes.

In the femto-second pumping regime at the anomalous dispersion, the SCG presents the characteristics of soliton dynamics. The higher order solitons are unstable in the presence of higher order dispersion terms or stimulated Raman scattering (SRS) effect, occurring the soliton fission.

In particular, SCG was observed with mode-locked Ti:saphire lasers (tunnable from red to infrared light), mode-locked krypton ion lasers at 647nm and frequency doubled Nd^{3+}-based lasers at 532nm, in tappered silica fibres with core diameters sufficiently reduced [91].

2.4 Summary

In this chapter we have presented the theoretical background about guided light propagation, in particular in MOFs. We have studied the different light guidance mechanisms that occur in SC-MOFs and HC-MOFs. In SC-MOFs we have the so-called modified total internal reflection effect, whereas in HC-MOFs we have the bandgaps effect or low density of states (DOS) in the cladding.

In order to observe the modified TIR effect, the core's refractive index must be higher

than the cladding's average refractive index. In order to observe the photonic bandgaps or low DOS the structure of the cladding must have a periodic pattern that leads to light being forbidden (or almost forbidden) in the cladding in a certain frequency band: the light cannot propagate through the cladding, but can propagate through the core that is a defect on the cladding structure, and thus it is core guided.

We have presented various designs for SC-MOFs and HC-MOFs, from which we can choose for each application.

Then, we have proceeded to the derivation of the equations for finding the propagation modes in fibres, Eqs. 2.17-2.18, and for describing the propagation of pulses, Eq. (2.24).

For deriving Eqs. 2.17-2.18 we have assumed that the cross section is constant in all the longitudinal direction of the fibre, and that the response is linear. For deriving Eq. (2.24) we took into account the fibre nonlinearity and we obtained an equation for the evolution of a slowly varying envelope of the electric field.

We then described some linear and nonlinear effects that can occur in MOFs. We also described conditions for the existence of solitons and their properties. Finally, we addressed the characteristics of SCG which will be investigated in this thesis for some MOFs.

3 MODELLING AND SIMULATION METHODS

The study of the properties of light propagation in microstructured optical fibres is strongly dependent on the usage of numerical tools. Due to the complex patterns of the refractive index of MOFs there are no analytical solutions in most of the cases. However, using numerical methods for solving the equations presented in the previous chapter we are able to find the propagation properties of different types of MOFs.

In this chapter we are going to discuss our numerical methods for the study of light propagation in MOFs. We will introduce the Comsol models developed for this purpose, the Matlab code, and the MIT photonic bands (MPB) software. With Comsol we find the propagation modes in MOFs including mode-field distributions, propagation constants, effective area, and dispersion in a range of wavelengths. With Matlab we simulate the propagation of light in MOFs with the properties previously determined with Comsol. With MPB we study the photonic bands of the cladding of MOFs that consist of photonic crystals.

3.1 Numerical methods for light propagation in fibres

In this section, we enumerate some methods used to study the propagation of light in optical fibres, especially for MOFs. Those methods are effective index, localized function expansion, plane wave expansion, multipole expansion, finite-difference time domain, finite-difference frequency domain, and beam propagation methods.

In the effective index method, the MOF is approximated as a step-index fibre. The method allows a quick estimate of the properties of the fibre, but it is not very accurate.

In expansion methods, the structure of the field is studied by considering a sum of periodic

functions: In the localized functions expansion methods, an expansion of the electromagnetic field is done over a theoretically infinite number of Hermite polynomials. In the plane-wave expansion methods, the simulations are done by operating in the reciprocal space of a periodic lattice. This method is particularly useful for finding the band structures of photonic crystals and hollow-core MOFs. In the multipole expansion methods, the electric field is described as Fourier-expansions - this method is well suited for symmetrical structures with circular holes.

The finite element methods (FEMs) are all-purpose methods [119] and can be used for any geometry, however they are computationally high intensive. FEMs use a discretization of the problem, and approximate the equations that express the system with numerical model equations.

In finite difference time domain methods and finite difference frequency domain methods, Maxwell's equations are solved in order to find the propagation modes in waveguides. The beam propagation methods (BPMs) are a subclass of finite difference methods. In a BPM, the fibre length is divided into small discrete steps and the evolution is done in short simulation steps, which can be fixed or adaptative. For each step, the simulation is carried out by solving an equation derived from Maxwell's equations, such as the generalized nonlinear Schrödinger equation (GNLSE) - Eq. (2.24).

3.2 Modelling and simulation: programs

In order to study the time-independent properties we have used Comsol multiphysics software v4.2/5.1 [120], and MIT photonic bands (MPB) software [121] for achieving different but consistent results.

With Comsol multiphysics it is used the finite elements method. In practice, in Comsol multiphysics, the 2D cross-section of the fibre is divided into a mesh; the master equation, Eq. (2.17), is then solved applying scattering boundary conditions to determine the propagation modes: the propagation constant, the electric-field distribution, and the magnetic-field distribution.

With MPB software we can study periodic 2D photonic crystals in order to find their photonic bands. In MPB the fibre cladding is designed as a photonic crystal consisting of a unit cell and with a specific periodicity; then, the master equation, Eq. (2.17), is solved using periodic boundary conditions. With our MPB implementations the output consists on

the matrices with the photonic bands, and in addition the arrays with the density of states data.

Then for studying the nonlinear propagation we use a pseudo-spectral beam propagation method based on the one given in ref. [26]. For this purpose we have used Matlab (as well as C++).

3.2.1 Comsol multiphysics and livelink™

With Comsol, our calculations of the propagation modes follow the following steps: set-up the model's parameters; create the geometry; add the materials; generate the mesh; set up the physics; find the solutions; and post-analyse the data.

In Comsol models for MOFs a very important input is the refractive index and how it varies with the spatial coordinates and with the wavelength: $n(\lambda, \mathbf{r})$. We shall include the geometry's parameters in the model; we can also calculate parameters given by the result of functions, such as the refractive index, $n(\lambda)$, of the fibre's core and the fibre's cladding materials, which is computed using the Sellmeier expression.

In order to draw the geometry's components, graphical operations and/or mathematical functions may be used. Amongst the possible methods for drawing fibre components we can define basic figures (such as circles, squares, etc.), and we can do graphical operations (such as forming arrays of figures, doing unions, or intersections, etc.). In addition, for drawing complex designs such as the LS-MOF, or even the simple air suspended core fibre, it is possible to define parametric curves delimiting each zone (Fig. 3.1).

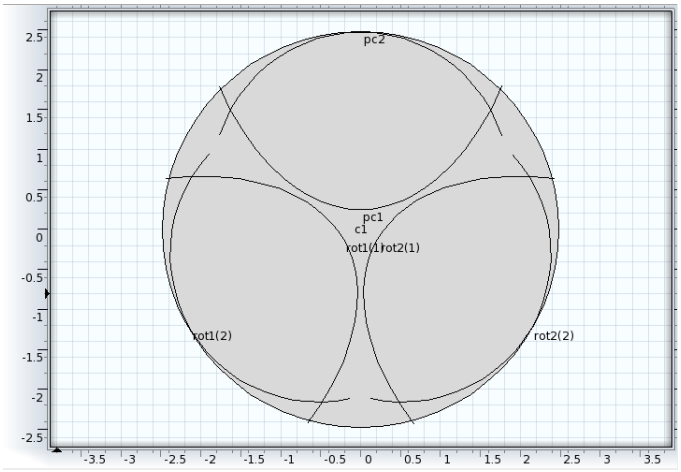

Fig. 3.1: Schematic figure with parametric curves for the drawing of an air-suspended core fibre.

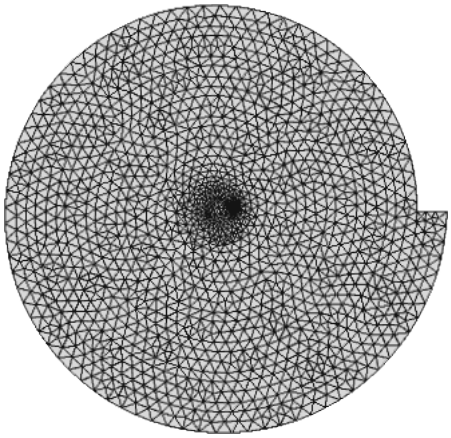

Fig. 3.2: The mesh used in this work for a layered spiral MOF (LS-MOF), with triangular sub-regions.

We may use the materials of the Comsol libraries; however, it is better to define our own materials, and associate to them refractive indexes that depend on the wavelength, $n(\lambda)$, which is not generally the case in Comsol libraries. The only input for the master equation is indeed $n(\lambda, \mathbf{r})$, and for HC-MOFs filled with gases we can also add the pressure and the temperature dependences of the refractive index.

We usually used a user-defined mesh, choosing a finer mesh for the core such as the "extra-fine", and a coarser mesh for the cladding. In geometries with many details, if their design is not in the form of a xy grid, as it is the case of our MOF designs, then the triangular meshes are often recommended. In Fig. 3.2, we observe an example with a fibre whose mesh was considered as a triangular mesh - in this case a LS-MOF (layered spiral MOF) was assumed.

Then, we choose to solve the master equation using the study step of "mode analysis" for electromagnetic waves; additionally, we add scattering boundary conditions.

In order to find the solutions, we have to give the program an initial guess of n_{eff}, which we do through the parameter of "search_for_modes_around". For the first computed modes we can insert the n_{core} as that initial guess, which works well for SC-MOFs. However if HC-MOFs are studied using that initial guess, then the computing time will be very large and the output for a particular wavelength will contain confined solutions (i.e. the two orthogonal fundamental modes), and non confined solutions. Therefore, in order to increase the time performance and to dynamically choose the fundamental mode for each wavelength, we use Comsol livelink$^{\text{TM}}$ for Matlab: we export the model made with Comsol to a file with the extension ".m", in which we can make editions or add our own code to the model; then we run the final code with the Comsol livelink$^{\text{TM}}$ and Matlab. In our simulations, we have

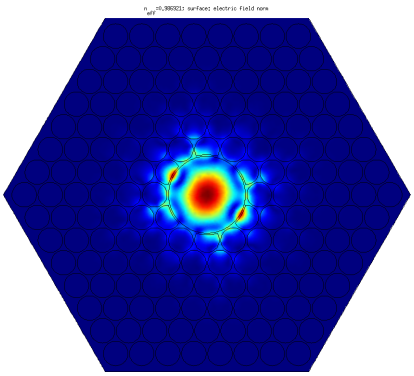

Fig. 3.3: The fundamental mode at λ=790nm of an HC-MOF, $r/a = 0.47$, and $a = 1.7\lambda$.

defined the parameter of "search_for_modes_around" as:

$$search\_for\_modes\_around = n_{\text{HC}} - (n_{\text{HC, neighbour}} - n_{\text{eff, neighbour}}), \tag{3.1}$$

where n_{HC} and $n_{\text{HC, neighbour}}$ are the refractive indexes of the hollow-core at the actual and the previous wavelengths respectively, and $n_{\text{eff, neighbour}}$ is the n_{eff} of the computed mode at the previous wavelength. In addition, a matrix with representative points of the electric-field, $e_{\text{field}}(x, y)$, for each found mode is analysed: the fundamental mode is selected by choosing the mode whose $max(e_{\text{field}}(x, y))$ occurs closest to the origin, where the centre of the fibre core is located. In addition, if the radius of the points with maximum electric-field, $r_{max\{e_{field}\}}$, is the same for different modes we select the mode with the smallest effective mode area.

The output is one mode for each λ, consisting in a $e_{field(x,y)}$ distribution.

Fig. 3.3 shows the optical field distribution of the fundamental mode, for a fibre with radius of holes r, and pitch a. We observe that the mode is confined in the core, thus the light can be guided through the fibre's core.

3.2.2 Matlab /C++

In order to solve the GNLSE, we use a pseudo-spectral method that is a modified version of the freely-available beam propagation method presented in ref. [26, chapt. 3].

For that purpose, we re-write the GNLSE, Eq. (2.24), in the frequency domain:

$$\begin{aligned} \frac{\partial \tilde{u}(z,\omega)}{\partial z} - i\left[\beta - \beta_c - \beta_1(\omega-\omega_0) + \frac{\alpha(\omega)}{2}\right]\tilde{u}(z,\omega) = \\ = i\gamma\left(1+\frac{\Delta\omega}{\omega_0}\right)\mathcal{F}\left\{u(z,\tau)\int_{-\infty}^{\tau} R(\tau')|u(z,\tau-\tau')|^2 d\tau'\right\}, \end{aligned} \tag{3.2}$$

where $\tilde{u}$ is the Fourier transform of u, and $\mathcal{F}$ denotes the Fourier transform. Eq.(3.2) is theoretically identical to Eq. (2.24) for an infinite number of β_k terms. However, solving Eq. (3.2) is more accurate than solving Eq. (2.24) for a finite number of β_k terms. The adopted pseudo-spectral method requires that the GNLSE be in the form of an ordinary differential equation. For that purpose we multiply all the terms by $e^{-\hat{l}z}$ where $\hat{l}$ is a linear operator given by $\hat{l} = i[\beta - \beta_c - \beta_1(\omega - \omega_0)]$, so that we can recognize the derivative of a product and we can rewrite Eq. (3.2) in the form:

$$\frac{\partial}{\partial z}\left[\tilde{u}(z)e^{-\hat{l}z}\right] = \tilde{v}(z)e^{-\hat{l}z}, \tag{3.3}$$

where we have defined $v(z,t) = i\gamma\left(1 + \frac{\Delta\omega}{\omega_0}\right)\left(u(z,t)\int_{-\infty}^{t} R(t')|u(z,t-t')|^2 dt'\right)$, and $\tilde{u}$ and $\tilde{v}$ denote Fourier transforms.

Eq. (3.3) can be solved by ordinary differential equation (ODE) techniques, since it is mathematically in the form of a ODE in z for $\tilde{u}(z)e^{-\hat{l}z}$.

In order to solve Eq. (3.3) we make the following steps:

- 1. do the Fourier transform of u and of v at $z_0 = 0$;

- 2. solve the ordinary differential Eq. (3.3), by a initial value method, getting $\tilde{u} = \mathcal{F}\{u\}$, at $z = z_j$;

- 3. come back to the initial domain, doing inverse Fourier transforms, obtaining u and v at $z = z_j$;

- then, the steps 1-3 are repeated until the program reaches $z = z_{\text{final}}$.

We have implemented additional features such as the inclusion of random noise, the usage of different types of dispersion definitions, admitting the existence of a pressure gradient, the computation of photon number, X-FROG traces, and coherence. We have implemented from source the main parts with C++, because C++ is faster and can be run from our computers network.

Initially, we start by defining our time grid points, which shall be high enough to give high-precision results, but not too high for not consuming to much cpu-time or cpu-memory. In order to verify the stability of the precision of the code for different input time-grids and z-steps for each model, the conservation of photon number was analysed: we have selected results in which the photon number variation was only of $\leq 0.1\%$, such as in Figs. 3.4-3.5. In these figures, the fibre's parameters were core diameter d_f=40μm with kagomé pattern, and the considered laser has a sech shape with FWHM of 40fs, energy of 10μJ, λ=0.790μm. The

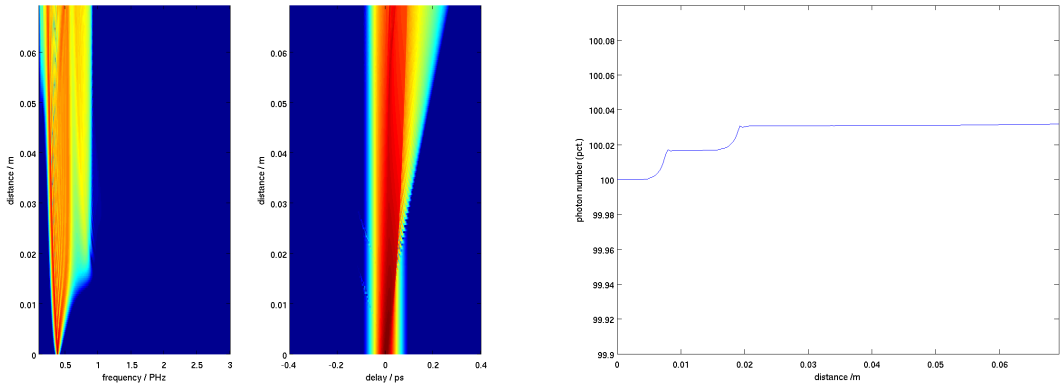

Fig. 3.4: Pulse propagation along a HC-MOF filled with 40bar of argon, and the numerical photon number evolution along the fibre.

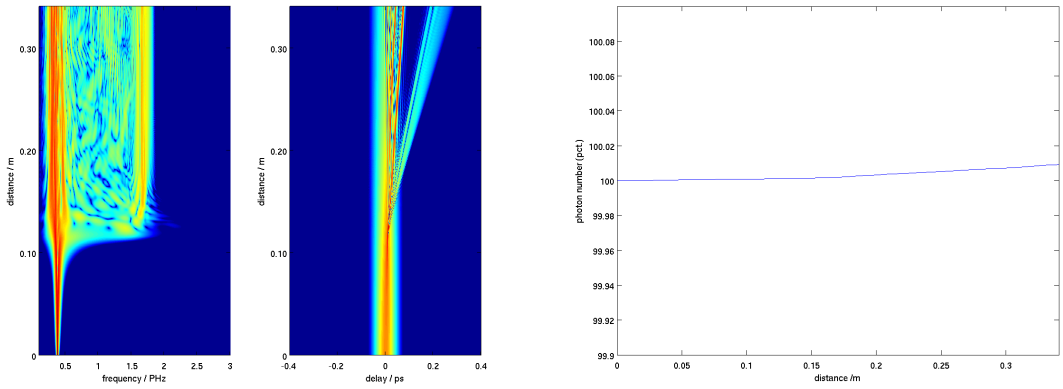

Fig. 3.5: Pulse propagation along a HC-MOF filled with 40bar of helium, and the numerical photon number evolution along the fibre.

fibre's core was filled with a noble gas (in the 1st case argon, and in the 2nd case helium, both with 40bar). The conservation of the photon number corresponds to a conservation of energy, where the photon number is given by:

$$\#p(z) = \sum_{i=1}^{n} |u(t)_i|^2 \Delta t \tag{3.4}$$

and the variation of the photon number in percentage along the time t is the quotient:

$$\#p(z)_{\%} = \frac{\#p(z)}{\#p(z=0)} \times 100.0\% \tag{3.5}$$

The input pulse is described by three main parameters: the full width at half maximum (FWHM), the energy, and its central wavelength, as well as by a specific shape. In our simulations we have used an hyperbolic secant as the input pulse shape, with the optional

addition of random noise.

The input profile of a perfect laser could be a hyperbolic secant function, or a Gaussian function, etc. However in practice, the pulse profile contains some noise, which deviates itself from the pure form.

For a hyperbolic secant input pulse, given by: $a = \sqrt{p_{\text{peak}}}\text{sech}(t/t_0)$, we have that the input in practice is of the form:

$$a = \sqrt{p_{\text{peak}}}sech(t/t_0) + f_{\text{noise}}, \tag{3.6}$$

where p_{peak} is the peak power of input, t_0 is the pulse width, with t_0=FWHM/1.762747, and f_{noise} is the function that describes the noise.

For adding the quantum noise, it is first considered that the photon number follows a Poissonian distribution with mean $\langle n \rangle$ and standard deviation $\sqrt{\langle n \rangle}$ [68, chapt. 5]. The normalized complex amplitude of the optical field, a, is the square root of power, thus $a(i)$ at each temporal mesh point i and $n(i)$ are related by:

$$a(i) = \sqrt{p(i)} = \sqrt{n(i)hc/(dt\lambda_0)} \tag{3.7}$$

where p is the power, h is the Plank's constant, c is the speed of light in the vacuum, λ_0 is the centre wavelength, and dt is the time step of integration.

The square root of a Poissonian variable has a Gaussian distribution with standard deviation equal to one-half; hence, after some calculations, the following result for the quantum noise is obtained:

$$f_{\text{noise}} = \frac{1}{2}\sqrt{hc/(dt\lambda_0)}\text{randn}(), \tag{3.8}$$

where randn() is a vector with dimension $1 \times n$, containing pseudo-random values drawn from the standard normal distribution (which has mean at 0 and standard deviation equal to 1). An example of an input pulse described by this approach is presented in Fig. 3.6, without and with quantum noise.

The coherence results show the sensitivity of the output due to differences in the input pulses due to random noise. The coherence of the pulse spectrum at the position z, $g^{(1)}(\lambda, z)$, is computed according to the following definition [24]:

$$g^{(1)}(\lambda, z) = \frac{|\,\langle E_a^*(\lambda, z)E_b(\lambda, z)\rangle\,|}{\sqrt{\langle|E_a(\lambda, z)|^2\rangle\,\langle|E_b(\lambda, z)|^2\rangle}} \tag{3.9}$$

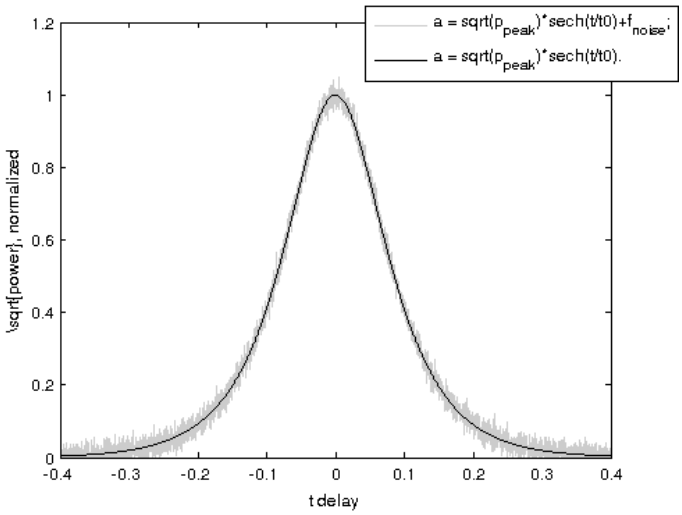

Fig. 3.6: Input profile, with and without quantum noise.

where E_a and E_b denote two outputs resulting from two independently generated inputs with random noise, and the angle brackets denote an average over a set of pairs. The coherence of light propagation profiles depends upon the relationship between the conditions of different pairs of events where the differences are due to the input random noise.

Before the propagation simulations, we have to obtain the fibre properties: effective area, dispersion, fibre length, and losses. The effective area is computed from the Comsol results. We have introduced the dispersion through three alternative methods: i) a Taylor series for β accordingly to Eq. (2.29), ii) a fit to Comsol data with standard matlab routines, and iii) a theoretical formula for models such as the kagomé filled with gases whose dispersion depends on pressure. When the Raman related effects are relevant (i.e. for most of the cases, except for noble gases) we need to introduce the Raman response of the fibre's core filling material.

We then proceed by solving the GNLSE through Eq. (3.3). We have used two methods for solving this problem: i) the ode45() routine of Matlab which has an adaptative step size, and ii) the RK4 method with a fixed step size. The ode45() method has the advantage of adapting the step-size by checking during the computations which is the best step-size to ensure the desired accuracy, however it has a more unpredictable running time compared to the RK4; RK4 has a more predictable and stable running time than ode45(), due to its fixed conditions such as the step-size and orders of the equations (4th order), and with RK4 we can have more insight on what are the numerical settings used in our simulated cases, since the details are manually specified by us; in fact, for the same running time usually ode45() is more accurate since it automatically distributes the spent time according to each step of the

problem but we cannot know the total running time before running the problem; with RK4 we can achieve also identical results by changing the value of the step which is maintained through all the problem, but it can be more slow.

Finally, we plot our final graphs: the spectral intensity along z, the temporal profile along z, the coherence, and the X-FROG traces.

3.2.3 MPB - MIT photonic bands

In order to study the properties of a photonic crystal, i.e. a medium with a certain periodicity in the distribution of the electric permittivity, we can use the MPB - MIT photonic bands, a software developed in MIT with an interface with the Scheme (or Python) language[1].

The fibre's cladding of a hollow core MOF is an instance of a photonic crystal since it is periodic, and therefore it can be analysed with MPB software. In fact, the periodicity of those fibres' cladding is the key factor that leads to light guidance in the fibre's core material.

In order to study a photonic crystal we can analyse its unit cell, and use periodic boundary conditions. In fact the HC-MOFs studied in this work include the hexagonal HC-MOF (also called honeycomb HC-MOF), and the kagomé HC-MOF, which have an unit cell in the form of a hexagon, because the smallest region that is periodically repeated along the material with the maximum number of symmetrical operations is a hexagon. The design of the unit cell must be described using a vector basis that is not the usual Cartesian basis. The primitive cell of a hexagonal lattice has specific primitive vectors, a_i.

Fig. 3.7.a) shows the unit cell built on the primitive space of a kagomé lattice and/or a hexagonal lattice, where the primitive lattice vectors are $\mathbf{a_1} = \left(\frac{\sqrt{3}}{2}, \frac{1}{2}\right)$, and $\mathbf{a_2} = \left(\frac{\sqrt{3}}{2}, -\frac{1}{2}\right)$. Thus, the normalised Cartesian base vectors may be written with respect to $\mathbf{a_1}$ and $\mathbf{a_2}$ by: $\mathbf{e_x} = \frac{1}{\sqrt{3}}\mathbf{a_1} + \frac{1}{\sqrt{3}}\mathbf{a_2}$, and $\mathbf{e_y} = \mathbf{a_1} - \mathbf{a_2}$. From the primitive lattice vectors we can deduce which are the reciprocal lattice vectors (appendix A.5), by the relation:

$$2\pi \left(\begin{bmatrix} \frac{\sqrt{3}}{2} & \frac{\sqrt{3}}{2} \\ \frac{1}{2} & \frac{-1}{2} \end{bmatrix}^T \right)^{-1} \underset{\rightarrow}{\overset{}{=}} \begin{bmatrix} \frac{1}{2} & \frac{1}{2} \\ \frac{\sqrt{3}}{2} & \frac{-\sqrt{3}}{2} \end{bmatrix}.$$

Thus, for the hexagonal unit cell the resulting reciprocal lattice vectors are: $\mathbf{b_1} = \left(\frac{1}{2}, \frac{\sqrt{3}}{2}\right)$, and $\mathbf{b_2} = \left(\frac{1}{2}, -\frac{\sqrt{3}}{2}\right)$ [Fig. 3.7.b)]. The points Γ, M, and K form the polygonal line Γ-M-K-Γ

[1]Recently an interface with a more user-friendly language, i.e. the Python language, was released, at 2018/06/08.

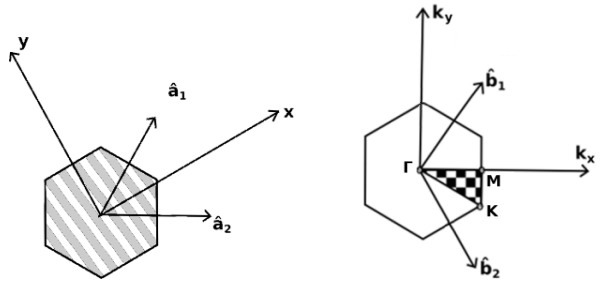

a) b)

Fig. 3.7: a) The unit cell of a HC-MOF with hexagonal lattice in the real space; b) the unit cell of a HC-MOF with hexagonal lattice in the reciprocal space.

which delimits the shading sub-region of that cell – the so called irreducible Brillouin zone, i.e. a sub-zone which contains all the information that is repeated in the other sub-zones of the cell [54] [Fig. 3.7.b)].

We define the main k-points of the system (i.e. Γ, M, and K) with the command "set! k-points()", in MPB. If we consider a hexagonal lattice, those k-points in the basis b_i are:

$\Gamma = (0, 0)$

$\mathrm{M} = (0, 0.5)$

$\mathrm{K} = (-1/3, 1/3)$

and we also define a set of points all of them in the boundary of the irreducible Brillouin zone.

Within the MPB, after defining the unit cell's basis vectors, we design the structure of the unit cell and the dielectric permittivity of each region. Then, for a list of k-points in the boundaries of the irreducible Brillouin zone, we compute the photonic levels. This is done by computing the photonic bands of two distinct types of polarization: the transverse electric (TE) modes, for which the electric-field is parallel to the xy plane, and the transverse magnetic (TM) modes, for which the magnetic field is parallel to the xy plane. The TE and TM bands can be shown separately [Fig. 3.9.a)-b)], or superimposed [Fig. 3.9.b)].

The graphs presented in Fig. 3.9 were obtained by reproducing a case study of the MPB data analysis tutorial [121, MPB-website], searching for modes that have $k_z = 0$. The graphs represent the frequency f normalized by a factor versus the (k_x, k_y) along the line that delimits the irreducible Brillouin zone. In the diagram of TM bands, gaps from f=0.275 to f=0.446 are noticeable, as well as from f=0.564 to f=0593; on the other hand, in the diagram of TE bands a small gap from f=0.822 to f=0.864 exists.

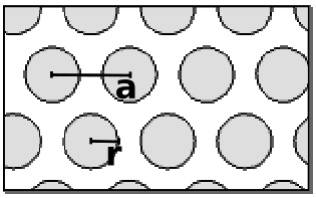

Fig. 3.8: Scheme of a photonic crystal with rod radius r, and lattice period a.

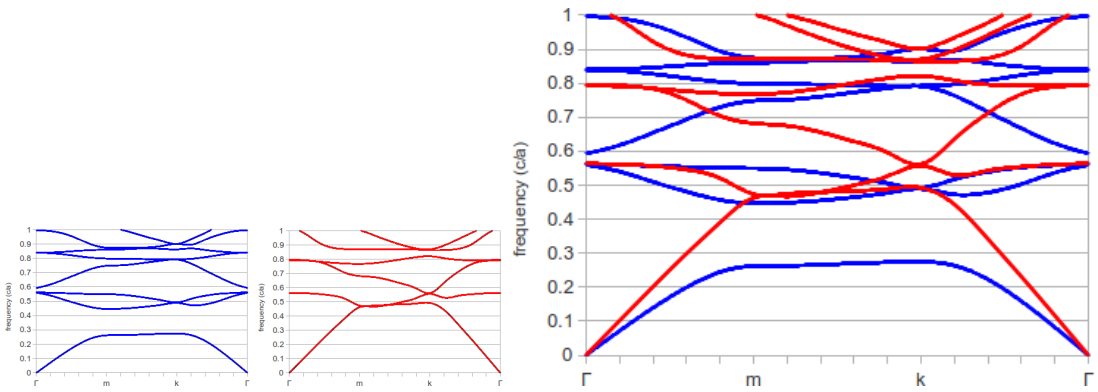

a) b) c)

Fig. 3.9: a) Transverse magnetic (TM) bands; b) transverse electric (TE) bands; c) superposition of TM and TE bands for $k_z = 0$. The photonic crystal considered here is the one represented in Fig. 3.8 with r/a=0.2, and refractive index of the rods n=3.46, in air for $k_z = 0$.

The photonic band structures for HC-MOFs which we are interested in are the ones corresponding to non-zero values for k_z, since those are the modes that may couple with the usual propagation modes in the core. For a given k_z, all the propagation modes can be classified into a superposition of two distinct types of polarization: the TE modes, and the TM modes.

We can then generalize the previous model to include modes with nonzero k_z. We set the main k-points as triplets:

$\Gamma = (0, 0, k_{\mathrm{zMPB}})$

$\mathrm{M} = (0, 0.5, k_{\mathrm{zMPB}})$

$\mathrm{K} = (-1/3, 1/3, k_{\mathrm{zMPB}})$

where k_{zMPB} is the adimensional k_z given by:

$$k_{\mathrm{zMPB}} = k_z \frac{a}{2\pi}. \tag{3.10}$$

We can then obtain the photonic bands for the cladding of a HC-MOF for various distinct k_z as shown in Fig. 3.10. In Fig. 3.10.a), the total bands correspond to a superposition of both the TE and TM bands.

From photonic bands data, for various k_z, such as the set represented in Fig. 3.10.a), we can compute the projected bandgaps or the density of states (DOS) of that fibre's lattice as is explained schematically in the same figure. For computing the bandgaps, for each k_z we determine the minimum and maximum frequency of each band; the band indicates the frequency range at which there are TE or TM states. In Fig. 3.10.b)-c) we observe the projected bandgaps and the DOS for k_z in the range $\{0.0,\ 3.0\ 2\pi/\mathrm{a}\}$. In Fig. 3.10.b), black regions represent the bandgaps and the white regions represent bands of allowed states in the fibre's cladding. This type of graph is called the projected bandgaps diagram.

There is a MPB routine which uses the previously computed data to compute the density of states (DOS), at a particular point (k_z, f). The density of states is computed by summing Gaussian smoothing functions centered at each k-point for each particular frequency value. For each pair (k_z, f) there is a DOS value, which is plotted in Fig. 3.11, where we observe the DOS values for a hexagonal hollow core fibre, at some specific k_z. In Fig. 3.11 we observe that there are two regions for which the density of states is zero: the 1st zone at bottom due to the material line, and a 2nd at the middle that corresponds to the bandgap in Fig. 3.10. Then, by varying k_z we can obtain the data that produce Fig. 3.10.c), where black regions

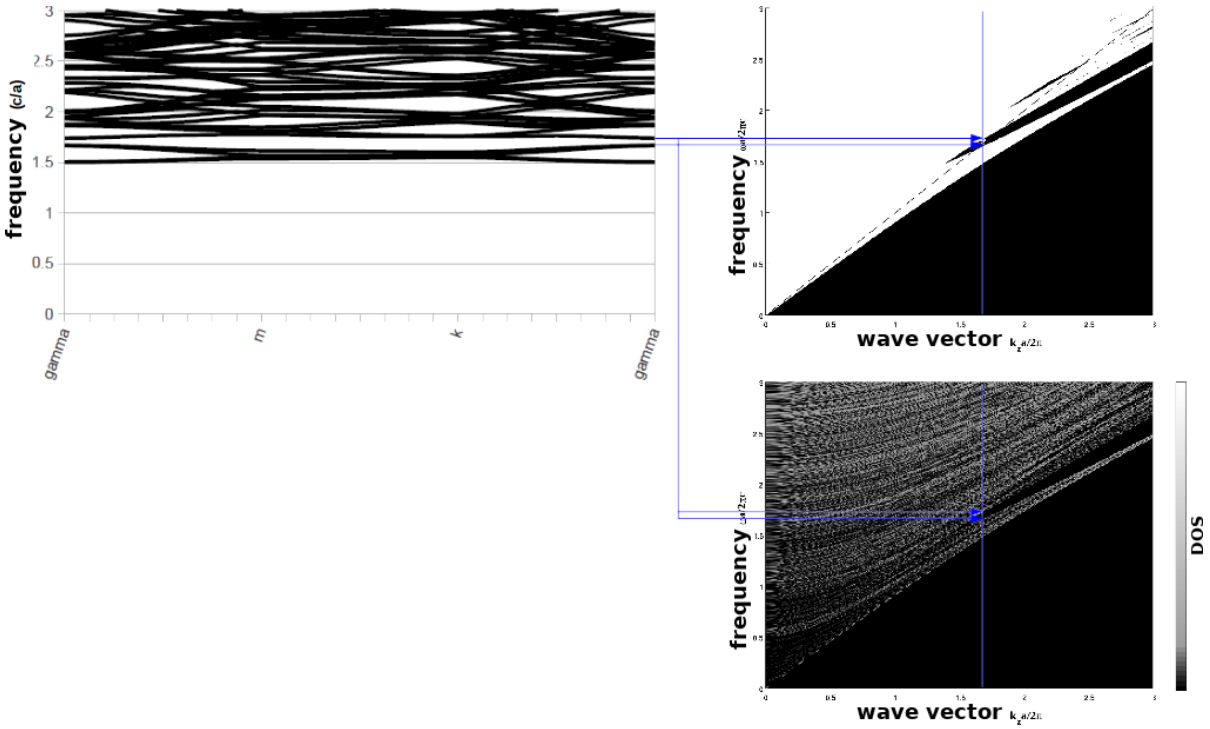

Fig. 3.10: a) left: photonic bands (both TE and TM) for a hexagonal lattice with circular air rods and silica glass, with r/a=0.47, for k_za/(2π)=1.7; b) top-right: projected bandgaps diagram for the same conditions; c) bottom-right: DOS graph for the same conditions.

correspond to forbidden states (i.e. DOS=0), and gray to white regions correspond to low and high DOS$\neq$ 0, respectively.

In order to find the regions of photonic bandgap guidance, we must search for graph's zones at which light states are allowed in the core and simultaneously forbidden in the cladding.

If the core is filled with a material having refractive index n, the allowed states in it should have a frequency larger than:

$$\omega = \frac{c}{n} k_z. \tag{3.11}$$

In the case of air, this line is called the air line, and it is represented in Fig. 3.10.b) by a dashed line. For noble gases, since $n \approx 1$, this line is approximately the same as the air line. For any confined mode that propagates in the core filled with air its frequency should be inside a bandgap of the cladding and above the air line.

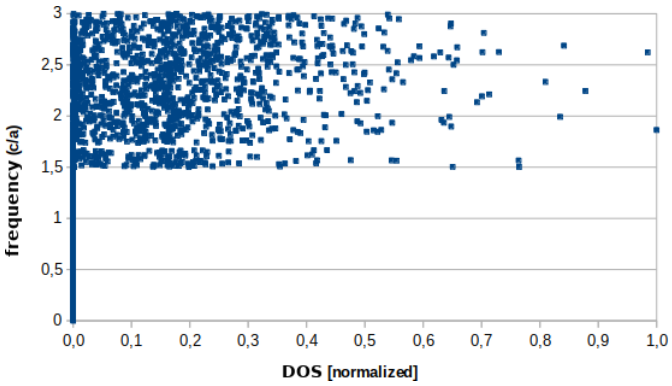

Fig. 3.11: Normalized density of states for $k_z a/(2\pi)$=1.7.

3.3 Summary

The structure of microstructured optical fibres makes the problem of finding their modes more complicated than that of standard single mode fibres, and thus numerical methods are necessary. For that purpose we have used a commercial software, Comsol multiphysics, applying the procedure described in this chapter. To solve the GNLSE in order to find the evolution of a pulse propagating along the fibre we used a pseudo-spectral method implemented in Matlab using: the ode45() routine with an adaptative step-size, and a 4th order Runge-Kutta method, RK4() [88], with a fixed step-size. The photon number was computed in order to check for pulse propagation conditions with the desired accuracy. In order to obtain the photonic bands of the fibre's cladding, we used the MIT photonic bands (MPB) software applying a procedure also described in this chapter.

4 NONLINEAR EFFECTS IN MICROSTRUCTURED OPTICAL FIBRES

In this chapter, we will see that by changing the fibre's design we can change its dispersive and nonlinear characteristics even without changing the materials, in particular at telecommunication wavelengths. We will describe different SC-MOFs in terms of dispersion and nonlinearity. In particular, we will study the layered spiral microstructured optical fibre (LS-MOF), with which we can have a very high nonlinearity.

In this chapter, we will also explore nonlinear effects in HC-MOFs, especially nonlinear light propagation that gives rise to supercontinuum generation or UV light generation. We will study the honeycomb fibre and then we will extensively analyse the HC-kagomé fibre.

4.1 Solid-core microstructured optical fibres

The SC-MOFs include a wide range of models, as presented in chapt. 2. Here, we will focus on the hexagonal SC-MOF and on the layered spiral SC-MOF. We will observe that by changing the geometry of the fibre, the dispersion can be adjusted, and the nonlinear effects can be reduced or increased. The layered spiral SC-MOF is a model with which we achieve the goal of combining adjustable dispersion and high nonlinearity. We will observe SCG in those fibres at various pumping wavelengths, and we will in particular adjust the fibre's properties for light propagation at 1.55μm.

4.1.1 SC-fibres properties

An hexagonal SC-MOF is a fibre such as the one represented in Fig. 4.1, whose parameters are the hole's diameter, d, and the hole pitch, Λ. The cores's diameter corresponding to this fibre's design is $2\Lambda - d$. Throughout this work we have considered that the core radius value of a MOF is approximately equal to the value of the radius of the circle inscribed on the fibre's core. We will show that the properties of SC-MOFs can be adjusted by changing the characteristic parameters of those fibres.

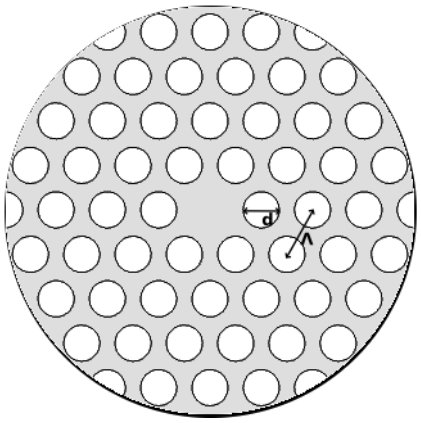

Fig. 4.1: Design of a hexagonal HC-MOF, with the indication of its two main parameters: d: the holes diameter, and Λ: the holes pitch.

We need to describe the distribution of the refractive index, n, in the transverse section of the fibre to obtain the fibre's properties. In particular, in the following the refractive index of silica, n_{SiO2}, was calculated with a Sellmeier equation (appendix A.3)[31, chapt. 2]:

$$n = \sqrt{1 + \sum_j \frac{a_j \lambda^2}{\lambda^2 - b_j}}. \tag{4.1}$$

For the silica material the coefficients taken correspond to 3 terms: a_1=0.6965325, a_2=0.4083099, a_3=0.8968766, b_1=0.004368309, b_2=0.01394999, and b_3=97.93399, [82, chapt. 3]. For the SF57 glass, the coefficients were taken from ref. [122]. For the arsenic trisulfide, the coefficients were taken from ref. [107].

We have studied the effect of changing the two parameters of the hexagonal SC-MOF. Figs. 4.2-4.3 show that we can vary the dispersion and the effective mode area by changing the pitch or the holes diameter. We note the possibilities of achieving two zeros of dispersion or a flat dispersion. In particular, for a fixed Λ, by increasing d/Λ the effective mode area is lower since the air filling fraction of the cladding increases; however, the dispersion tends to

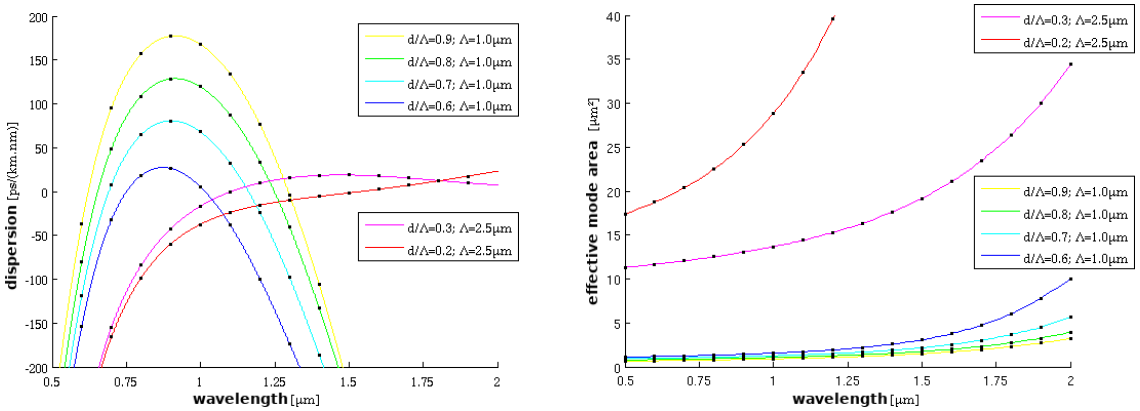

a) b)

Fig. 4.2: Dispersion curves (a), and effective mode area (b) for various fibre parameters: pitch, Λ, and holes diameter, d.

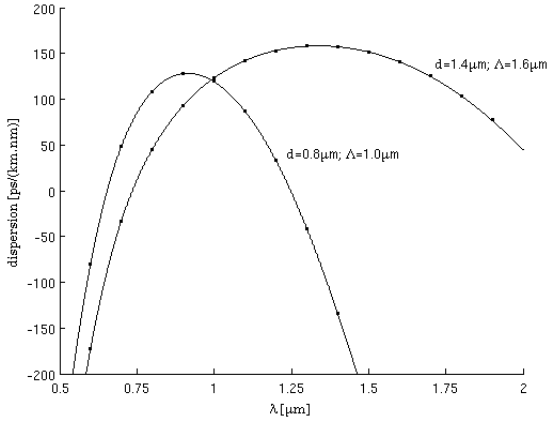

Fig. 4.3: Dispersion curves for two different microstructured fibers with a hexagonal pattern of holes, with distinct hole's diameter, d, and distinct hole's pitch, Λ.

increase in these conditions. In addition, it can be noted that the conditions for flat dispersion correspond to a higher effective mode area. This is due to the fact that for achieving flat dispersion it is necessary a small contrast between the refractive indices of the cladding and of the core, whereas for achieving high nonlinearity that contrast shall be high.

In order to obtain a flat dispersion profile it is possible to adjust the radius of the fibre's holes. We have achieved a very flat dispersion curve, as shown in Fig. 4.4. The considered fibre has different holes diameters for each fibre's cladding ring around the core, with values as suggested in ref. [95]: from inside to outside, the diameters are d1=0.47μm, d2=0.71μm, d3=0.74μm, d4=0.62μm, d5=... =d10=0.65μm, and the hole pitch is 1.60μm. The dispersion profile of this fibre has values between 0.0 and 0.3ps/(km.nm), in the wavelength range from 1.41μm to 1.68μm. This is very good for some types of applications, for example to implement devices to realize optical signal processing based on four wave mixing effect. However, the

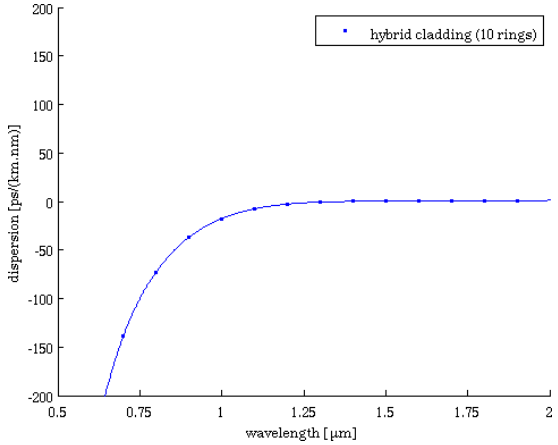

Fig. 4.4: Dispersion curve for a flat profile with the hole diameters with different diameters, whose values are given in the text.

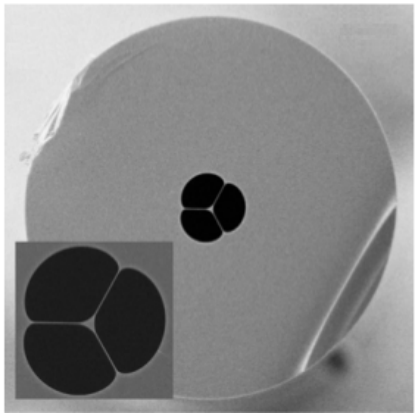

Fig. 4.5: SEM image of a air suspended core fibre, after ref. [28]

effective mode area is not adjusted simultaneously so that the nonlinear parameter is relatively low.

For comparison purposes we will analyse the air suspended core (ASC) fibre, whose design can be seen on Figs. 4.5, 4.6. The scanning electron microscopy (SEM) image of an air-suspended core (ASC) fibre [28] is presented in Fig. 4.5. The fundamental modes for two ASC fibres can be seen in Fig. 4.6, where in a) the fibre is composed by arsenic trisulfide (n=2.437) and air, and in b) the fibre is composed by SF57 (n=1.802) and air.

The differences between cases a) and b) are due to the different index contrast between the core materials, arsenic trisulfide vs SF57, and the cladding material, air. When the refractive index contrast between n_{core} and $avg(n_{cladding})$ is higher the mode is more confined in the fibre's core. In Fig. 4.6, the effective refractive index obtained in our simulations for arsenic trisulfide was n_{eff}=2.157, whereas for SF57 the value was n_{eff}=1.326.

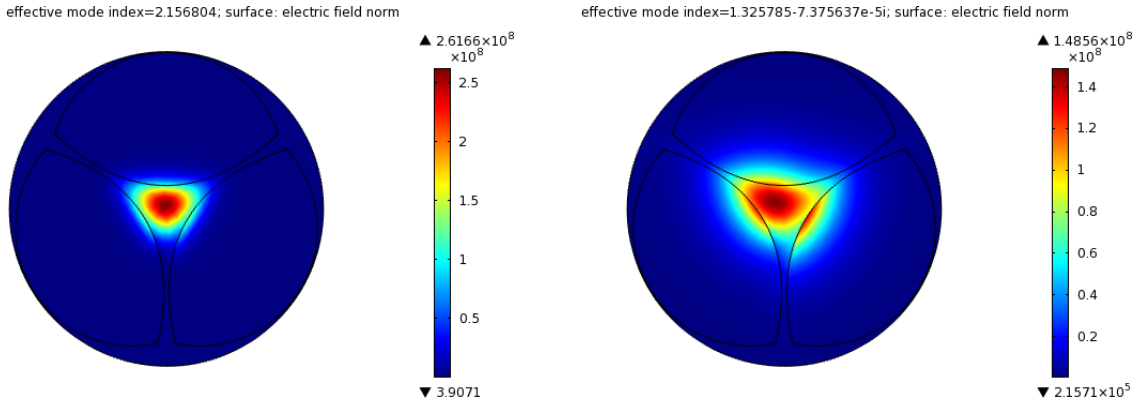

Fig. 4.6: The fundamental propagation mode for ASC fibres, at 1.550μm, with core radius $r_{co} = 0.4\mu$m for: a fibre composed by arsenic trisulfide and air, and a fibre composed by SF57 glass and air.

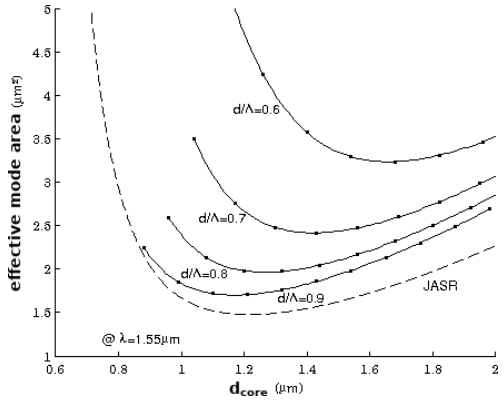

Fig. 4.7: The effective mode area, at 1.55 μm, as a function of the fibre's core diameter: the continuous traces are for SC-MOFs with different parameters; the dashed trace is for a JASR; the fibres considered here are all composed by silica and air.

The ASC fibres are amongst the fibres with highest nonlinearity. These fibres, provide a high contrast between the refractive index of the fibre's core and of the fibre's cladding, that together with a small core area lead to a high nonlinear parameter. However ASC fibres do not permit a flexible tailoring of the dispersion because their microstructred design is relatively simple. For a jacket air suspended rod (JASR) fibre, which is a step-index fibre with glass in the core and air in the cladding, when composed by a silica core the value of fibre's core diameter that leads to minimum a_{eff} is of approximately 1.20μm, for λ=1.55μm [33, 35] (see Fig. 4.7).

In particular, the dispersion of ASC fibres composed by different solid-core materials such as the arsenic trisulfide glass and the SF57 glass, which are highly nonlinear materials, are shown in Fig. 4.8. We observe the transition from anomalous dispersion to normal dispersion

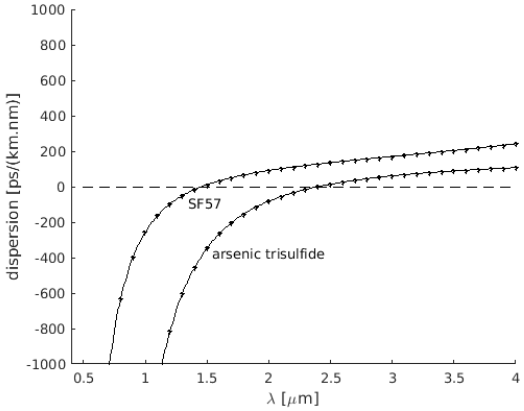

Fig. 4.8: The dispersion for ASC fibres, for: a) fibre composed by arsenic trisulfide and air; b) fibre composed by SF57 glass and air, with d_{core}=3.4μm.

for wavelengths at the middle of the graph: for the considered ASC fibre with arsenic trisulfide the ZDW is at 2.40μm, whereas with SF57 the ZDW is at 1.46μm.

We have studied the effect of changing the two parameters of the hexagonal SC-MOF. We have observed that for intermediate values with pitch and wavelength of the same magnitude (i.e. $\lambda \approx$1.55μm) the effective mode area can be minimized, as shown in Fig. 4.7. In this figure, we include the properties of two types of fibres: the hexagonal SC-MOF, and the jacker air suspended rod (JASR). By varying the radius of the JASR or by varying the pitch of a hexagonal SC-MOF we note that there is a minimum value for the modal radius; in addition the modal radius decreases when we have a higher ratio for d/Λ. In the region of the minimum modal radius, the nonlinear effects are stronger. The region of the d_{core} at each side of the graph are well-suited for different applications: the left-side for sensors, the middle-side for nonlinear effects and generation of signals, and the right-side for transmission.

With the aim of creating a highly nonlinear medium we have proposed a new fibre design that we have called the layered spiral microstructured optical fibre (LS-MOF) [92]. The transversal section of the LS-MOF is shown in Fig. 4.9. In this design, there is one turn of an equiangular spiral given by:

$$r(\theta) = a\mathrm{e}^{b\theta} \tag{4.2}$$

with $a = r_i$ and $b = \log(r_f/r_i)/2\pi$, which limits the core of the MOF. Its enclosed circle has a radius equal to r_i, which is here used as a measure of the core size. The cladding consists of several turns of solid regions confined in between two Archimedean spirals given by:

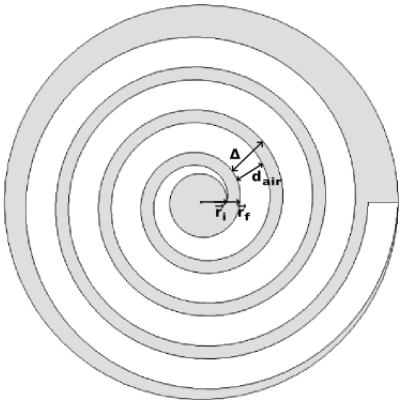

Fig. 4.9: LS-MOF design, where the grey regions correspond to glass, and the white regions to air; its three main parameters are d_{air}, Δ, and r_i (see the text for details).

$$\begin{aligned} r_{\text{in}}(\theta) &= r_f + \Delta\theta/(2\pi), \theta \in [0, (n-1)2\pi]; \\ r_{\text{out}}(\theta) &= r_i + \Delta\theta/(2\pi), \theta \in [0, n2\pi]; \end{aligned} \tag{4.3}$$

where n is the number of layers. The parameter Δ represents the spatial period of the air/solid layers on the cladding. The LS-MOF structure will be parametrized by r_i, Δ, and by the relative air layer thickness, d_{air}/Δ, where $d_{air} = \Delta - (r_f - r_i)$. The quantity d_{air}/Δ corresponds to the cladding's percentage of air.

By manipulating the location of glass strands in the LS-MOF, we may mainly control the dispersive properties; by adjusting the thickness of these strands we change significantly both the dispersive and the nonlinear properties of the fibre. This geometry has an important limiting case, when $d_{air}/\Delta \to 1$ which corresponds to a fibre with 100% air filling fraction in the cladding that allows a particularly high nonlinear parameter. In addition, the radius of the fibre's core is another parameter which can be adjusted independently.

With a careful adjustment of the LS-MOF parameters we have found a zero dispersion at 1.546μm, for r_i=0.6μm, d_{air}/Δ=0.7 and Δ=1.0μm, as discussed in ref. [92]. In addition, we have achieved a zero dispersion with a vanishing first derivative near 0.650μm for r_i=0.3μm, d_{air}/Δ=0.7 and Δ=0.6μm. The dispersion and effective mode area in these situations are shown in Fig. 4.10, where the circle corresponds to the zero dispersion point. The mode field profile at λ=1.55μm is given in Fig. 4.11.

We have made a computational analysis of the LS-MOF for finding conditions for ZDWs at 1.55μm. The Table 4.1 summarizes our results. We have chosen $r_i = 0.6\mu m$ in order to minimize the effective mode area. Then, for each air filing fraction, we vary the Δ parameter which manipulates the distribution of the regions of air and silica, and consequently vary

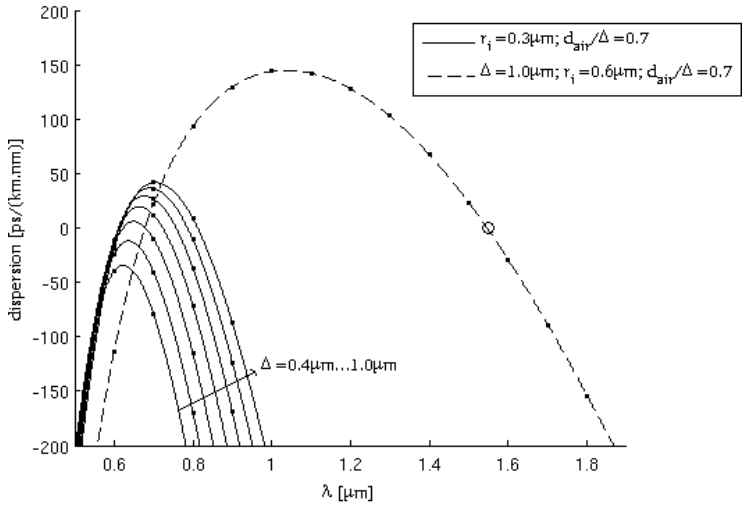

a)

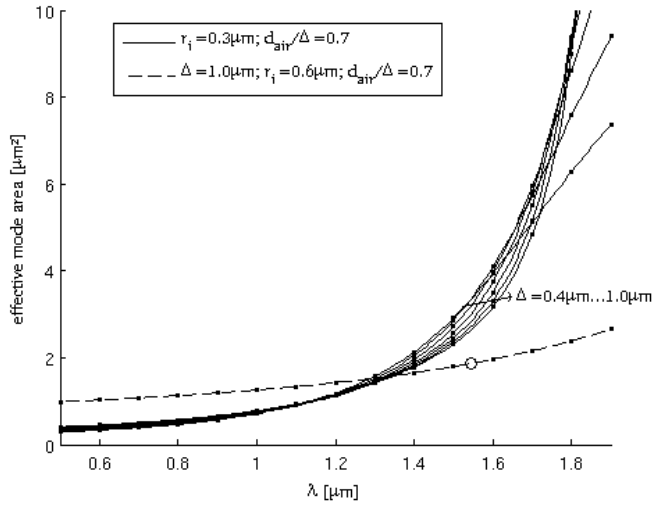

b)

Fig. 4.10: a) Dispersion curves, b) effective mode area, for the LS-MOF with the indicated parameters

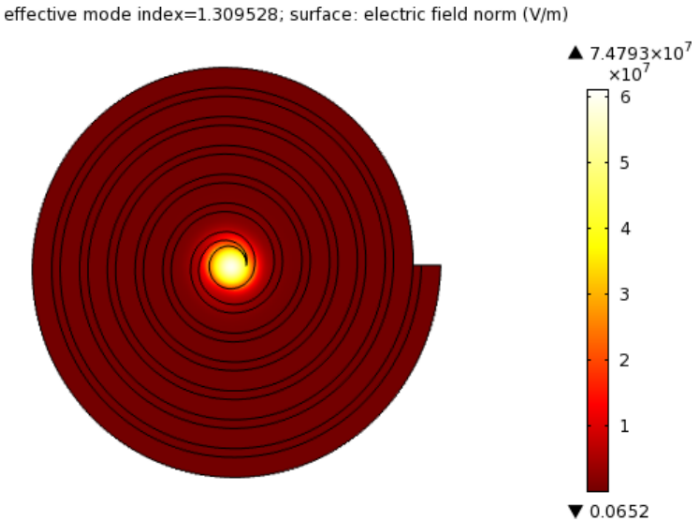

Fig. 4.11: Mode field profile of the fundamental propagation mode for a LS-MOF, composed by silica and air, at 1.55μm, with r_i=0.6μm, d_{air}/Δ=0.7, and Δ=1.01μm, at which the dispersion is zero.

the dispersion. Zero dispersion cases were obtained for the parameters in the 1st column; in the 6th row, for AFF=90.0%, we achieve a nonlinear parameter of 70.0W^{-1}km^{-1}, with simultaneously zero dispersion.

In addition, we have also studied the LS-MOF composed by arsenic trisulfide and air in order to achieve an adequate dispersive curve and a high nonlinear parameter. The ideal value of r_i is related to the properties of a JASR, which corresponds to the theoretical limit of a LS-MOF when $d_{air}/\Delta \to 1$. Fig. 4.12 shows the dependence of the effective mode area and group velocity dispersion with the core radius of an arsenic trisulfide JASR, for $\lambda = 1.55\mu m$. We see that the minimum a_{eff} is achieved for $r_i = 0.32\mu m$. However, at this value of r_i the GVD is very high, so we have chosen $r_i = 0.40\mu m$ in order to obtain a lower value of dispersion, despite its slight deviation from the minimum of a_{eff}.

For d_{air}/Δ we have chosen a value of 0.9, which is a value that is close to the maximum air filling fraction (AFF), but it still has the strands that support the core and allow the adjustment of the dispersion. The LS-MOF with these parameters seems feasible in practice, in the future. Note that whenever we increase the AFF the nonlinearity becomes higher due to the enhanced contrast between the refractive indices of the core and the cladding, leading to a stronger confinement of the light. In addition, we have chosen a value of $\Delta = 1.0\mu m$, with which we have anomalous dispersion at the reference wavelength of $1.550\mu m$. Note that by choosing other values of Δ, $d_{air}/\Delta < 1.0$, or r_i we can change the location of the ZDWs

parameters of the geometry	air filling fraction	dispersion at 1.55µm [ps/(km.nm)]	effective area at 1.55µm [µm^2]	nonlinear paramater at 1.55µm [W^{-1}.km^{-1}]
r_i=0.6µm, d_{air}/Δ=0.4; Δ=1.525µm	40.0%	0.0	3.72	28.3
r_i=0.6µm, d_{air}/Δ=0.5; Δ=1.311µm	50.0%	0.0	2.77	38.1
r_i=0.6µm, d_{air}/Δ=0.6; Δ=1.014µm	60.0%	0.0	2.22	47.4
r_i=0.6µm, d_{air}/Δ=0.7; Δ=1.01µm	70.0%	0.0	1.88	56.0
r_i=0.6µm, d_{air}/Δ=0.8; Δ=0.950µm	80.0%	0.0	1.66	63.5
r_i=0.6µm, d_{air}/Δ=0.9; Δ=1.048µm	90.0%	0.0	1.50	70.0
r_i=0.6µm, d_{air}/Δ=1.0; Δ=0.400µm [JASR]	100.0%	-63.4	1.39	76.0

Table 4.1: The results of our rigorous modelling of a LS-MOF composed by silica and air showing dispersion, effective mode area, and nonlinear parameter at 1.55μm.

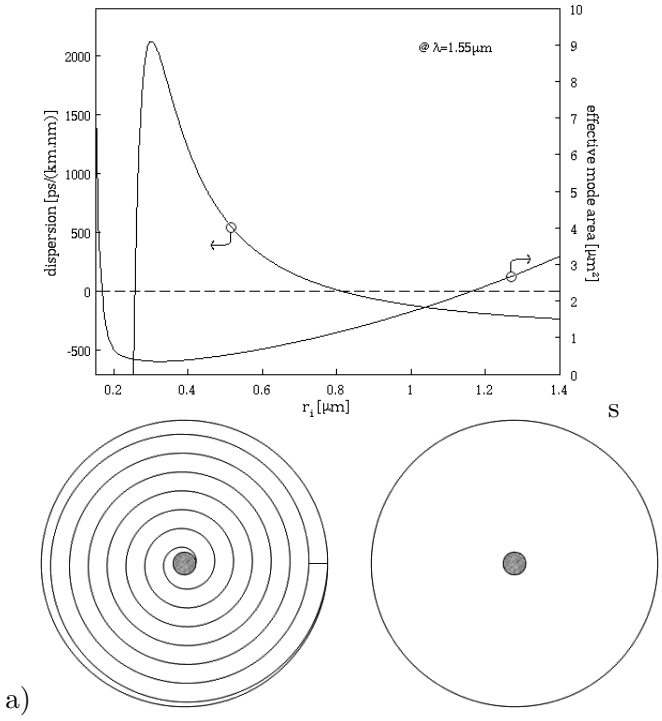

Fig. 4.12: a) Effective mode area and dispersion curves versus the core radius of a JASR, for $\lambda = 1.55\mu m$, with arsenic trisulfide core; b) schemes showing the theoretical limit of a LS-MOF when $d_{air}/\Delta \to 1$, which is the JASR.

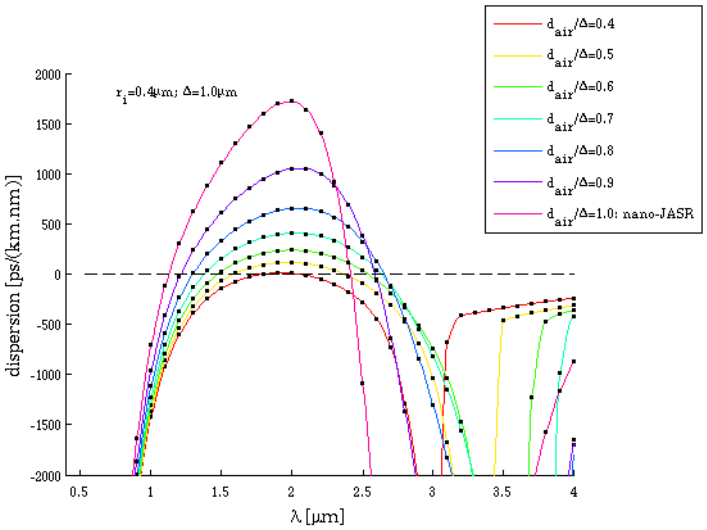

Fig. 4.13: Dispersion of an LS-MOF made of arsenic trisulfide for $r_i = 0.4\mu m$, $\Delta = 1.0\mu m$, and several values of d_{air}/Δ.

of the LS-MOF.

In Fig. 4.13 we show the GVD of the LS-MOF as a function of wavelength, for several values of d_{air}/Δ up to the limit $d_{air}/\Delta = 1$, which corresponds to 100% of AFF. We see that by increasing the air filling fraction the maximum dispersion in the anomalous region becomes higher, due to the increased waveguide dispersion contribution determined by the higher contrast between the refractive indices of the core and the cladding.

Fig.4.14 illustrates the nonlinear parameter, γ, as a function of frequency. In fact, we confirm that when the air filling fraction is increased the nonlinearity of the fibre also increases. The line in Fig. 4.14 of $d_{air}/\Delta = 0.9$ corresponds to our choice, and the star indicates the nonlinear parameter value $\gamma = 50.7\mathrm{W}^{-1}\mathrm{m}^{-1}$, obtained at $1.55\mu m$. Note that this value of the nonlinear parameter was found in the anomalous dispersion region of the fibre.

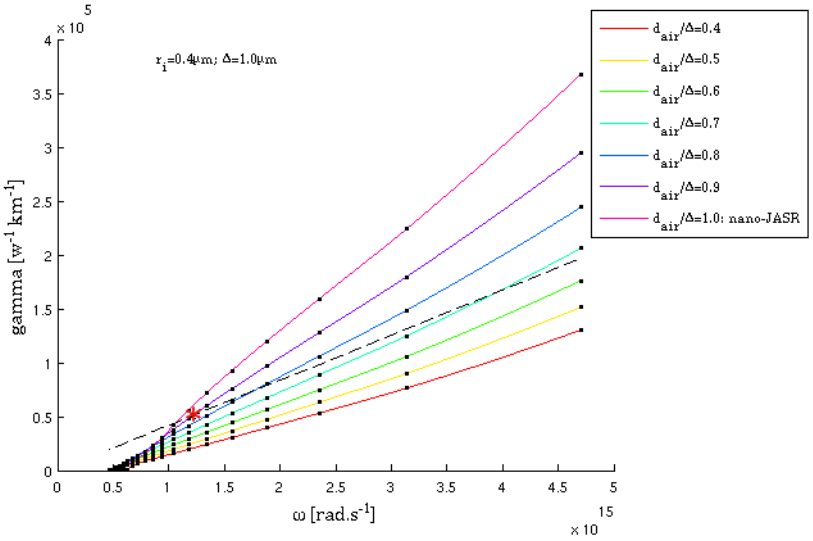

Fig. 4.14: Nonlinear parameter, γ, of an arsenic trisulfide LS-MOF for $r_i = 0.4\mu m$, $\Delta = 1.0\mu m$, and several values of d_{air}/Δ; for details about the dashed line see the text.

4.1.2 Light propagation in hexagonal fibres - SCG

In order to study the pulse propagation in SC-MOFs we start by considering a hexagonal fibre with: d=1.4μm, Λ=1.6μm [whose dispersion profile is shown on Fig. 4.3], and a hyperbolic secant pulse, described by sech u(0, τ)=$\sqrt{P_0}$sech(τ/t_0) with t_{FWHM}=1.762747t_0=25fs, P_0=5kW, at λ_{pump}=790nm. This fibre has a single zero dispersion wavelength at 735nm. The considered pumping is located in the anomalous dispersion regime, at which the soliton dynamics has an important role, and in those conditions the nonlinear parameter is γ=117.0W^{-1}km^{-1}. For this fibre and pulse we have simulated the propagation with the full GNLSE equation, (2.24), whose results are shown in Fig. 4.15 For the assumed pulse and fibre parameters, the input pulse corresponds to a higher order soliton with n_{order}=2.81, and it has a fission distance $l_{\text{fiss}} \approx$ 0.48cm (see chapt. 2). In Fig. 4.15 we observe that new wavelengths are generated at both left- and right- hand-sides of the graph, which is due to the interplay between several phenomena. We note the appearance of solitons for higher wavelengths due to the SSFS caused by IRS, as well as the appearance of wavelengths at lower wavelengths due to the dispersive waves generation. The spectral width that is achieved can be observed at Fig.4.15.b), whose range goes approximately from 500nm to 1100nm.

We can numerically isolate some of the involved phenomena, by eliminating some of the terms in the GNLSE, Eq. (2.24). With that approach, we show the propagation results in four cases: a) with only 2nd order dispersion, and SPM, b) with 2nd order dispersion, SPM, and self-steepening (SST), c) with the presence of IRS but without higher-order dispersion,

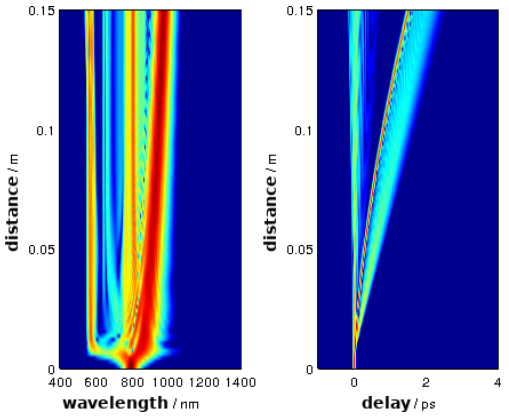

a)

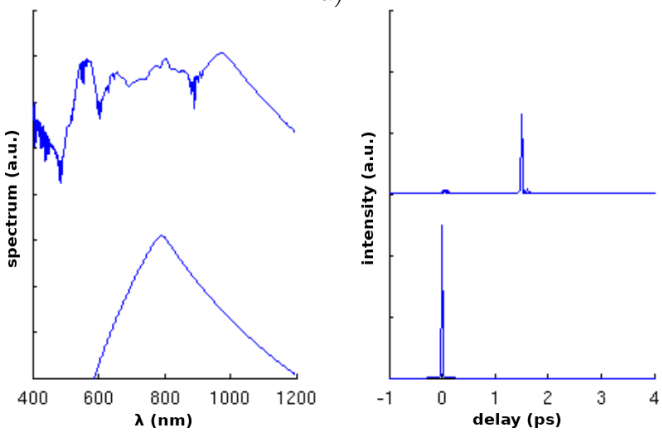

b)

Fig. 4.15: a) Spectral and temporal pulse evolution; b) Input and output pulses with the SCG effect, for a fibre with: d=1.4μm, Λ=1.6μm, P_0=5kW, t_{FWHM}=25fs, at λ=790nm.

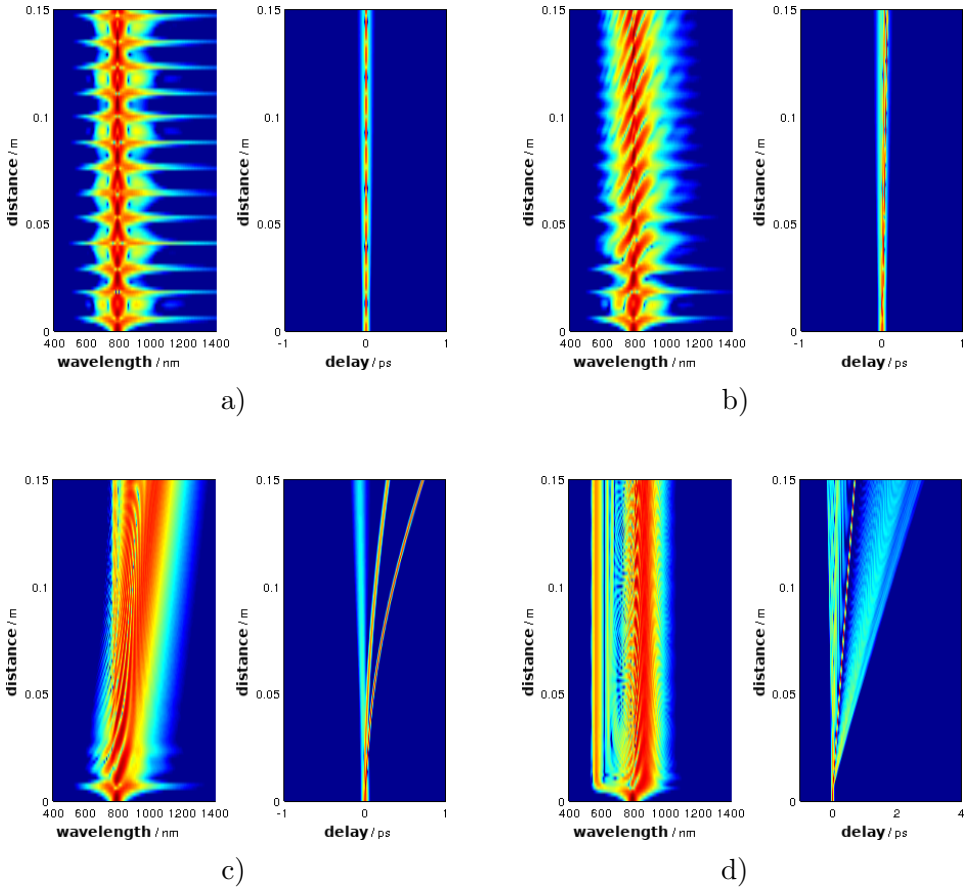

Fig. 4.16: Spectral and temporal evolution with partial effects for a fibre with: d=1.4μm, Λ=1.6μm, and a pulse with: P_0=5kW, t_{FWHM}=25fs, λ=790nm - a) with only 2nd order dispersion and SPM; b) with 2nd order dispersion, SPM, and with SST effect; c) in the presence of IRS and SST, but without higher-order dispersion; d) with higher-order dispersion terms and SST, but without IRS.

and with SST, and d) with higher-order dispersion terms but without IRS, and with SST. Those results are shown in Figs. 4.16.a)-d), respectively.

In Fig. 4.16.a) we observe a periodical evolution of the pulse, since the effects included in this simulation were only SPM and 2nd order dispersion, which act in alternate modes leading to the observed evolution. In Fig. 4.16.b) we have considered the same effects as in a) with the addition of the self-steepening effect. We note that with this perturbation the soliton does not exhibit a periodic evolution. The consequences of IRS on soliton fission can be seen in Fig. 4.16.c), where we may observe three individual pulses after the soliton fission. The solitons created by the fission process are then red-shifted due to the Raman effect, being called Raman solitons. The change of the soliton's frequency leads to a bending of the soliton trajectory in the time domain. In case of higher-order dispersion, when we neglect the IRS

contribution (Fig. 4.16.d)), the individual solitons resulting from the fission process are not apparent. Despite of that, the appeareance of a new spectral peak at $z = l_{\text{fiss}}$ is an indication of soliton fission. In the time domain we observe the spreading of a dispersive wave which propagates and it is separated from the main soliton. The new spectral peak present in d) corresponds to the so-called nonsolitonic radiation (NSR), which is emitted by the solitons in the presence of higher-order dispersion [3]. The NSR is emitted at a frequency such that the new phase velocity matches that of the soliton. The phase matching condition is given by[109]:

$$\beta(\omega) - \beta_c - \beta_1[\omega - \omega_s] = \gamma P_{\text{s}}/2, \tag{4.4}$$

where P_{s} is the peak power of the fundamental soliton generated by the fission.

The frequency shift, $\Omega = \omega - \omega_s$, can be obtained by neglecting the fourth- and higher-order dispersion terms, such that it is given by [31]:

$$\Omega \approx -\frac{3\beta_2}{\beta_3} + \frac{\gamma P_s \beta_3}{3\beta_2^2}. \tag{4.5}$$

In the anomalous-dispersion regime we have $\beta_2 <0$, and in that situation Eq. (4.5) shows that $\Omega <0$ when $\beta_3 <0$, and $\Omega >0$ when $\beta_3 >0$. Depending on the slope of the β_2 curve, the 1st case occurs when we are close to the 1st ZDW, such that the new frequencies are generated at the left of the spectrum; the 2nd case occurs when we are close to the 2nd ZDW, such that the new frequencies are generated ate the right of the spectrum.

In the fibre with d=0.8μm, spaced by Λ=1μm, of Fig. 4.3, there are two ZDWs, one at 654nm and the other at 1248nm, and the GVD is anomalous in the spectral window between them. In Fig. 4.17 we show the numerical results of pulse propagation in the anomalous dispersion region of this fibre by pumping at 860nm using 100fs pulses with a peak power of 1kW. Here, the GVD at the pump wavelength is β_2=-0.0472ps^2/m and the nonlinear parameter is γ=196.2W^{-1}km^{-1}, leading to a soliton order n_{order}=3.66. The obtained value for the fission length in this case is l_{fiss}=1.32cm, which is in agreement with the pulse evolution observed in the graph. By analysing this figure, we see that there is here a predominance of the IRS effect. We observe the fission of the pulse into four solitons, which is in agreement with the initial pulse order. The Raman solitons generated are different from each other, since they have different powers and different wavelengths. The pulse with highest power is the shortest and it is the one that suffers a larger deviation. The new wavelengths generated due to the IRS, are deviations into higher wavelengths. In the case of this figure, around the 2nd

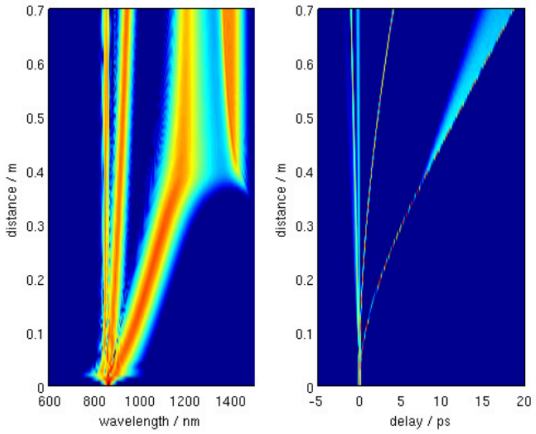

Fig. 4.17: (a) Spectral and (b) temporal evolution of 100fs pulses with a peak power of 1kW, at 860nm on a hexagonal fibre with d=0.8μm, spaced by Λ=1μm.

ZDW the β_3 signal is negative, and therefore the NSR appears at the right hand-side. When the pulse is almost reaching the region surrounding the 2nd ZDW, the detuning between the radiation and the soliton gets smaller with the propagation, which leads to an exponential amplification of the radiation. Then, due to the energy conservation the SSFS is cancelled, such that the propagation of pulses in those conditions leads to the so-called recoil effect, which is clearly observed here.

In order to compute the coherence we have used Eq. (3.9). For this purpose, we have to do multiple runs of the pulse propagations. We must compare the differences between two elements of each pair, and also evaluate all the pairs results, as indicated in the formula. As much as we have more quantities of pairs, the coherence at each (x, y) point converges to its expected value, where x is wavelength, and y is the distance across the fibre. Fig. 4.18.a)-b) show the spectral, temporal and coherence evolution of a pulse in a hexagonal SC-MOF, with: d=1.4μm, Λ=1.6μm, P_0=5kW, λ=790nm, and: a) t_{FWHM}=100fs; b) t_{FWHM}=400fs. In the case of shorter pulses, they get temporally compressed so quickly that the soliton fission process dominates the initial dynamics. In this case, the spectral extent of the developing supercontinuum can overlap with the frequencies of maximum modulation instability gain before significant amplification of the noise background occurred. However, in the case of longer pulses, modulation instability amplified noise becomes a dominant feature. Such amplified noise is random and can induce soliton fission even before other perturbations such as higher-order dispersive and nonlinear effects become significant. In that case, soliton fission occurs randomly and fission products are completely incoherent.

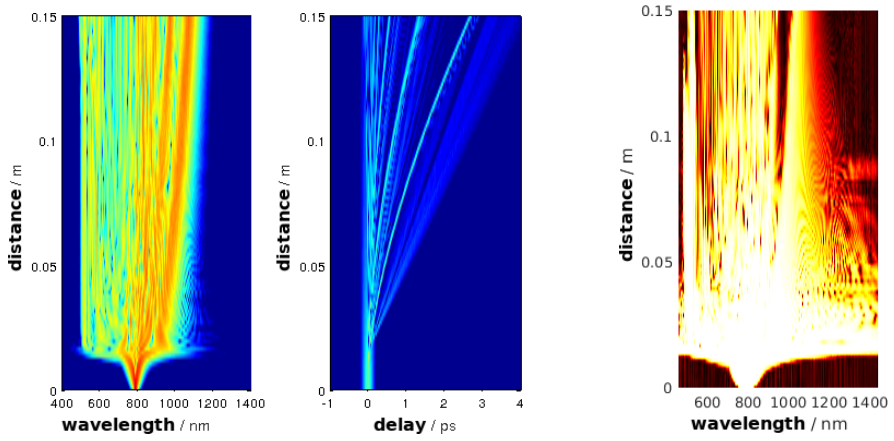

a)

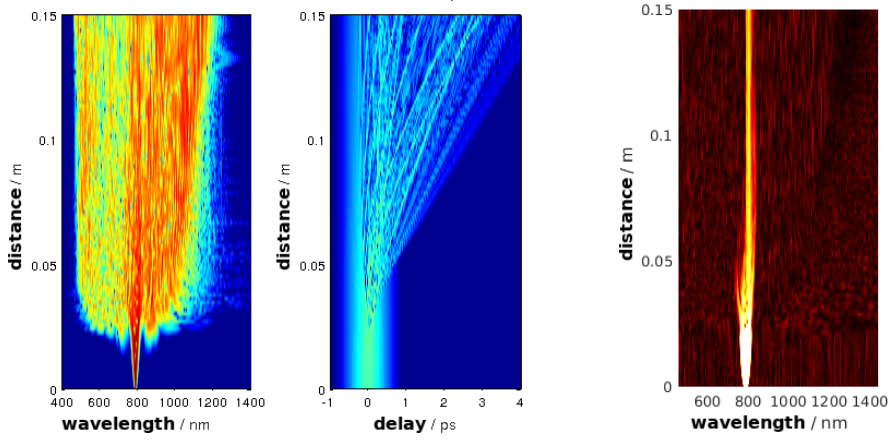

b)

Fig. 4.18: Spectral, temporal and coherence evolution of a pulse in a hexagonal SC-MOF, with: d=1.4μm, Λ=1.6μm, P_0=5kw, λ=790nm, and: a) t_{FWHM}=100fs; b) t_{FWHM}=400fs.

4.1.3 Light propagation in LS-MOFs - SCG

For enhancing the supercontinuum effect, we shall consider a pumping wavelength on the anomalous dispersion region, or close to a ZDW at the normal dispersion region.

In Fig. 4.19.a)-b) it is illustrated the supercontinuum generation, obtained considering a LS-MOF with the parameters r_i=0.6μm, d_{air}/Δ=0.7 and Δ=1.0μm, composed by silica and air. The corresponding curve for the dispersion is presented in Fig. 4.10, which exhibits two zero dispersion wavelengths: one at 0.679μm, and the other at 1.546μm. The pumping was assumed at 0.780μm (in the anomalous dispersion region), using 50fs sech pulses with a peak power P_{peak}=10kW. The corresponding nonlinear parameter has a value of 187.1W^{-1}km^{-1}.

When we include the self-steepening term, in a first approximation, the parameter γ is readjusted to:

$$\gamma \rightarrow \gamma_0 \left(1 + \frac{\omega - \omega_0}{\omega_0}\right). \tag{4.6}$$

However, we note that the function in Eq. (4.6), which is represented in the dashed line in Fig. 4.14 for $d_{air}/\Delta = 0.9$, is different from the real data. The 1st derivative of the γ function is:

$$\gamma' = \gamma_0 \frac{1}{\omega_0} = \gamma_0 \tau_{shock}, \tag{4.7}$$

such that $\tau_{shock} \approx \frac{1}{\omega_0}$ corresponds to the approximated curve in the dashed line, where ω_0 is the frequency associated with $\lambda = 1.55\mu$m and γ_0 is the corresponding nonlinear parameter. We can correct the τ_{shock} value in order to adjust it to the data, such that:

$$\tau_{shock} = \frac{F}{\omega_0}, \tag{4.8}$$

where F represents the factor between the derivative of the real curve (continuous) and the derivative of the approximated curve (dashed). Here, we have determined that $F = 1.6524$.

In Fig. 4.19.c)-f) we observe the separate effects of the higher order dispersion terms and IRS term. We note that the IRS is mainly responsible for the long-edge of new wavelengths, whereas the higher-order dispersion is responsible for both short- and long-edges of new wavelengths. The inclusion of both effects leads to the light propagation shown at Fig. 4.19.a)-b). In addition to the referred effects, there is also usually the occurrence of wave mixing and cross phase modulation (XPM) which even though being weaker lead also to spectral broadening.

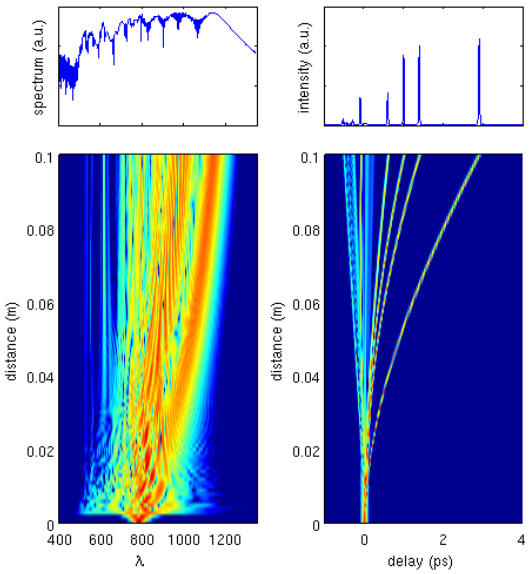

a)-b)

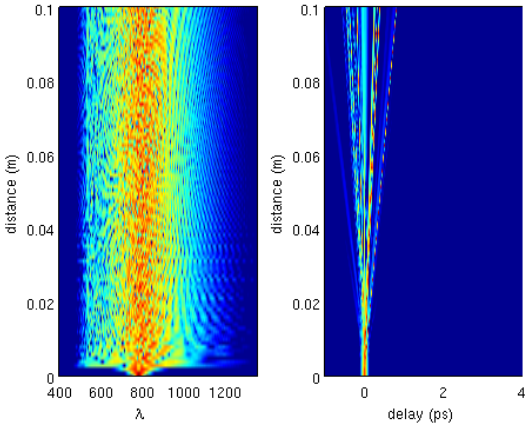

c)-d)

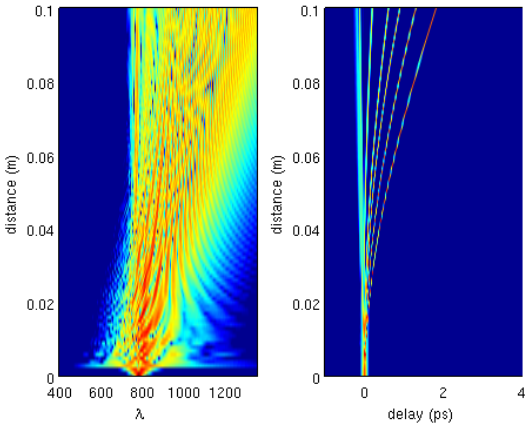

e)-f)

Fig. 4.19: Spectral and temporal evolutions of a)-b) supercontinuum generation in a LS-MOF; c)-d) isolation of dispersion, including higher-order dispersion; e)-f) isolation of Raman; in these cases a pump wavelength of λ=780nm, t_{FWHM}=0.05ps, and P_0=10kW were used, and the fibre parameters are those referred in the text.

We can notice that the spectrum is significantly broadened both to the left- and to the right-hand sides of the pumping wavelength, extending from ∼700nm to ∼1200nm, as a result of the soliton dynamics and dispersive wave generation. The initial pulse corresponds to a soliton of order n_{order}=7.1, which disintegrates under the soliton fission phenomenon. The fundamental solitons generated in this process are subsequently red-shifted under the action of the IRS effect.

In the following we report our studies of SCG in a LS-MOF with arsenic trisulfide and air, with the fibre's parameters of: $r_i = 0.4\mu m$, $\Delta = 1.0\mu m$, and $d_{air}/\Delta = 0.9$. The Raman effect of arsenic trisulfide was included taking into account Eq. (2.28) and the parameters of ref. [117]: τ_1=15.2fs and τ_2=230.5fs.

Using a pumping wavelength of $1.06\mu m$, which is in the normal dispersion region, we have $\beta_2 = 0.36\text{ps}^2/\text{m}$, and $\gamma = 89.7\text{W}^{-1}\text{m}^{-1}$. We have considered input pulses with a hyperbolic secant shape of 0.1kW of peak power and a temporal duration of 100fs. We observe a moderate spectral broadening in these conditions [Fig. 4.20.a)]. Despite of the high value of γ, the conditions for the supercontinuum generation with the considered fibre at this wavelength are not favourable since the dispersion is normal and the pump wavelength is not very close to the ZDW.

The results in Fig. 4.20.b) were obtained considering a pumping wavelength at $1.55\mu m$. We observe a large spectral broadening in a very short length of fibre: 1mm. In these conditions we have anomalous dispersion with $\beta_2 = -0.88\text{ps}^2/\text{m}$, a nonlinear parameter $\gamma = 50.7\text{W}^{-1}\text{m}^{-1}$, for which the 0.1KW peak pulse corresponds to a soliton order of 7.6. The characteristics of this supercontinuum are mainly determined by solitonic effects and dispersive wave generation. Here, the soliton self frequency shift (SSFS) effect is not clearly observable because the Raman effect is relatively weak. In this figure, the dispersive waves appear at the left-hand side ($\lambda = 0.450\mu m$) and at right-hand side ($\lambda = 3.790\mu m$) because we are pumping in the anomalous regime in the middle of the two ZDWs.

We have simulated also the pulse propagation for a pumping wavelength of $\lambda = 2.50\mu m$, as shown in Fig. 4.20.c). In this case, we have anomalous dispersion, with $\beta_2 = -1.27ps^2/m$, $\gamma = 15.0\text{W}^{-1}\text{m}^{-1}$, and a soliton order of 3.5 for the 0.1kW peak power. A large spectral broadening also occurs in these conditions. In this case, the dispersive waves appear only at the right-hand side, because of the proximity of the pump wavelength with the second ZDW.

The output spectra resulting from input pulses of different peak powers, centered at 1.55μm, propagating in a 1mm-long LS-MOF are shown in Fig. 4.21. We see that, by

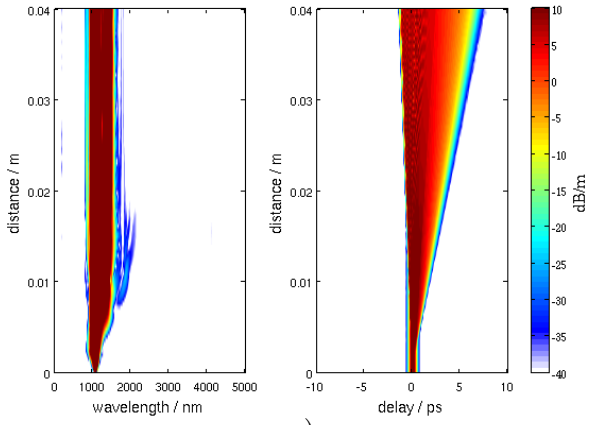

a)

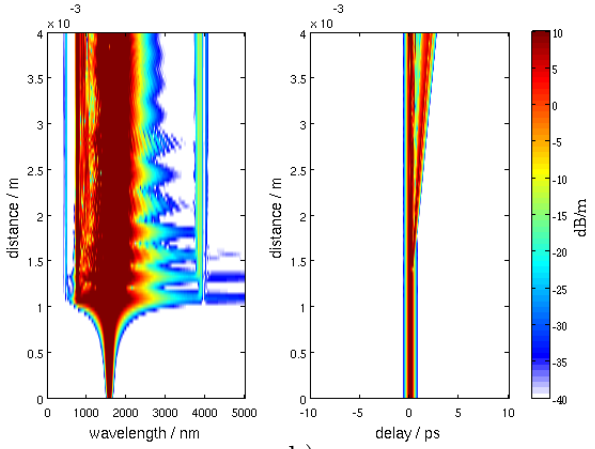

b)

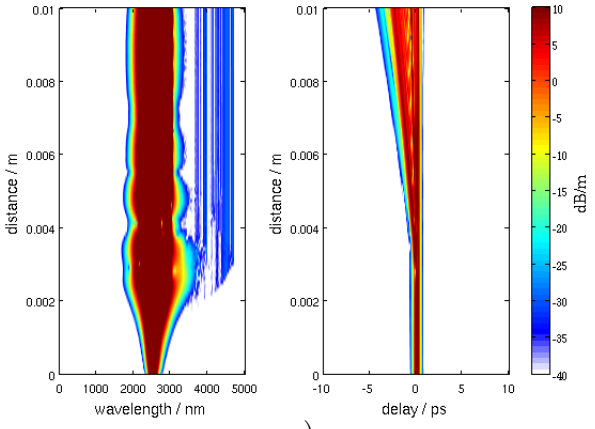

c)

Fig. 4.20: Supercontinuum generation in a highly nonlinear LS-MOF composed by arsenic trisulfide and air, with fibre's parameters $r_i = 0.4\mu$m, $\Delta = 1.0\mu$m, and $d_{air}/\Delta = 0.9$; the pumping pulse has a peak power of 0.1kW, pulse temporal duration of 100fs, and wavelength of a) 1.060μm, b) 1.550μm, and c) 2.500μm.

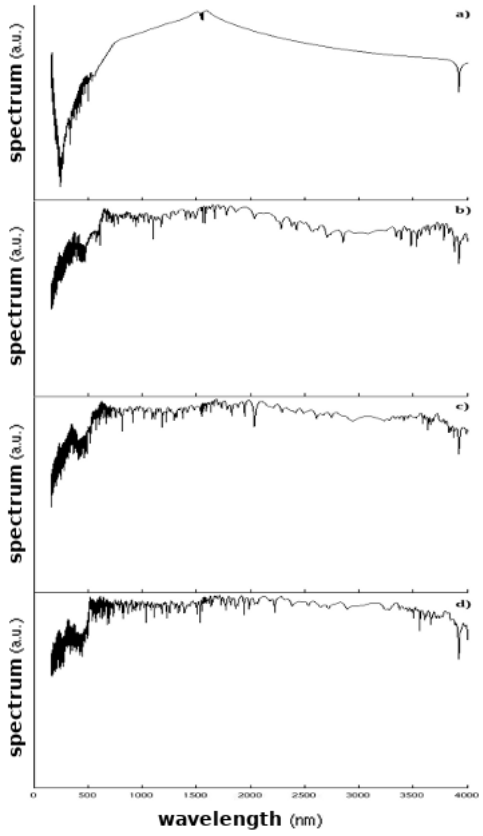

Fig. 4.21: Output of the supercontinuum generation in a highly nonlinear LS-MOF of 1mm, with fibre's parameters $r_i = 0.4\mu m$, $\Delta = 1.0\mu m$, and $d_{air}/\Delta = 0.9$; the pumping pulse is centered at 1.550μm with a temporal duration of 100fs, and peak power of 0.1kW (a), 0.4kW (b), 0.7kW (c), and 1kW (d).

increasing the peak power, a flatter and wider supercontinuum is achieved, as expected. For a pump power of 1kW, the supercontinuum extends from ∼500nm to ∼3900nm, and it is formed at a distance of 0.3mm as seen in Fig. 4.22.

This shall be compared with the results of other authors referred in Table 4.2, which shows supercontinuum generation data in different conditions. The main factors of these systems are the waveguide geometry, the materials, and the input pulse characteristics (wavelength, power, and pulse width – as well as pulse shape), which require different fibre length and lead to different SCG bandwidth. The results of our numerical study predict a record distance for the supercontinuum generation, due to a careful adjustment of the fibre properties and laser pumping conditions.

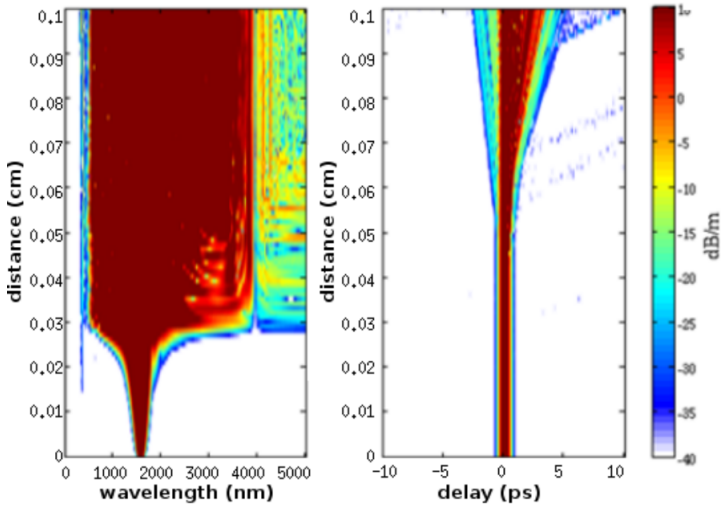

Fig. 4.22: Supercontinuum generation in a highly nonlinear LS-MOF, with the same fibre's parameters as in Fig. 4.20, and pulse temporal duration of 100fs, a peak power of 1kW, and a pumping wavelength of 1.55μm.

#ref.	fibre	pump source	output	
			fibre length [cm]	SCG bandwidth [µm]
P. Domachuk et. al	*HNL PCF: "wagon whell design", with tellurite*	*100fs pulse at 1.550µm, with energy of 1.9nJ*	*0.8*	*~0.790-4.870*
N. Granzow et. al	*step index fibre, with silica&chalcogenide*	*59fs pulse at 1.550µm, with energy of 0.014nJ*	*0.4*	*~0.980-2.000*
J.C. Travers et. al	*HC-PCF, with gas-filled core*	*600fs pulse at 0.400µm, with energy of 10000nJ*	*2.0*	*~1.400-1.000*
W. Gao et. al	*suspended core fibre, with arsenic trisufide*	*200fs pulse at 2.500µm, with peak power of 1.32kW*	*1.3*	*~1.750-3.010*
N. Granzow et. al	*nano-spike waveguide, with arsenic trisulfide*	*65fs pulse at 2.000µm, with energy of 0.018nJ*	*0.2*	*~1.700-3.900*
O. Mouawad et. al	*suspendec core fibre, with arsenic trisulfide*	*200fs pulse at 2.500µm, with energy of 1nJ*	*2.0*	*~0.600-4.100*
S. Xie et. al	*double nanospike waveguide, with arsenic trisulfide*	*60fs pulse at 1.550µm, with energy of 0.038nJ*	*0.1*	*~0.800-2.500*
A. Ermolov et. al	*kagomé HC-PCF, with gas-filled core*	*35fs pulse at 0.800µm, with energy of 5000nJ*	*15.5*	*~0.110-1.000*
A. Barrentos-García et. al	*hexagonal PCF, with silica*	*30fs pulse at 1.550µm, with peak power of 8kW*	*5.0*	*~0.900-2.300*
X. Han et. al	*three hole suspended core fibre, with chacogenide glass core*	*150fs pulse at 3.300µm, with peak power of 750kW*	*15.0*	*~3.000-8.000*
this work - selected case	*layered spiral fibre, with arsenic trisulfide*	*100fs pulse at 1.550µm, with peak power of 1kW*	*0.03*	*~0.500-3.900*

Table 4.2: Supercontinuum generation in highly nonlinear fibres /waveguides – input and output parameters (for references at which more than one case were studied, we have selected the one with the shortest fibre length). refs.: [5, 22, 30, 36, 39, 40, 41, 79, 109, 116]

4.2 Hollow-core microstructured optical fibres

The HC-MOFs include distinct geometries as presented in chapt. 2. In the following subsections we will focus on the hexagonal HC-MOF, and on the kagomé HC-MOF. We will study different light propagation effects in those fibres such as the SCG and UV light generation. We will consider hollow-core fibres filled with gases, and we will see that the nonlinear effects can be enhanced by varying the gas pressure. In addition, we will study the consequences of using a gas pressure gradient in the fibre's core.

4.2.1 HC-fibres properties

In Fig. 4.23 we see a SEM picture of a HC-MOF with a hexagonal lattice, for a fibre composed by strands of silica in the cladding and a hollow core with air, which guides light by means of a 2-dimensional photonic bandgap. This fibre is the model HC-1550-04 from NKT Photonics. The model of this fibre is similar to the first fabricated MOFs, for which it was predicted the photonic bandgap effect similarly to what happens in photonic crystals [93], but its parameters are different. In particular, the fibre of the picture has a hole diameter of 3.9μm and a hole pitch of 4.0μm. Fig. 4.23.b) shows its fundamental propagation mode at 1.55μm.

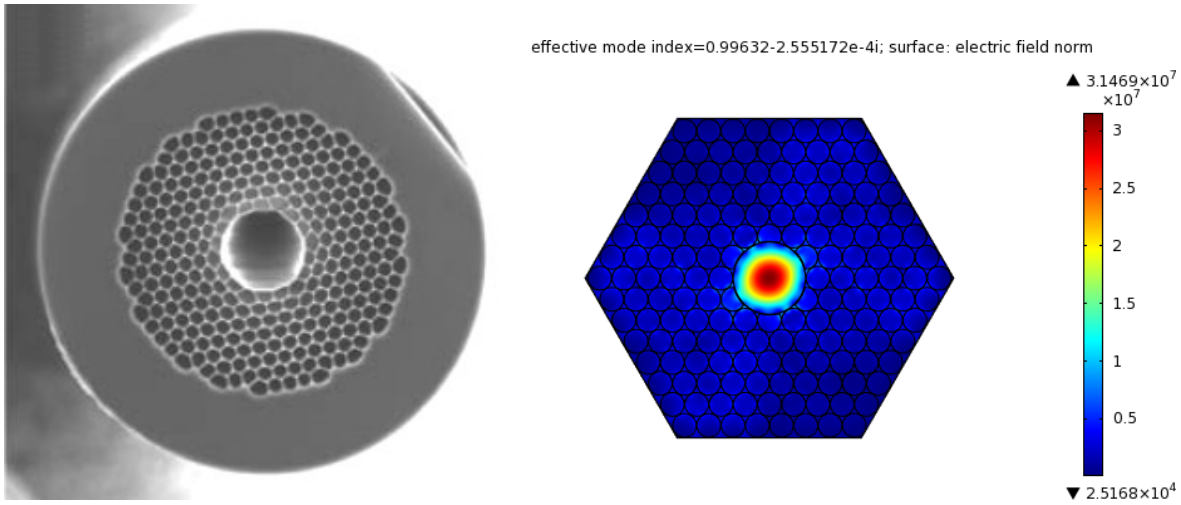

Fig. 4.23: Hexagonal lattice HC-MOF model HC-1550-04 from NKT Photonics: a) scanning electron microscopy (SEM) image; b) fundamental propagation mode at λ=1.55μm for the same HC-MOF, with the dimensions: hole diameter of 3.9μm and pitch of 4.0μm.

In Fig. 4.24 we show the density of states (DOS) of a standard HC-MOF with d/Λ=0.9, obtained with MPB software as explained in chapt. 3. In both these scenarios we vary the

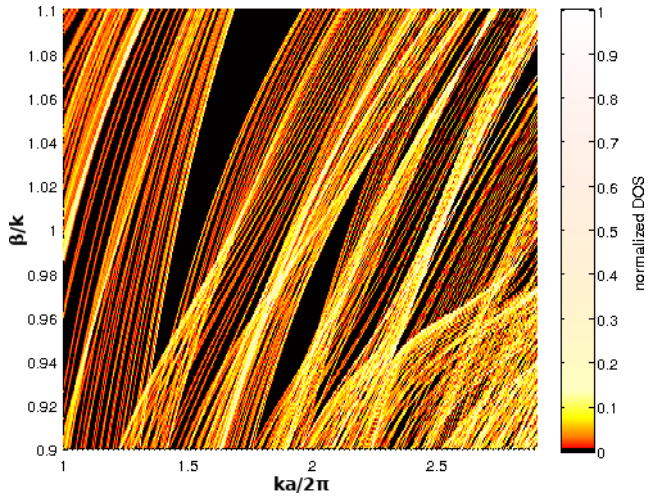

a)

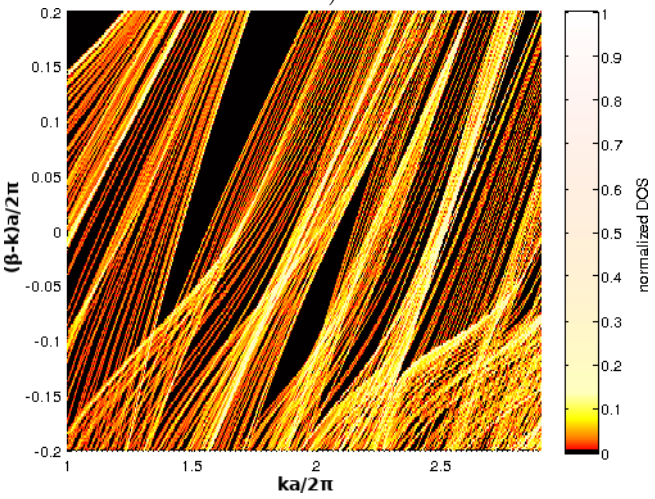

b)

Fig. 4.24: DOS for a hexagonal HC-MOF with d/Λ=0.9, considering a) $\beta/k \approx 1$; b) $\beta - k \approx 0$.

fibre's lattice period parameter, a, in the xx axis, along with the wave number, k. We have done a zoom-in of the properties around the light with β=k, by choosing yy axis around of β/k=1 [as considered in figure 3.4 of ref. [20].], or β-k=0 [as considered in figure 1.a) of ref. [6]]. We can observe bandgaps in those conditions, which in the figure correspond to the black regions, and with $\beta/k < 1$ or $\beta - k < 0$.

We now focus on another important type of fibres: the kagomé HC-MOFs, which were firstly proposed on ref. [7]. In particular, these fibres offer broadband transmission when compared to other HC-MOFs [109], as well as small dispersion, providing an ideal medium for, as example, the generation and guidance of ultraviolet light which is not possible in silica SC-MOFs since the UV light is highly attenuated in silica fibres.

There are two types of kagomé patterns referred in literature [7, 37], as indicated in Fig.

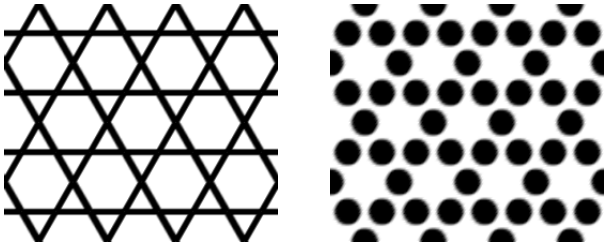

a) b)

Fig. 4.25: The two types of kagomé lattice; by default we are assuming the case in a).

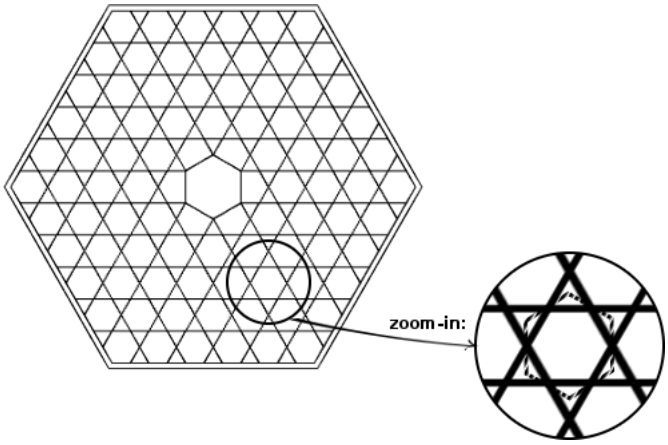

Fig. 4.26: Kagomé HC-MOF geometry – the white regions contain gases, the black regions (i.e. the strands) are made of glass; in the inset region there is a zoom-in of the fibre's details, where the unit cell of the lattice is delimited by a dashed hexagon.

4.25; however, in the context of MOFs, the pattern of 4.25.a) is the standard one.

It is known that the periodicity of the fibre's cladding is what makes possible the guidance in a fibre with hollow-core. Thus, in order to know how the kagomé HC-MOFs guide light, we shall study their lattice. The kagomé HC-MOF geometry is shown in Fig. 4.26, in which we present a zoom-in selection of the fibre's cladding. Inside the zoom-in region, a unit cell is signalled with a dashed hexagon; this is the primitive unit cell of this fibre. The unit cell must be chosen like this since this is the region which, when repeatedly translated, generates the full lattice and has the maximum number of possible symmetry operations (i.e. geometrical operations which maintain the figure with the same aspect).

For studying the bandgaps or the DOS of the kagomé model, we have also used the MPB software. In Fig. 4.27 we show the photonic bands of a kagomé HC-MOF composed by silica in the strands and air in the hollow regions, for $k_z \mathrm{a}/2\pi = k n_{\mathrm{eff}} \times [2/3(d_{core})]/(2\pi)$=8.463 (those arguments include the case of: λ=0.790μm, n_{eff}=1.0028578, and d_{core}=10.0μm). We

gas	a_1	b_1	a_2	b_2
air	14926.44×10^{-8}	19.36×10^{-6}	41807.57×10^{-8}	7.434×10^{-3}
helium	4977.77×10^{-8}	28.54×10^{-6}	1856.94×10^{-8}	7.760×10^{-3}
neon	9154.48×10^{-8}	656.97×10^{-6}	4018.63×10^{-8}	5.728×10^{-3}
argon	20332.29×10^{-8}	206.12×10^{-6}	34458.31×10^{-8}	8.066×10^{-3}
krypton	26102.88×10^{-8}	2.01×10^{-6}	56946.82×10^{-8}	10.043×10^{-3}
xenon	103701.61×10^{-8}	12.75×10^{-3}	31228.61×10^{-8}	0.561×10^{-3}

Table 4.3: Coefficients of the Sellmeier equation for each gas, at pressure p_0 = 1bar, and temperature Θ_0 =273.15K (after ref. [15]).

do not observe a full bandgap above the air line that is a y=8.463, but the density of states is very low in the regions which correspond to the fundamental propagation modes. Thus, we conclude that the guidance in those kagomé fibres is due to the low DOS.

As explained in chapt. 3, the propagation modes can be found by solving Eq. (2.17) numerically, with $n(\lambda, r)$ for the full cross-section of the fibre. For this purpose we have used Comsol multiphysics, and we have found the propagation modes and their characteristics. In Fig. 4.28 we show the fundamental mode of a helium-filled kagomé fibre with the parameters mentioned above, for a pressure of 10bar and a pumping wavelength of 790nm.

Alternatively, in the case of kagomé HC-MOFs, n_{eff} can be theoretically approximated by that of a glass capillary, which is given by [52]:

$$n_{\text{eff}} = n_{\text{gas}} - \frac{1}{2}\left(\frac{u_{01}\lambda}{\pi d_{\text{core}}}\right)^2 \tag{4.9}$$

where d_{core} is the core-diameter, u_{01} is the first zero of the J_0 Bessel function, n_{gas} is the refractive index of the core-filling gas, which is given by a Sellmeier equation including the effects of pressure and temperature variation [15]:

$$n_{\text{gas}} = \sqrt{1 + \frac{p}{p_0}.\frac{\Theta_0}{\Theta}\left[\frac{a_1\lambda^2}{\lambda^2 - b_1} + \frac{a_2\lambda^2}{\lambda^2 - b_2}\right]} \tag{4.10}$$

whose coefficients a_i and b_i were taken from ref. [15](see Table 4.3), p is the pressure at the fibre core, p_0 is the 1bar pressure, Θ_0 =273.15K, and Θ is the absolute temperature of the fibre core.

In gas-filled kagomé HC-MOFs, the ZDW can be shifted to lower wavelengths and enter the UV region. The ZDW of a gas-filled kagomé HC-MOF can be tailored by choosing an

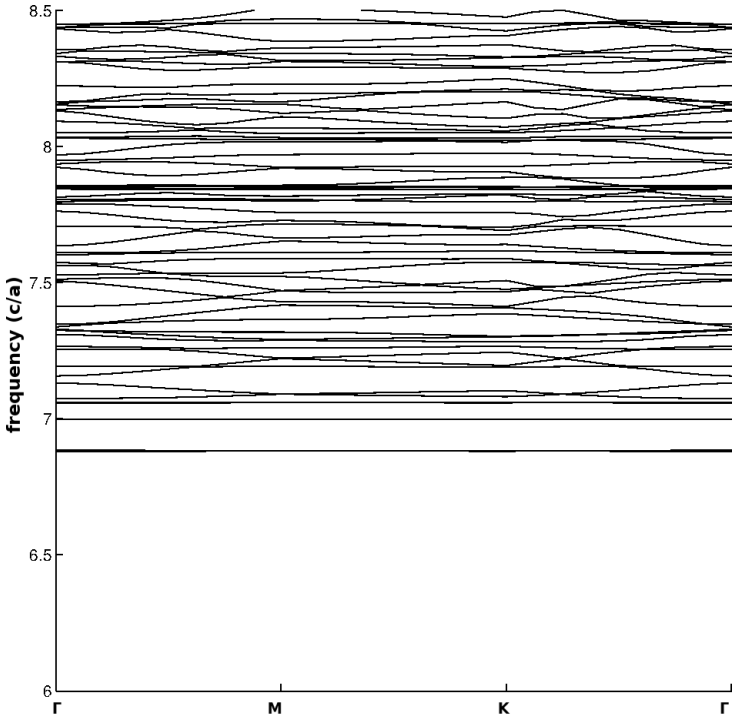

a)

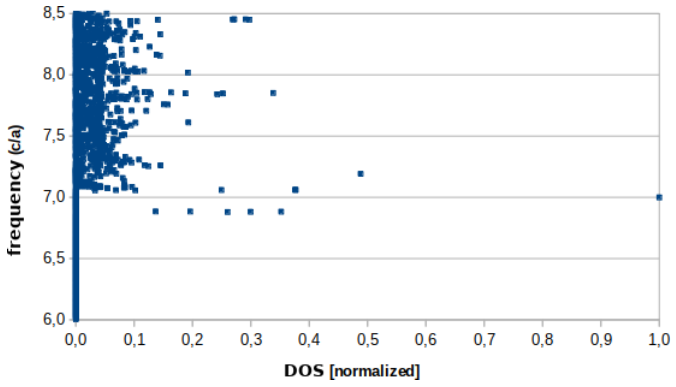

b)

Fig. 4.27: a) The photonic bands diagram; b) the DOS graph, of a kagomé HC-MOF with $k_z a/(2\pi)$=8.463, and thickness/a=1/26.6667.

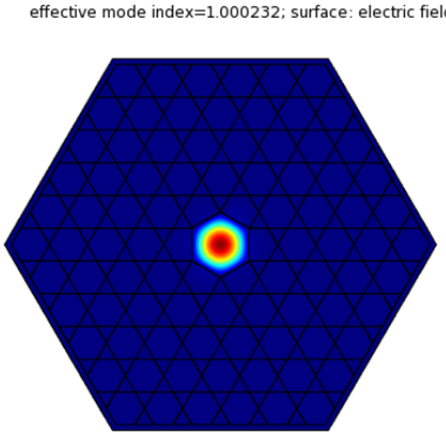

Fig. 4.28: The fundamental propagation mode of a kagomé HC-MOF filled with helium: core diameter $d_{core} = 40.0\mu$m, thickness of the glass strands $t = 0.1\mu$m, and gas pressure p=10.0bar, @$\lambda = 790nm$.

appropriate gas to fill the core and by adjusting its pressure. This effect is illustrated in Fig. 4.29, which shows the dependence of the parameter β_2 on the wavelength for a kagomé HC-MOF with a core diameter of $40.0\mu m$, and thickness of the glass strands of $0.1\mu m$, filled with helium, or argon, obtained from Eq. (4.9), using the relation $\beta_2 = \frac{d^2\beta(\omega)}{d\omega^2} = \frac{d^2\{n_{\text{eff}}k\}}{d\omega^2}$.

In Fig. 4.30 we show the GVD for different filling gases at 1bar, in the same HC-MOF with 40.0μm core diameter. At pumping wavelengths lower than the zero dispersion wavelength (λ_0) the dispersion regime of these fibres is normal, whereas at pumping wavelengths higher than λ_0 the dispersion regime is anomalous [Figs. 4.29, and 4.30]. We see that the group velocity dispersion curves are different for each gas; in particular, they are different in the region of the pumping wavelength (790nm) which will be considered below.

The dependence of ZDW with pressure is plotted in Fig. 4.31, at room temperature. In the case of helium and for pressures up to 150bar, the dispersion regime is always anomalous at $\lambda_{pump} = 790$nm; however, for the other gases the anomalous regime at 790nm only happens for smaller pressures. For the considered noble gases, when the pressure varies from 1 to 150bar, the ZDW varies in the following way: for helium in the range 215.7nm to 659.2nm, for argon in the range 406.2nm to 1355.9nm, for krypton in the range 482.6nm to 1609.5nm, and for xenon in the range 693.2nm to 1973.5nm. We can notice that with HC-fibres a ZDW well below that of SC-fibres made of silica can be achieved.

In order to study the propagation of light in HC-MOFs filled with gases, we must take into account that the Kerr coefficient increases linearly with the gas pressure, according with, $n_K(p) = pn_K^0$ [16], where p is pressure and n_K^0 is the value of the Kerr coefficient at 1 atm.

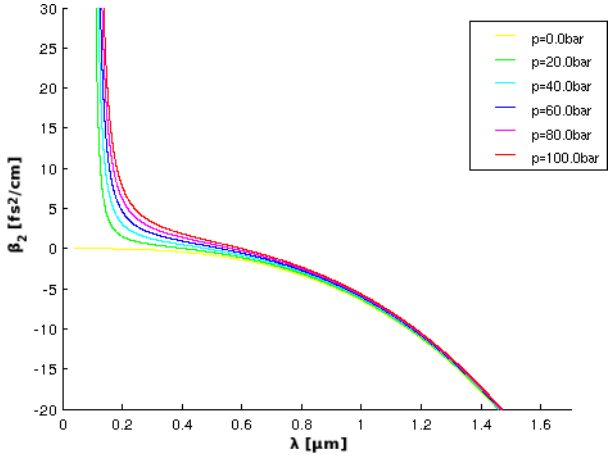

a)

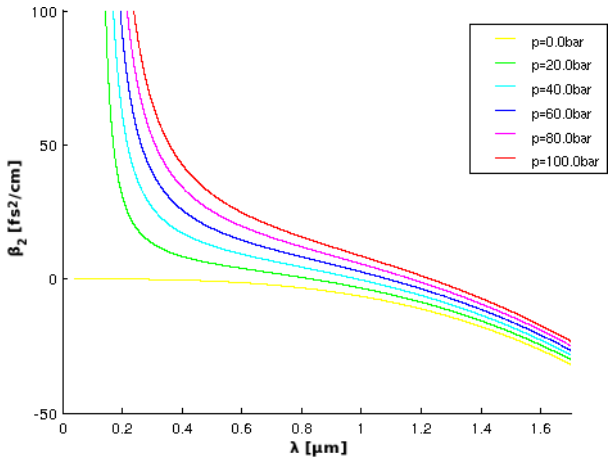

b)

Fig. 4.29: Dispersion curves of a kagomé HC-MOF with a 40μm core diameter filled with a noble gas: a) helium with pressures p={0.0, 20.0, 40.0, 60.0, 80.0, 100.0}bar; b) argon with pressures p={0.0, 20.0, 40.0, 60.0, 80.0, 100.0}bar.

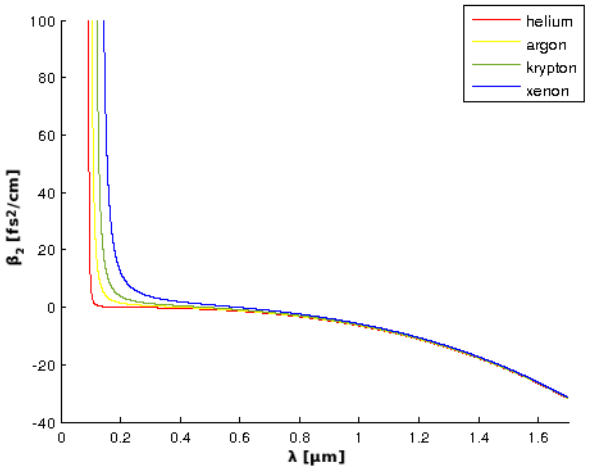

Fig. 4.30: Dispersion curves of a kagomé HC-MOF with a 40μm core diameter filled with distinct noble gases at 1bar.

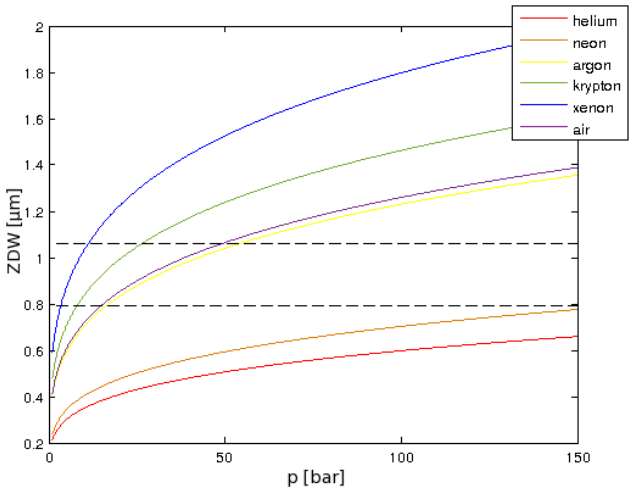

Fig. 4.31: ZDW as a function of the pressure for various gases: helium, neon, argon, krypton, and xenon.

n_{Kerr}x10^{16} [m^2/W]				
helium	neon	argon	krypton	xenon
5.21x10^{-9}	1.31x10^{-8}	1.27x10^{-7}	3.07x10^{-7}	9.16x10^{-7}

Table 4.4: Kerr coefficients for various noble gases at pressure of 1 atm (after ref. [14]).

Table 4.4 shows n_K^0 for different noble gases.

4.2.2 Light propagation in kagomé fibres - SCG

After having characterized the fibre's properties for various filling gases and different pressures, we can simulate the propagation of light pulses in those fibres. For that purpose we will solve Eq. (2.24), but without the Raman effect, since noble gases are Raman-free:

$$\begin{aligned}\frac{\partial u(z,t)}{\partial z} - i\left[\sum_{k>1}\frac{1}{k!}\beta_k i^k \frac{\partial^k}{\partial \tau^k}u(z,t)\right] + \frac{\alpha(\omega)}{2}u(z,t) = \\ = i\gamma\left(1 + i\tau_{shock}\frac{\partial}{\partial t}\right)|u(z,t)|^2 u(z,t),\end{aligned} \tag{4.11}$$

In Figs. 4.32-4.33 we show the pulse propagation in a kagomé fibre, in the presence or in the absence of quantum noise using a 600fs FWHM pulse with an energy of 10μJ at 800nm [P_0=14.667MW]. The considered fibre is a kagomé HC-MOF with a 30μm diameter core filled with 25bar of argon (ZDW at 750nm). The dispersion was computed as mentioned above with Eq. (4.9), assuming the referred d_{core}. We notice a clear difference between the cases without and with quantum noise: in the case with quantum noise the pulse spreads faster, and it has more variations such that it does not present the same symmetry as in the other case.

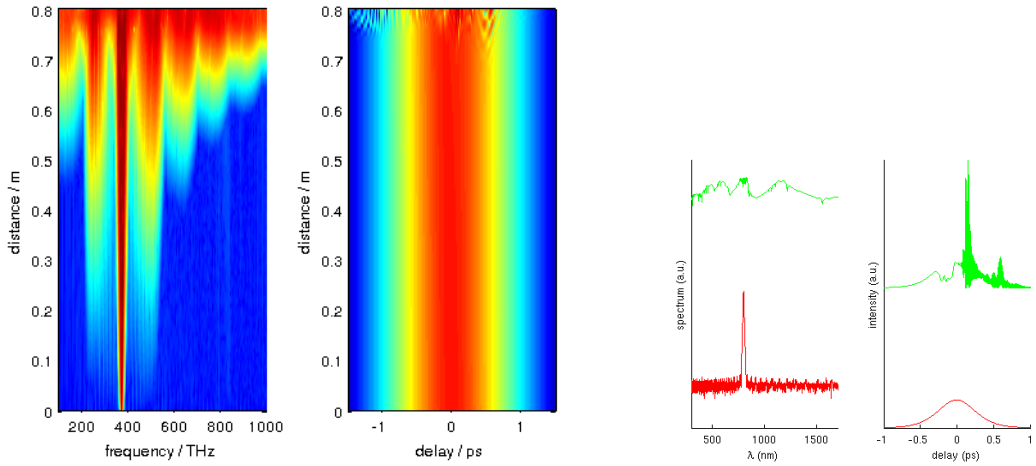

a) b)

Fig. 4.32: a) Spectral and temporal evolution of a pulse propagation in a kagomé HC-MOF without inclusion of quantum noise; b) input and output pulses.

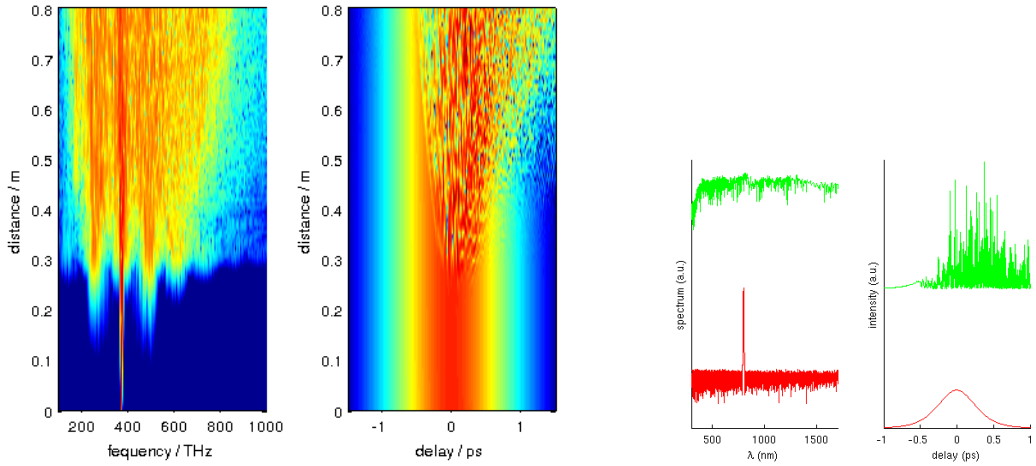

a) b)

Fig. 4.33: a) Spectral and temporal evolution of a pulse propagation in a kagomé HC-MOF with inclusion of quantum noise; b) input and output pulses.

4.2.3 Light propagation in kagomé fibres - UV light generation

A pulse propagating in the anomalous dispersion regime possessing enough energy to be a higher order soliton undergoes through an initial narrowing (see chapt. 2). This solitonic compression is limited by perturbation effects such as higher order dispersion or intrapulse Raman scattering. This limitation is less significant in kagomé fibres filled with noble gases, because they have small dispersion and they do not present Raman response. Therefore, considerable compression can be achieved, as shown in Fig. 4.34.

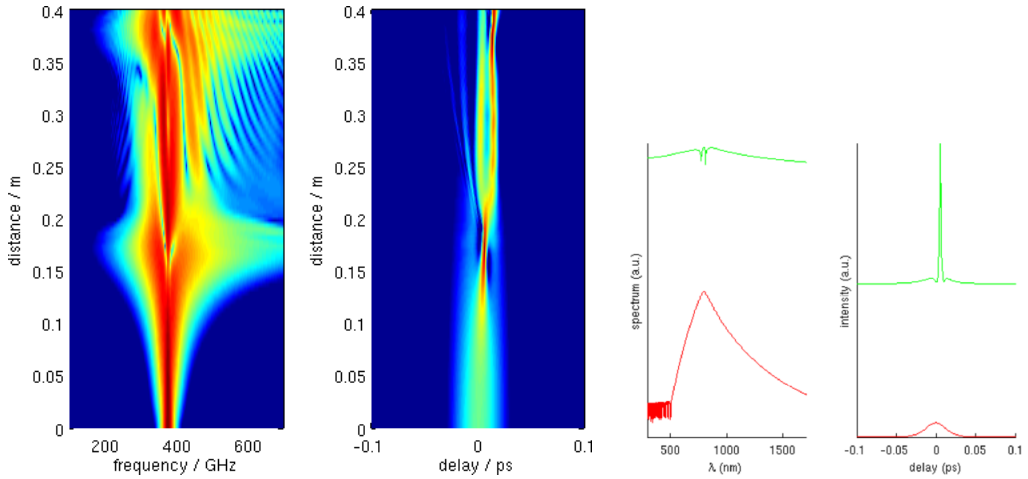

a) b)

Fig. 4.34: (a) Spectral and temporal evolution of a 30fs input pulse at 800nm through a kagomé MOF with a 30μm diameter core filled with argon; (b) initial (red) and compressed (green) pulse profiles in spectral and time domains.

When the soliton compression is high enough, the broadened spectrum may overlap with resonant dispersive-wave frequencies, which are consequently excited in the UV region. After this initial compression, the pulse splits in the time domain, which may generate a supercontinuum or UV light. The UV light is generated approximately when the pulse achieves the maximum temporal compression right before the soliton fission.

The phase-matching condition in the case of maximum pulse compression is given by:

$$\beta(\omega) - \beta_c - \beta_1[\omega - \omega_s] = \gamma P_c/2, \tag{4.12}$$

where P_c is the power of the compressed pulse given by $P_c \approx f_{opt} P_0$. The optimum pulse compression factor, f_{opt}, can be estimated by the following empirical relation [109]:

$$f_{opt} \approx 4.6 n_{order}, \tag{4.13}$$

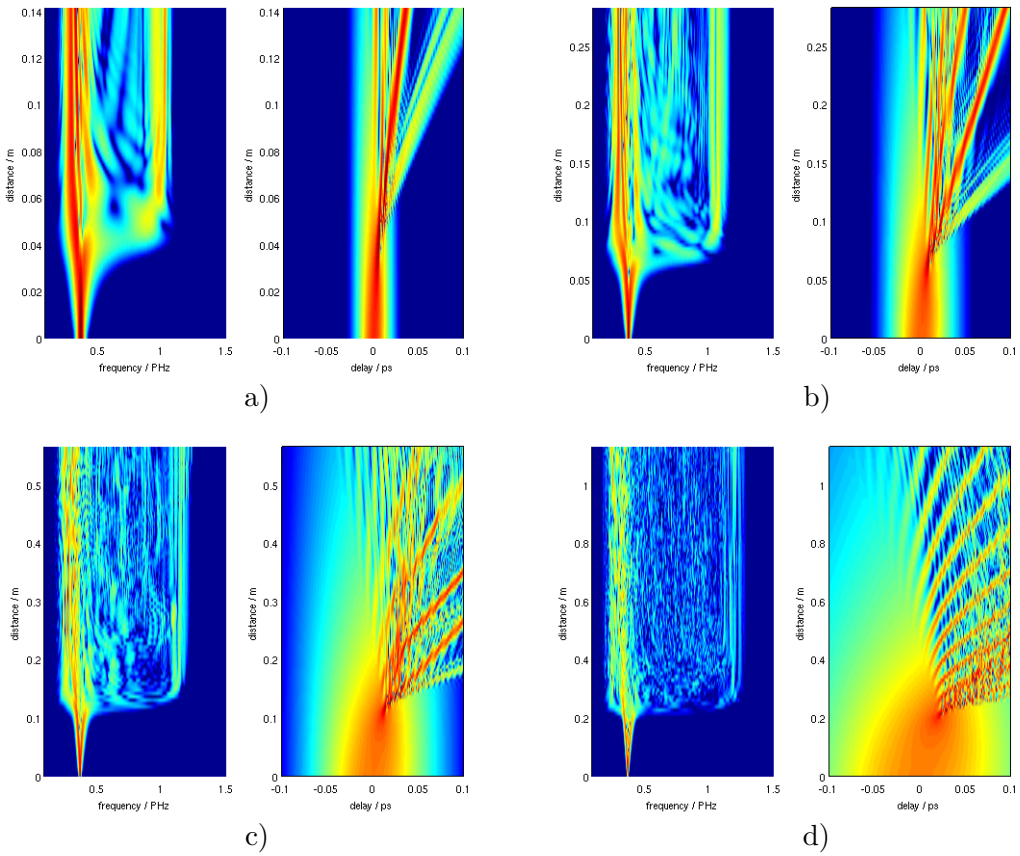

Fig. 4.35: Spectral and temporal pulse propagation in a kagomé fibre of 30μm core diameter filled with 9.8bar of argon, with λ_{pump}=600nm; a)-d): dependence of UV light generation on pulse duration (15, 30, 60, and 120fs).

where n_{order} is the soliton order.

The output spectra may vary from a UV light output (for smaller pulse widths) to a SCG output (for larger pulse widths), which can be observed in Fig. 4.35.

In Figs. 4.36 & 4.37, 4.38, and 4.39 we show the spectral evolutions of pulses propagating in the kagomé HC-MOF filled with argon, xenon, and helium, respectively, at different pressures. The kagomé HC-MOF considered in those cases as d_{core} = 40.0μm and thickness=0.1μm.

We show the results for light propagation in argon filled kagomé fibres with two different pumping wavelengths: at 1060nm (Fig. 4.36) and at 790nm (Fig. 4.37). In Fig. 4.36.a)-b) we are pumping at the anomalous dispersion regime, in Fig. 4.36.c) we are pumping in the ZDW, and in Fig. 4.36.d) we are pumping in the normal dispersion regime. The ZDWs location are shown in Fig. 4.31, where the dashed lines represent the pumping cases at 790nm or 1060nm, for comparison purposes. When the pressure is increased the nonlinearity also increases, such that we observe the occurrence of the spectral broadening in shorter distances

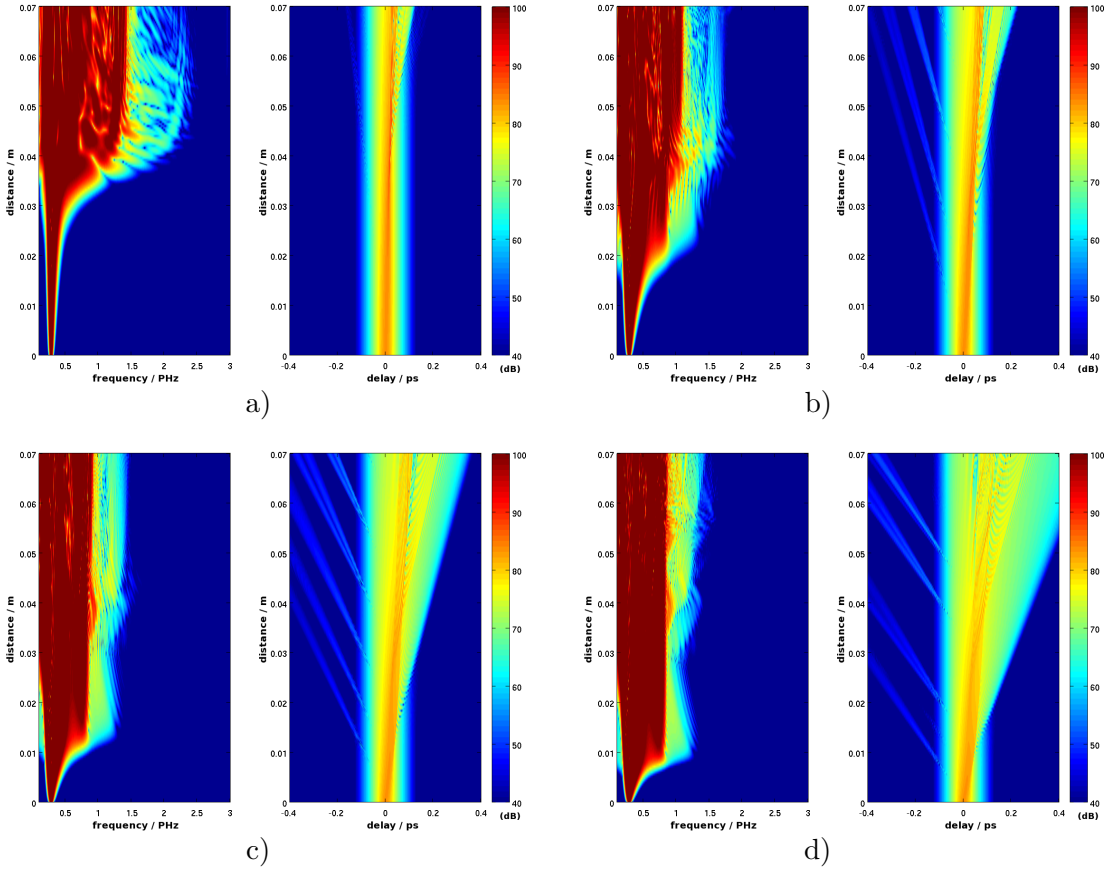

Fig. 4.36: Spectral and temporal evolutions for a pumping wavelength of 1.06μm, with pulses of t_{FWHM}=40fs, energy of 10μJ, and p={10, 30, p_0, and 80}bar, where p_0=54.1 is the pressure of argon for which the ZDW is at 1.06μm; the core diameter of the considered kagomé fibre is 40μm.

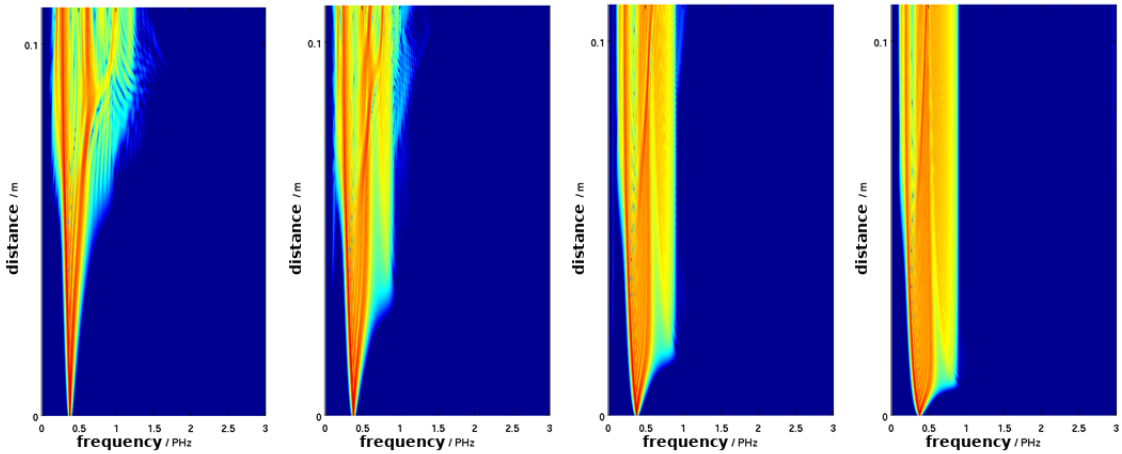

Fig. 4.37: a)-d) Spectral evolution of an input pulse of t_{FWHM}=40fs, energy of 10μJ, λ=790nm, along a kagomé HC-MOF filled with argon at pressure a) 10bar, b) 20bar, c) 40bar, d) 80bar; d_{core}=40.0μm.

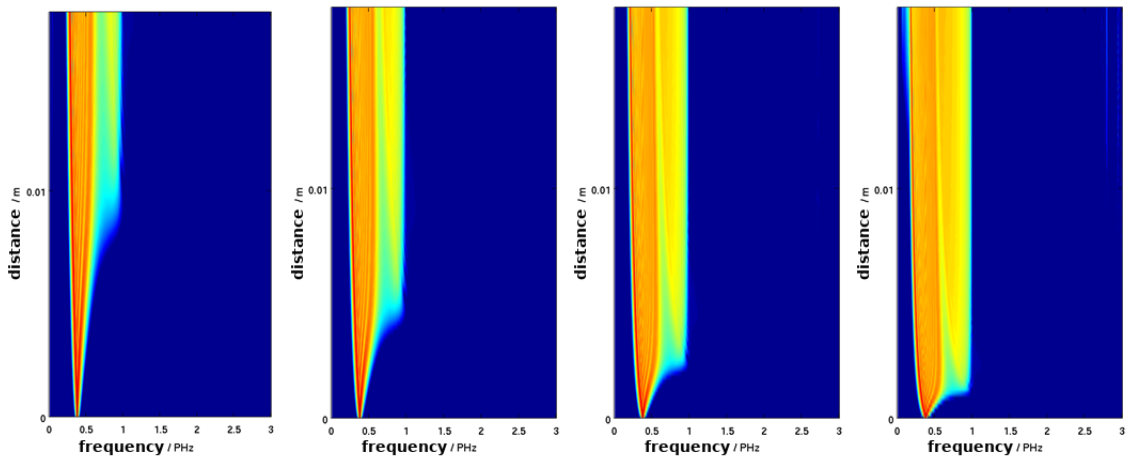

a) b) c) d)

Fig. 4.38: a)-d) Spectral evolution of an input pulse of t_{FWHM}=40fs, energy of 10μJ, λ=790nm, along a kagomé HC-MOF filled with xenon at pressure a) 10bar, b) 20bar, c) 40bar, d) 80bar; d_{core}=40.0μm.

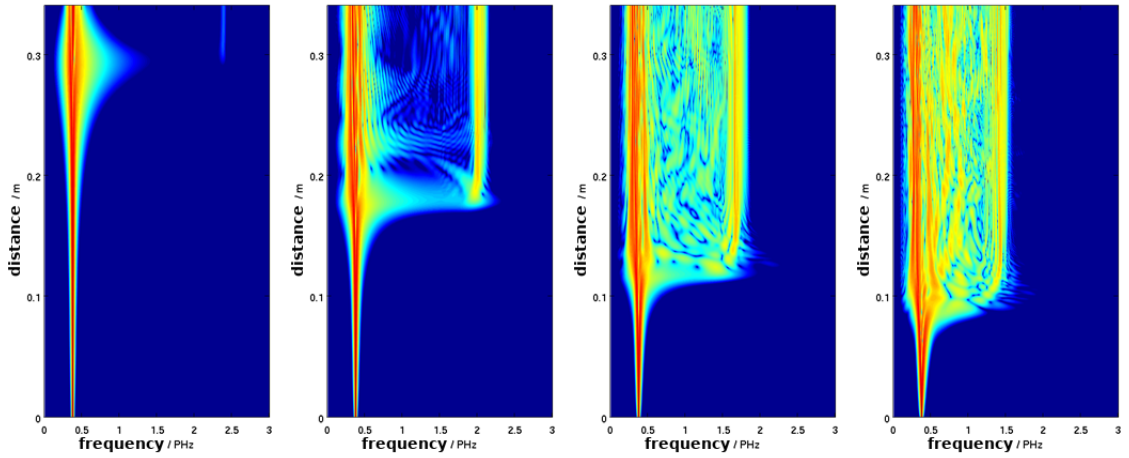

a) b) c) d)

Fig. 4.39: a)-d) Spectral evolution of an input pulse of t_{FWHM}=40fs, energy of 10μJ, λ=790nm, along a kagomé HC-MOF filled with helium at pressure a) 10bar, b) 20bar, c) 40bar, d) 80bar; d_{core}=40.0μm.

for higher pressures. We observe a broader expansion when the pumping is at anomalous dispersion regime, followed by the case of pumping at the ZDW, and at last for the normal pumping regime. This is due to the increased difference between the pump wavelength and the ZDW, which inhibits phase matching conditions.

In the case of xenon (Fig. 4.38), the final spectral broadening is similar for all the considered pressures and the distance at which this happens decreases for higher pressures. Nevertheless, the distance for spectral broadening in the xenon filled fibre is one order of magnitude smaller than the same distance for an argon filled fibre, due to the fact that the xenon presents higher nonlinearity than argon. For instance, for xenon at a pressure of 150bar, the n_K is $1.37 \times 10^{-20}\mathrm{m}^2/\mathrm{W}$, which is similar to that of silica (which is $2.6 \times 10^{-20}\mathrm{m}^2/\mathrm{W}$).

In the case of helium (Fig. 4.39), the pumping is always in the anomalous dispersion regime. Note that as we increase the pressure, we change nonlinearity and dispersion, in such a way that we are getting closer to the ZDW, so that the soliton order for Fig. 4.39.a)-d) are 4.9, 7.0, 10.3 and 15.8. As a consequence, the fission length is decreasing with pressure.

The expression of phase matching condition on Eq. (4.12) gives $\omega \approx \{2.4, 2.0, 1.7, 1.6\}$PHz for Figs. 4.39.a)-d) which agrees reasonably with the peak of the generated UV band. In the case presented in Fig. 4.37.a) the pumping is made in the anomalous dispersion regime and the soliton order is 38.4. The corresponding fission length is 11.0 cm, and Eq. (4.12) for the phase-matching gives in this case $\omega \approx 0.9$PHz, which corresponds to the new band seen in that figure.

For distinct gas pressures the UV peak is located at a different frequency, as shown in Fig. 4.40, and in agreement with the prediction by Eq. (4.12), where the terms of β_i depend on the pressure. In Fig. 4.41 we observe the frequency of the UV peak versus the pressure of the gas inside the fiber's core.

In Figs. 4.42.a)-d) we show the X-FROG trace of the input and output pulses. We have computed the correlation between the input pulse and itself, and the correlation between the input pulse and the output pulses, for the same 3 cases considered in 4.37.a), 4.38.a) and 4.39.a). Fig. 4.42.a) shows the trace of an unchirped pulse, as was expected for the input pulse. In the figures for the output X-FROGs, the trace varies for different fibres or different pumping conditions: in the figure of X-FROG for argon we see new frequencies with significant amplitudes, where we can observe two different peaks, which is in agreement with the two peaks observed in Fig. 4.37.a); in the figure of X-FROG for xenon we observe a generation of a wide range of new frequencies, in agreement to Fig. 4.38.a); moreover, in the

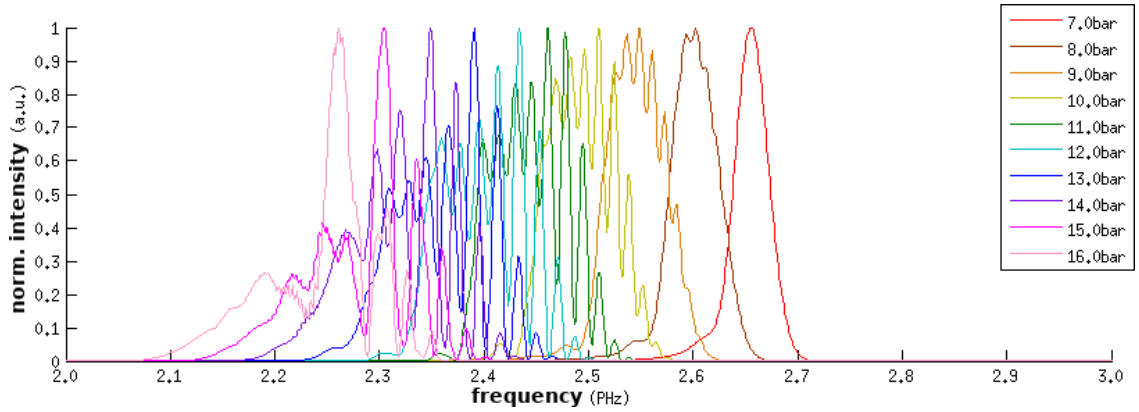

Fig. 4.40: Output spectrum of UV light generation in a kagomé HC-MOF with d=40.0μm, thickness=0.1μm, filled with helium; the laser signal has λ_{pump}=800nm, FWHM of 40fs, and energy=20μJ; the pressure of the core-filling gas is indicated in the label.

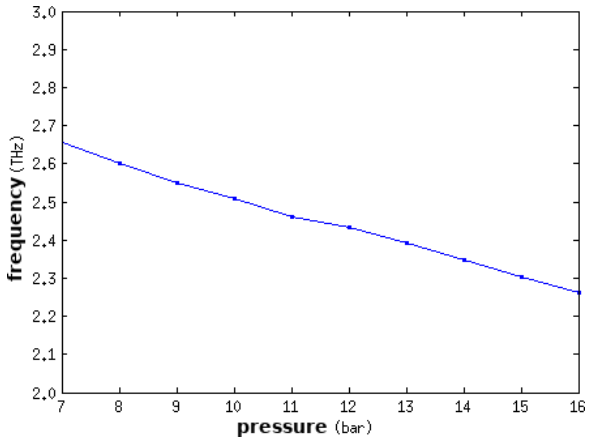

Fig. 4.41: Frequency with maximum intensity in the UV region for different gas pressures, computed accordingly to the results of Fig. 4.40 [which has the same parameters for the fibre and input pulse].

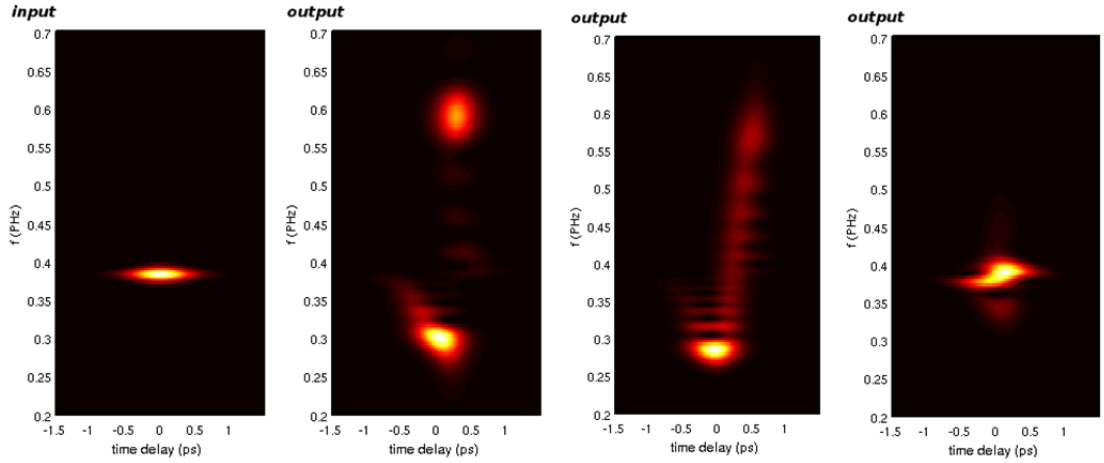

Fig. 4.42: a) X-FROG trace for an input pulse signal of FWHM=0.040ps, 10μJ, λ=790nm; X-FROG trace for the output signal after different lengths of the kagomé fibre filled with 10 bar of different gases: b) filled with argon and l=0.0693m; c) filled with xenon and l=0.0179m; d) filled with helium and l=0.3403m, where l is the fibre length.

figure of X-FROG for helium we observe the trace of the self-phase modulation, by comparison with ref. [110]. These figures of X-FROG are in agreement to the light propagation results seen in 4.37.a), 4.38.a), and 4.39.a) respectively.

In order to characterize the output of UV light we used the conversion efficiency and the quality factor [109]. The efficiency of the UV light generation is defined as the fraction of the total output spectral power at UV wavelengths (i.e. for wavelengths from 10 nm to 350 nm), P_{UV}, and the total input power, P_0:

$$\text{efficiency} = P_{UV}/P_0. \tag{4.14}$$

In addition, in order to measure the quality of the UV emission, we used the factor:

$$q_{UV} = P_{UV}^{FWHM}/P_{UV}, \tag{4.15}$$

where P_{UV}^{FWHM} is the spectral power within the FWHM of the strongest UV peak, and P_{UV} is the total spectral power in the UV region. In figures 4.43.a)-b) we see how the efficiency and the quality factor vary for gas-filled kagomé fibres as considered in Figs. 4.37, 4.38, and 4.39. We see that the efficiency increases with pressure, which is due to the fact that a higher pressure corresponds to higher nonlinear effects and consequentially to higher transfer rates of energy into the UV region. In addition, the quality factor of the UV light increases for relatively medium pressure values (up to approx. 10bar); however, for higher pressures the

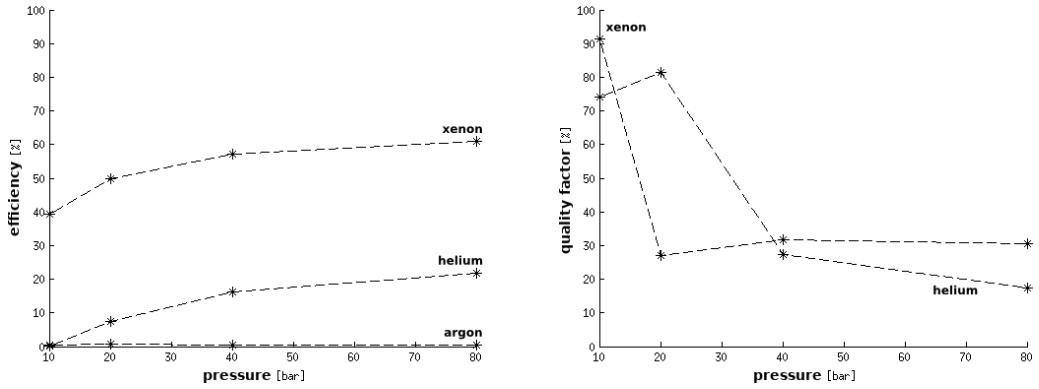

a) b)

Fig. 4.43: a) Efficiency of UV light generation calculated for different pressures of the core-filling gas, with the fibre and input pulses of Figs. 4.37, 4.38, and 4.39; b) quality factor calculated.

UV band spreads and resembles that of supercontinuum generation. Therefore, in order to achieve both an efficient and a high quality UV generation, we benefit from choosing the pressure, but it shall not be too high neither too low, in order to have both an efficient generation and a high quality factor.

In order to tune the generated UV spectrum, several adjustments of the input pulse have been made: energy, width, and center wavelength, as well as the pressure of the gas, maintaining the same kagomé HC-MOF with $d_{core} = 40.0\mu$m and thickness=0.1μm.

Fig. 4.44.a)-b) shows an optimized result that was obtained by changing those parameters and that corresponds to a gas pressure of p=10bar, centre wavelength λ_{pump}=800nm, pulse full width at half maximum (FWHM) of 40fs, and energy=20μJ. The UV output shown in this figure has a quality factor of 85.9%, and the process has a conversion efficiency of 5.2%.

The output spectra that results from the propagation of ultrashort pulses is usually highly coherent, which is important for several applications. In the Fig. 4.44.c) the 1st order coherence was calculated to study the fluctuations in the system due to random noise, with Eq. (3.9). This figure shows that the generated spectrum has a very high coherence, for the case considered in Fig. 4.44.a)-b). It is seen that the coherence is very high along a large range of frequencies from the initial pulse frequency up to the UV region. Light pulses with such coherence may be useful if the final light is used as a source of phase correlated pulses.

It is possible to experimentally realize a gradient of pressure in the gas that fills the fibre core [71]. When the pressures at the input and output of the fibre are different, the pressure profile in equilibrium is given by the following equation [71]:

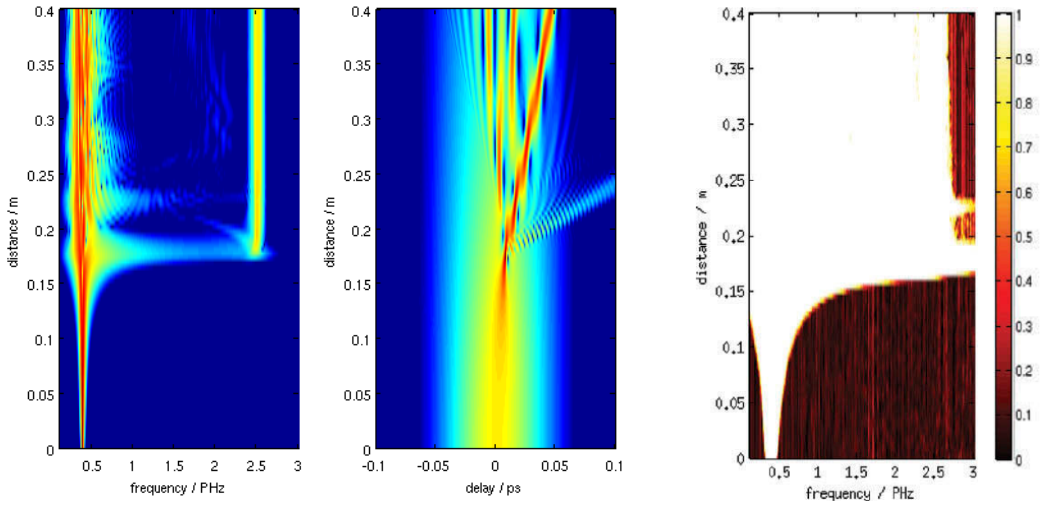

a) b) c)

Fig. 4.44: Spectral (left), temporal (middle) and coherence (right) evolution of ultrafast non-linear UV generation in a kagomé HC-MOF, with the same fibre and pulse parameters as in Fig. 4.40, considering a core filled by helium gas with a pressure of p=10bar.

$$p(z) = \sqrt{p_i^2 + \frac{z}{l}\left(p_f^2 - p_i^2\right)}, \tag{4.16}$$

where $p(z)$ is the pressure at a distance z, p_i is the initial pressure, p_f is the final pressure, and l is the fibre length.

In Figs. 4.45-4.46, the results of simulations with a pressure gradient following Eq. (4.16) are seen. It can be observed that the distance for maximum compression is different in the two considered cases of a positive gradient and of a negative gradient. In addition, it can be observed that the new UV frequencies appear in different regions, which is due to the different properties depending on the fibre's gas filling pressure gradient. The fission length is higher for a positive gradient than for a negative gradient. This is due to the fact that for the initial higher pressures the nonlinearity at the start zone is higher such that the nonlinear effects occur at shorter fibre lengths.

In the case of the positive gradient, a quality factor of 42.9% and an efficiency of 8.7% were found, whereas in the case of the negative gradient, a quality factor of 81.5% and an efficiency of 6.0% were found. Fig. 4.46 shows that both scenarios of pressure gradient considered here for achieving UV light have a very high coherence throughout a very broad range of frequencies.

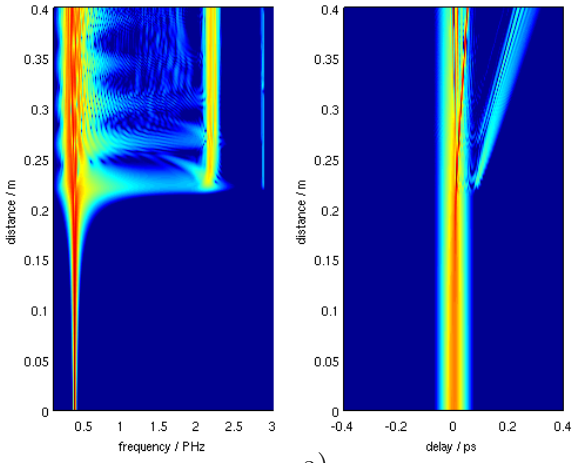

a)

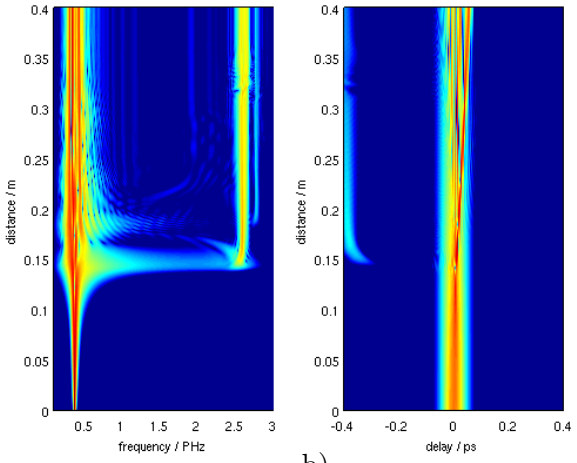

b)

Fig. 4.45: Spectral and temporal evolution of non-linear UV generation in a kagomé MOF with a pressure gradient of: (a) 1bar to 15bar, and (b) 15bar to 1bar; the other parameters are the same as in Fig. 4.44.

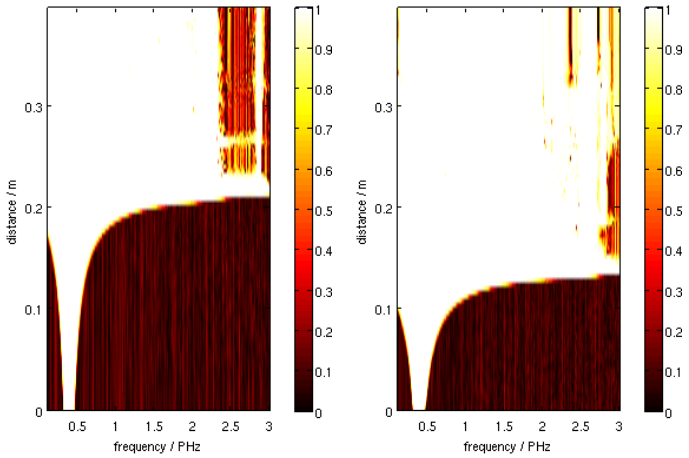

Fig. 4.46: Coherence evolution for the same two scenarios considered in Fig. 4.45, respectively.

4.3 Summary

In the first part of this chapter, we have seen that by changing the SC-MOFs design it is possible to change their dispersive and nonlinear characteristics.

In order to study the supercontinuum occurring in fibres, it is possible to numerically isolate some of the involved effects by eliminating some of the terms in the equations. With this approach we study the real system described by the full equation, as well as hypothetical systems with only some of the effects.

We have shown that the LS-MOF is a model that unites high nonlinearity and adjustable dispersion. We have studied the LS-MOF composed by air and silica, and by air and arsenic trisulfide glass. For a LS-MOF with AFF=90.0% composed by silica and air, we have achieved a nonlinear parameter of 70.0W^{-1} km^{-1}, with zero dispersion, simultaneously, at the telecom wavelength of 1.55μm.

We have found that for enhancing the supercontinuum effect, we shall work with a pumping wavelength on the anomalous dispersion region, or close to a ZDW at the normal dispersion region. The results of our numerical study for a LS-MOF composed by arsenic trisulfide and air predict a record distance for the supercontinuum generation in a fibre composed by arsenic trisulfide and air: 0.3mm, whose spectral band goes through ∼0.500-3.900μm.

In the second part, we have studied the hexagonal and kagomé HC-MOFs. The latter was considered to be filled with noble gases.

With the HC-MOFs we can achieve ZDWs for lower wavelengths than that achivable with

SC-MOFs.

We have shown the DOS graphs of a hexagonal HC-MOF, and the main fundamental propagation mode.

After that, we have focused on the kagomé fibre, which is a HC-MOF that offer broadband transmission, and small dispersion. We have studied the periodic lattice of the kagomé pattern, and we have presented the photonic bands for a particular instance, concluding that the light guidance in the kagomé fibres studied here is due to low DOS, since their DOS is not null but very low. We have studied the effect of varying the pressure, and the core-filling gas in a kagomé fibre. We have analysed the impact on dispersion by varying those conditions; namely change the dispersion profile leads to different location of the ZDWs. In addition, we have found propagation modes in those fibres. After characterizing the properties of kagomé fibres we have simulated the propagation of light in them. We have analysed the differences on the final spectrum of propagation in HC-MOFs filled with helium, argon, and xenon, at different pressures. The input and output FROG traces, which show a different perspective on the light propagation results, were computed. The first order coherence was also computed.

We have studied the inclusion of a pressure gradient in the gas filling the fibre's core, and we have tuned the UV light by comparing several situations. The efficiency and the quality of the UV light generation was calculated, from which we have found some cases particularly well suited for fabricating UV light sources.

5 EIT - THEORY AND COMPUTATIONAL RESULTS

When the light travels it may find a medium such as a lense, or a glass that transmit light, or a mirror that reflects light, or an opaque medium which absorbs light. The electromagnetically induced transparency (EIT) is a new phenomena which occurs when the presence of a control field converts an initially opaque medium for a probe field at certain frequencies into a transparent one. The transmission of the material can reach 100%. In fact, both the control field and the probe field must be very well tunned each one to a specific transition of the atoms or molecules of the media. The EIT phenomenon is a source of many nonlinear effects, such as enhanced cross phase modulation. In addition, the induced small window of transparency has distinct properties with unusual profiles, such as very low group velocities [57].

In this chapter, we will study EIT in a fibre whose core is filled with an active material such as rubidium. We will compare the propagation properties of the probe without and with the guiding effect of a HC-MOF. In particular, we assume that the power of the control laser has a transverse Gaussian shape, therefore the refractive index of the fibre core that is filled with rubidium varies with the radial position. We will study the consequences of the guiding in this context.

5.1 EIT - an introduction

In an atom, with the states coupled via several transition possibilities, it is possible to observe interference that can result in an enhancement of the transition probability (constructive interference) or a cancellation of the transition probability (destructive interference)

[72]. In 3-level atomic systems, coupled to two laser fields, the interference effects that result in the cancellation of the absorption of light at a resonant frequency lead to the so-called EIT phenomenon. This means that an initially highly opaque medium becomes transparent. In addition, the refractive index of the medium in this range of frequencies becomes very different from before.

EIT experiments have been performed both employing pulsed lasers or continuous-wave lasers. The first observations of the EIT effect were made in strontium atoms [10] and lead atoms [32]. The EIT effect can be observed in optical cavities [18], or in more sophisticated media such as microstructured optical fibres [17].

There has been considerable research efforts regarding the topic of EIT since 1990 [34, 43, 44]. This phenomenon has several potential applications such as in ultraslow light [45], stored light [87], enhancement of nonlinear optical effects [72], lossless propagation of laser beams through optically thick media [72], and quantum information processing [69].

With the EIT phenomena it is possible to trap photons in a medium [69]. It is possible to observe slow-light or fast-light, in those media. In addition, operating in the single-photon level may be possible with EIT in photonic crystals [102].

As was mentioned above, the EIT effect allows not only to suppress light absorption, but also to significantly enhance the nonlinear effects. In fact, EIT materials are the most nonlinear materials found up to date [102].

In this chapter, we will consider a 3-level atomic system, i.e. a system in which only 3 energy levels are relevant to the process, when considering the interaction between the atoms and the electromagnetic fields. Here, we will use the density matrix formalism, but other approaches can be used [72].

It is found that the system macroscopic optical properties depend upon some parameters that are controllable in the experiment, such as the detuning of each laser, and the intensity of the control laser. The EIT phenomenon also depends strongly on the atomic properties of the medium.

In practice, some of the materials in which we can observe the EIT effect are strontium [10, 43], rubidium [38], acetylene [115], and cesium [114].

5.2 The density matrix formalism for nonlinear optics

In order to study the interaction of light and matter, one important method is to use the density matrix formalism [100, chapt. 2]. In such approach, the microscopic properties of the system are studied using a quantum mechanical description, in order to determine the macroscopic properties of the system.

Here, we describe the atomic system quantically, whereas the electromagnetic field is treated by a classical formalism; thus, following a semi-classical approach. In other studies, fully quantum treatments for EIT have also been developed [58, 104].

Let us consider a set of states $|\varphi_i\rangle$ that is a complete set of basis states; then, the density matrix operator ρ is defined as the ensemble average over the product of ket and bra vectors of the system:

$$\rho = \overline{|\varphi\rangle \langle\varphi|} = \sum_j p_j |\varphi_j\rangle \langle\varphi_j| , \tag{5.1}$$

where p_j is the probability of each state j.

We know by quantum mechanics that the average of an observable associated with the operator $\hat{f}$ is given by:

$$\hat{f} = \overline{\langle\varphi| \hat{f} |\varphi\rangle} \equiv \mathrm{Tr}(\rho\hat{f}), \tag{5.2}$$

where Tr denotes the trace.

From the definition of ρ, in Eq. (5.1), and from the Schrödinger equation for $|\varphi\rangle$, we obtain the Liouville equation [90], which is an alternative formula for studying the quantum properties of the system:

$$\dot{\rho} = \frac{i}{\hbar}[\rho, H], \tag{5.3}$$

where the dot mean the time derivative, and H is the full Hamiltonian of the system.

The Hamiltonian here is composed by three parts [100]:

$$H = H_0 + H_{int} + H_{random}, \tag{5.4}$$

where H_0 is the Hamiltonian of the unperturbed system, H_{int} is the interaction Hamiltonian between the system and the propagating light fields, and H_{random} is the Hamiltonian that describes a random perturbation of the system due to thermal motion.

We can, therefore, express the Liouville equation as:

$$\dot{\rho} = \frac{i}{\hbar}[\rho, H_0 + H_{int}] + \dot{\rho}_{relax}, \tag{5.5}$$

with:

$$\dot{\rho}_{relax} = \frac{i}{\hbar}[\rho, H_{random}], \tag{5.6}$$

We can separate the matrix elements ρ_{ij} into two groups: the diagonal matrix elements $\rho_{ii} = \langle i| \rho |i\rangle$ represent the population of the atomic system in the state $|i\rangle$; and the off-diagonal matrix elements ρ_{ij} are called the "coherences"of the system.

The relaxation time evolution of the off-diagonal elements can be expressed as [100, chapt. 2]:

$$(\dot{\rho}_{ij})_{relax} = -\gamma_{ij}\rho_{ij}. \tag{5.7}$$

which corresponds to a linear approximation of the ρ_{ij} variation on time, with $\gamma_{ij}^{-1} = \gamma_{ji}^{-1}$, being a relaxation time between the states $|i\rangle$ and $|j\rangle$, for $i \neq j$. The relaxation time of the population matrix elements, i.e. the diagonal elements, is known as the longitudinal relaxation time, whereas the relaxation time of the off-diagonal matrix elements is known as the transverse relaxation time [100].

It shall be noted that each γ_{ij} is a parameter that can depend not only on the intrinsic properties of the atomic levels but also on other experimental parameters such as the temperature, the density of atoms in the medium, etc. Usually, γ_{ij} is determined by fitting the experimental data to the model.

Eq. (5.5) may be solved with the assumption of a steady-state system, i.e., that all the derivatives of the density matrix elements vanishes to zero. With the additional assumption of having the power of the pump laser much greater than the power of the probe laser, an analytic solution can be found.

The real and imaginary parts of the susceptibility may be derived from the coherences and are responsible for the dispersion effects, and for the absorption /transmission effects, respectively.

5.3 Theory of 3-level systems

The possible combinations for the 3-levels relationship when two transitions are possible and one transition is forbidden are: the Λ-type configuration, the ladder-type configuration,

and the V-type configuration.

5.3.1 Lambda systems

We will consider an atom with 3 levels of energy in the lambda configuration [90] (usually denoted by Λ), as shown in Fig. 5.1, where ω_{pr} and ω_{pu} are the probe and pump laser frequencies, and δ_{pr} and δ_{pu} are the detunings of the lasers with the corresponding levels. We assume that the light of these lasers is monochromatic.

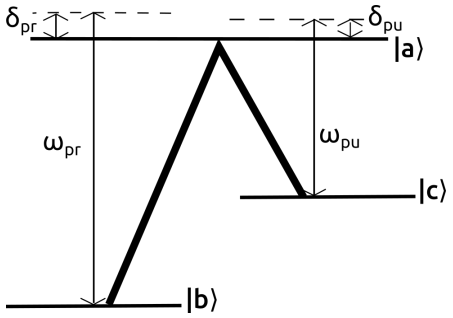

Fig. 5.1: The energy levels of a Λ-type configuration.

The interacting Hamiltonian consists of two different potential energies: the potential energy of the interaction of the probe laser field with the atom and of the pump laser field with the atom:

$$H_{int} = V_{pr} + V_{pu}. \tag{5.8}$$

Assuming that the interactions atom-laser are written in the dipolar approximation:

$$V_{pr} = -\vec{d}_{pr}.\vec{E}_{pr} = -\vec{d}_{pr}.\vec{E}_{pr_0}\cos(\omega_{pr}t) \tag{5.9}$$

$$V_{pu} = -\vec{d}_{pu}.\vec{E}_{pu} = -\vec{d}_{pu}.\vec{E}_{pu_0}\cos(\omega_{pu}t) \tag{5.10}$$

where $\vec{d} = -e\vec{r}_e$ is the dipolar moment of the electron at $\vec{r}_e$ displacement relatively to the nucleus, and e is the electron charge.

The Hamiltonian of the 3-level free atom can be expressed as:

$$H_0 = \hbar\omega_a |a\rangle \langle a| + \hbar\omega_b |b\rangle \langle b| + \hbar\omega_c |c\rangle \langle c| \equiv \begin{bmatrix} \hbar\omega_a & 0 & 0 \\ 0 & \hbar\omega_b & 0 \\ 0 & 0 & \hbar\omega_c \end{bmatrix} \tag{5.11}$$

For the transition between states $|m\rangle$ and $|n\rangle$, the atomic dipolar moment may be written in the basis of the atomic states by:

$$\vec{d} = \vec{d}_{mn}(|n\rangle\langle m| + |m\rangle\langle n|). \tag{5.12}$$

In particular,

$$\vec{d}_{pr} = \vec{d}_{ba}(|a\rangle\langle b| + |b\rangle\langle a|) = \begin{bmatrix} 0 & \vec{d}_{ba} & 0 \\ \vec{d}_{ba} & 0 & 0 \\ 0 & 0 & 0 \end{bmatrix} \tag{5.13}$$

$$\vec{d}_{pu} = \vec{d}_{ca}(|a\rangle\langle c| + |c\rangle\langle a|) = \begin{bmatrix} 0 & 0 & \vec{d}_{ca} \\ 0 & 0 & 0 \\ \vec{d}_{ca} & 0 & 0 \end{bmatrix} \tag{5.14}$$

In order to find the interaction potential energy due to the probe laser in the same basis, we use Eqs. (5.9) and (5.13), obtaining:

$$V_{pr} = -\vec{d}_{ba}(|a\rangle\langle b| + |b\rangle\langle a|).\vec{E}_{pr_0}\frac{1}{2}(\mathrm{e}^{-i\omega_{pr}t} + \mathrm{e}^{i\omega_{pr}t}) \tag{5.15}$$

$$= -\frac{\vec{d}_{ba}.\vec{E}_{pr_0}}{2}(|a\rangle\langle b|\,\mathrm{e}^{-i\omega_{pr}t} + |a\rangle\langle b|\,\mathrm{e}^{i\omega_{pr}t} + |b\rangle\langle a|\,\mathrm{e}^{-i\omega_{pr}t} + |b\rangle\langle a|\,\mathrm{e}^{i\omega_{pr}t}) \tag{5.16}$$

where the terms with $\mathrm{e}^{-i\omega_{pr}t}$ are associated to the absorption of a photon, whereas the terms with $\mathrm{e}^{i\omega_{pr}t}$ are associated with the emission of a photon [90].

In the rotating wave approximation (RWA), for $|\omega - \omega_0| \ll \omega_0$ we can neglect the terms associated with the absorption of a photon and a transition from an excited state to the fundamental state, as well as associated with the emission of a photon and a transition from the fundamental state to an excited state. Therefore we have:

$$V_{pr} = \frac{\hbar\Omega_{pr}}{2}(|a\rangle\langle b|\,e^{-i\omega_{pr}t} + |b\rangle\langle a|\,e^{i\omega_{pr}t}) \tag{5.17}$$

where we have used the definition of Rabi frequency associated with the states $|a\rangle$ and $|b\rangle$ and the probe field:

$$\Omega_{pr} = -\frac{\vec{d}_{ba}.\vec{E}_{pr_0}}{\hbar}. \tag{5.18}$$

Identically, in matrix notation we have that:

$$V_{pr} = \frac{\hbar\Omega_{pr}}{2}\begin{bmatrix} 0 & \mathrm{e}^{-i\omega_{pr}t} & 0 \\ \mathrm{e}^{i\omega_{pr}t} & 0 & 0 \\ 0 & 0 & 0 \end{bmatrix} \tag{5.19}$$

and, analogously, we obtain:

$$V_{pu} = \frac{\hbar\Omega_{pu}}{2}\begin{bmatrix} 0 & 0 & \mathrm{e}^{-i\omega_{pu}t} \\ 0 & 0 & 0 \\ \mathrm{e}^{i\omega_{pu}t} & 0 & 0 \end{bmatrix} \tag{5.20}$$

Therefore the resulting Hamiltonian of the full system is:

$$H = \begin{bmatrix} \hbar\omega_a & \frac{\hbar\Omega_{pr}}{2}\mathrm{e}^{-i\omega_{pr}t} & \frac{\hbar\Omega_{pu}}{2}\mathrm{e}^{-i\omega_{pu}t} \\ \frac{\hbar\Omega_{pr}}{2}\mathrm{e}^{i\omega_{pr}t} & \hbar\omega_b & 0 \\ \frac{\hbar\Omega_{pu}}{2}\mathrm{e}^{i\omega_{pu}t} & 0 & \hbar\omega_c \end{bmatrix}. \tag{5.21}$$

From Eq. (5.5) and (5.7) we have, for the off-diagonal elements, that:

$$\dot{\rho}_{mn} = \frac{i}{\hbar}((\rho H)_{mn} - (H\rho)_{mn}) - \gamma_{mn}\rho_{mn} \tag{5.22}$$

Then, using the definition of the full Hamiltonian of this system, Eq. (5.21), in Eq. (5.22), we obtain:

$$\dot{\rho}_{ab} = (i(\omega_b - \omega_a) - \gamma_{ab})\rho_{ab} + i\frac{\Omega_{pr}}{2}\mathrm{e}^{-i\omega_{pr}t}(\rho_{aa} - \rho_{bb}) - i\frac{\Omega_{pu}}{2}\mathrm{e}^{-i\omega_{pu}t}\rho_{cb} \tag{5.23}$$

$$\dot{\rho}_{ac} = -(i(\omega_a - \omega_c) + \gamma_{ac})\rho_{ac} + i\frac{\Omega_{pu}}{2}\mathrm{e}^{-i\omega_{pu}t}(\rho_{aa} - \rho_{cc}) - i\frac{\Omega_{pr}}{2}\mathrm{e}^{-i\omega_{pr}t}\rho_{bc} \tag{5.24}$$

$$\dot{\rho}_{cb} = -(i(\omega_c - \omega_b) + \gamma_{cb})\rho_{cb} + i\frac{\Omega_{pr}}{2}\mathrm{e}^{-i\omega_{pr}t}\rho_{ca} - i\frac{\Omega_{pu}}{2}\mathrm{e}^{i\omega_{pu}t}\rho_{ab} \tag{5.25}$$

It is useful to introduce the slow variables:

$$\tilde{\rho}_{ab} = \rho_{ab}\mathrm{e}^{i\omega_{pr}t} \tag{5.26}$$

$$\tilde{\rho}_{ac} = \rho_{ac}\mathrm{e}^{i\omega_{pu}t} \tag{5.27}$$

$$\tilde{\rho}_{cb} = \rho_{cb}\mathrm{e}^{i(\omega_{pr}-\omega_{pu})t} \tag{5.28}$$

and the following formulas for the detuning between atomic and optical frequencies,

$$\delta_{pr} = \omega_{pr} - \omega_a + \omega_b \tag{5.29}$$

$$\delta_{pu} = \omega_{pu} - \omega_a + \omega_c \tag{5.30}$$

with which we obtain:

$$\dot{\tilde{\rho}}_{ab} = -(\gamma_{ab} - i\delta_{pr})\tilde{\rho}_{ab} + i\frac{\Omega_{pr}}{2}(\rho_{aa} - \rho_{bb}) - i\frac{\Omega_{pu}}{2}\tilde{\rho}_{cb} \tag{5.31}$$

$$\dot{\tilde{\rho}}_{ac} = -(\gamma_{ac} - i\delta_{pu})\tilde{\rho}_{ac} + i\frac{\Omega_{pu}}{2}(\rho_{aa} - \rho_{cc}) - i\frac{\Omega_{pr}}{2}\tilde{\rho}_{bc} \tag{5.32}$$

$$\dot{\tilde{\rho}}_{cb} = -(\gamma_{cb} - i(\delta_{pr} - \delta_{pu}))\tilde{\rho}_{cb} + i\frac{\Omega_{pr}}{2}\tilde{\rho}_{ca} - i\frac{\Omega_{pu}}{2}\tilde{\rho}_{ab} \tag{5.33}$$

On the steady state, the time derivatives of the density matrix elements vanish, i.e. $\dot{\rho}_{ij} = 0$. In addition, we assume that for small probe powers the population of the ground state is always approximately equal to 100% and the other populations are approximately equal to 0%:

$$\rho_{bb}(t) \approx 1; \tag{5.34}$$

$$\rho_{aa}(t) \approx 0; \quad \rho_{cc}(t) \approx 0. \tag{5.35}$$

Therefore, using these approximations in Eqs. (5.31)-(5.33), we obtain:

$$0 \approx -(\gamma_{ab} - i\delta_{pr})\tilde{\rho}_{ab} - i\frac{\Omega_{pr}}{2} - i\frac{\Omega_{pu}}{2}\tilde{\rho}_{cb} \tag{5.36}$$

$$0 \approx -(\gamma_{ac} - i\delta_{pu})\tilde{\rho}_{ac} - i\frac{\Omega_{pr}}{2}\tilde{\rho}_{bc} \tag{5.37}$$

$$0 \approx -(\gamma_{cb} - i(\delta_{pr-\delta_{pu}}))\tilde{\rho}_{cb} + i\frac{\Omega_{pr}}{2}\tilde{\rho}_{ca} - i\frac{\Omega_{pu}}{2}\tilde{\rho}_{ab}, \tag{5.38}$$

from which we obtain that, for $\Omega_{pr} \ll \Omega_{pu}$:

$$\tilde{\rho}_{ab} = -i\frac{\Omega_{pr}}{2}\left[\gamma_{ab} - i\delta_{pr} + \frac{(\Omega_{pu}/2)^2}{\gamma_{cb} - i(\delta_{pr} - \delta_{pu})}\right]^{-1}. \tag{5.39}$$

Using Eq. (5.2), we have for $\langle d_{pr}\rangle$:

$$\langle d_{pr}\rangle = \mathrm{Tr}(\rho d_{pr}) \tag{5.40}$$

$$= \mathrm{Tr}\left(\begin{bmatrix}\rho_{aa} & \rho_{ab} & \rho_{ac}\\ \rho_{ba} & \rho_{bb} & \rho_{bc}\\ \rho_{ca} & \rho_{cb} & \rho_{cc}\end{bmatrix}\begin{bmatrix}0 & d_{pr_{ba}} & 0\\ d_{pr_{ba}} & 0 & 0\\ 0 & 0 & 0\end{bmatrix}\right) \tag{5.41}$$

$$= \rho_{ab} d_{ba} + \rho_{ba} d_{ba} \tag{5.42}$$

$$= d_{ba}(\tilde{\rho}_{ab} \mathrm{e}^{-i\omega_{pr}t} + \tilde{\rho}_{ba} \mathrm{e}^{i\omega_{pr}t}) \tag{5.43}$$

The polarization of the medium is the product of the average dipolar moment by the number of atoms or molecules per unit volume, n_m, in the form:

$$P = n_m \langle d \rangle \tag{5.44}$$

On the other hand, in the linear approximation, the polarization is:

$$P = \epsilon_0 \chi E_{pr} = \epsilon_0 \chi \frac{E_{pr_0}}{2} (\mathrm{e}^{-i\omega_{pr}t} + \mathrm{e}^{i\omega_{pr}t}); \tag{5.45}$$

therefore, by combining Eqs. (5.44)-(5.45), (5.43), and (5.18) we obtain:

$$\chi = -\frac{2 n_m d_{ba}^2 \tilde{\rho}_{ab}}{\epsilon_0 \hbar \Omega_{pr}}, \tag{5.46}$$

with which we obtain the refractive index:

$$n = \sqrt{1 + \chi}. \tag{5.47}$$

Finally, using Eqs. 5.47, 5.46, and 5.39 we find the complex susceptibility of the medium and its complex refractive index, n:

$$n = \sqrt{1 - \frac{n_m d_{ba}^2}{\epsilon_0 \hbar} \left\{ -i / \left[\gamma_{ab} - i\delta_{pr} + \frac{(\Omega_{pu}/2)^2}{\gamma_{cb} - i(\delta_{pr} - \delta_{pu})} \right] \right\}} \tag{5.48}$$

In Figs. 5.2-5.3 we show EIT graphs with the dependence on various parameters, namely for distinct γ_{ab}, and γ_{bc}. We observe that the values of γ_{ab}, and γ_{bc} affect the overall shape of the EIT graphs.

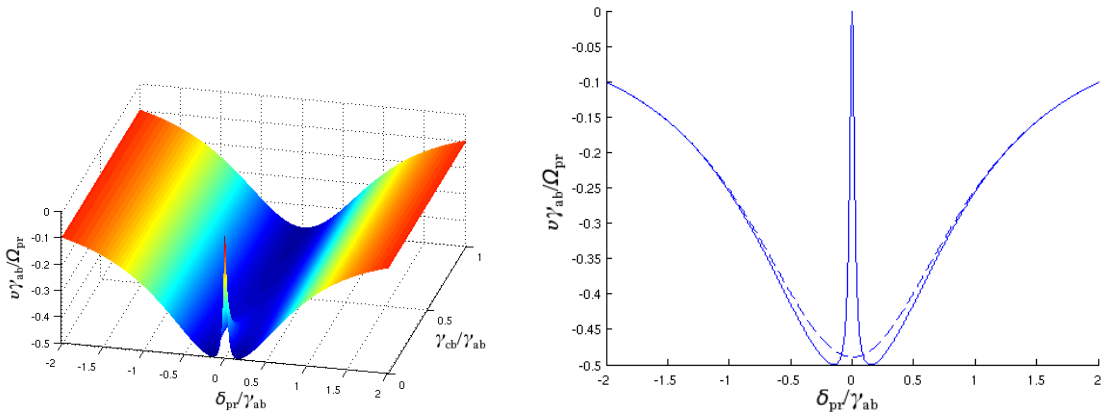

Fig. 5.2: a) Three dimensional plot showing the dependence of v =Im$\{\tilde{\rho}_{ab}\}$ on δ_{pr} and γ_{cb}/γ_{ab}; b) the two extremes of the graph at left. - after ref. [90, fig. 3.4.i].

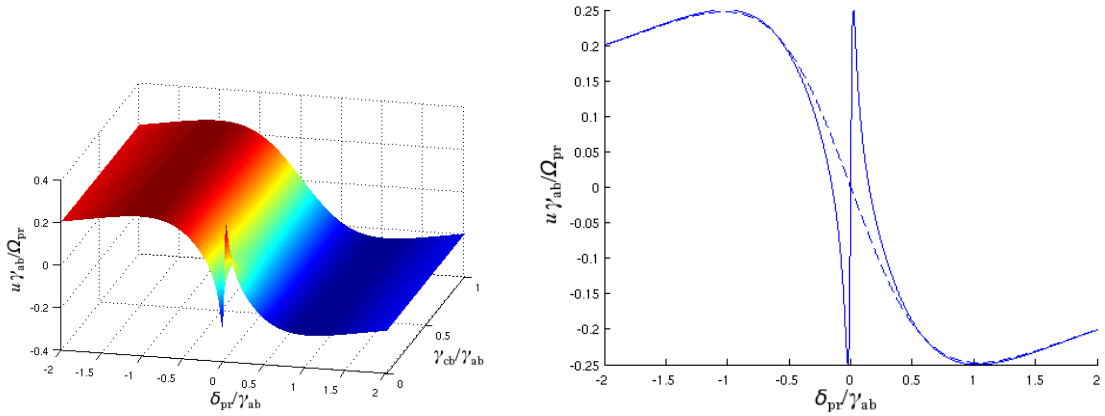

Fig. 5.3: a) Three dimensional plot showing the dependence of u =Re$\{\tilde{\rho}_{ab}\}$ on δ_{pr} and γ_{cb}/γ_{ab}; b) the two extremes of the graph at left.

5.3.2 Ladder systems

In a ladder system the relevant levels of that system have the form shown on Fig. 5.4, where the ground state was defined as $|b\rangle$ for a mathematical convenience of comparison between the Λ and the ladder systems, but $|a\rangle$ and $|c\rangle$ levels differ in their location. The Hamiltonian of a ladder system, in the rotating wave approximation, differs from the previous one (in the Eq. (5.21)), being now given by:

$$H_l = \begin{bmatrix} \hbar\omega_a & \frac{\hbar\Omega_{pr}}{2}\mathrm{e}^{-i\omega_{pr}t} & \frac{\hbar\Omega_{pu}}{2}\mathrm{e}^{i\omega_{pu}t} \\ \frac{\hbar\Omega_{pr}}{2}\mathrm{e}^{i\omega_{pr}t} & \hbar\omega_b & 0 \\ \frac{\hbar\Omega_{pu}}{2}\mathrm{e}^{-i\omega_{pu}t} & 0 & \hbar\omega_c \end{bmatrix} \tag{5.49}$$

where the signal that differs results from the different level structure.

In consequence $\dot{\rho}_{ab}$, $\dot{\rho}_{ac}$, and $\dot{\rho}_{bc}$ are given by:

$$\dot{\rho}_{ab} = (i(\omega_b - \omega_a) - \gamma_{ab})\rho_{ab} + i\frac{\Omega_{pr}}{2}\mathrm{e}^{-i\omega_{pr}t}(\rho_{aa} - \rho_{bb}) - i\frac{\Omega_{pu}}{2}\mathrm{e}^{-i\omega_{pu}t}\rho_{cb} \tag{5.50}$$

$$\dot{\rho}_{ac} = -(i(\omega_a - \omega_c) + \gamma_{ac})\rho_{ac} + i\frac{\Omega_{pu}}{2}\mathrm{e}^{i\omega_{pu}t}(\rho_{aa} - \rho_{cc}) - i\frac{\Omega_{pr}}{2}\mathrm{e}^{-i\omega_{pr}t}\rho_{bc} \tag{5.51}$$

$$\dot{\rho}_{cb} = -(i(\omega_c - \omega_b) + \gamma_{cb})\rho_{cb} + i\frac{\Omega_{pr}}{2}\mathrm{e}^{-i\omega_{pr}t}\rho_{ca} - i\frac{\Omega_{pu}}{2}\mathrm{e}^{-i\omega_{pu}t}\rho_{ab}. \tag{5.52}$$

Those expressions can be simplified by defining the appropriate slow variables, which for a ladder system we write as:

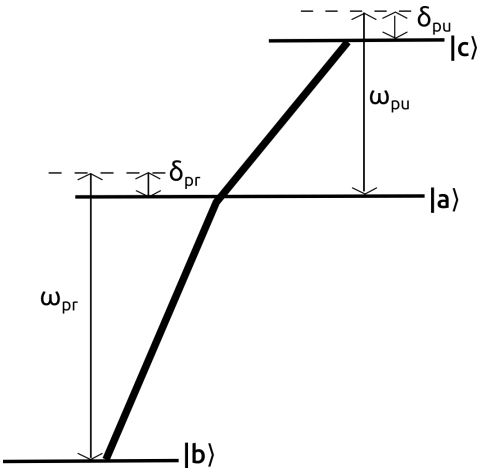

Fig. 5.4: The energy levels of a ladder-type configuration.

$$\tilde{\rho}_{ab} = \rho_{ab} \mathrm{e}^{i\omega_{pr}t} \tag{5.53}$$

$$\tilde{\rho}_{ac} = \rho_{ac} \mathrm{e}^{-i\omega_{pu}t} \tag{5.54}$$

$$\tilde{\rho}_{cb} = \rho_{cb} \mathrm{e}^{i(\omega_{pr}+\omega_{pu})t} \tag{5.55}$$

Finally, we assume the steady state and that $\rho_{bb} \approx 1; \rho_{aa} \approx 0; \rho_{cc} \approx 0$. Therefore, we find:

$$\tilde{\rho}_{ab} = -i\frac{\Omega_{pr}}{2} \Big/ \left[\gamma_{ab} - i\delta_{pr} + \frac{(\Omega_{pu}/2)^2}{\gamma_{cb} - i(\delta_{pr}+\delta_{pu})}\right]. \tag{5.56}$$

5.3.3 Vee systems

In the case of a vee system (usually denoted by V), the energy levels configuration are as in Fig. 5.5. The Hamiltonian in this case is given by:

$$H_V = \begin{bmatrix} \hbar\omega_a & \frac{\hbar\Omega_{pr}}{2}\mathrm{e}^{i\omega_{pr}t} & \frac{\hbar\Omega_{pu}}{2}\mathrm{e}^{i\omega_{pu}t} \\ \frac{\hbar\Omega_{pr}}{2}\mathrm{e}^{-i\omega_{pr}t} & \hbar\omega_b & 0 \\ \frac{\hbar\Omega_{pu}}{2}\mathrm{e}^{-i\omega_{pu}t} & 0 & \hbar\omega_c \end{bmatrix} \tag{5.57}$$

In this case, the time governing equations for each ρ_{ij}, are:

$$\dot{\rho}_{ab} = (i(\omega_b - \omega_a) - \gamma_{ab})\rho_{ab} + i\frac{\Omega_{pr}}{2}\mathrm{e}^{i\omega_{pr}t}(\rho_{aa} - \rho_{bb}) - i\frac{\Omega_{pu}}{2}\mathrm{e}^{-i\omega_{pu}t}\rho_{cb} \tag{5.58}$$

$$\dot{\rho}_{ac} = -(i(\omega_a - \omega_c) + \gamma_{ac})\rho_{ac} + i\frac{\Omega_{pu}}{2}\mathrm{e}^{i\omega_{pu}t}(\rho_{aa} - \rho_{cc}) - i\frac{\Omega_{pr}}{2}\mathrm{e}^{i\omega_{pr}t}\rho_{bc} \tag{5.59}$$

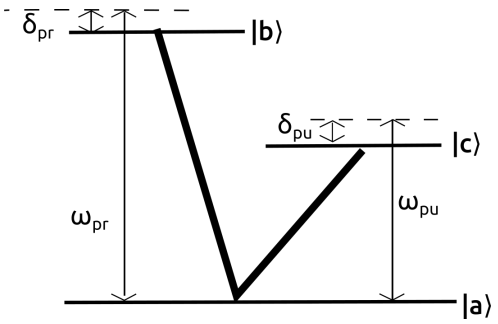

Fig. 5.5: The energy levels of a V-type configuration.

$$\dot{\rho}_{cb} = -(i(\omega_c - \omega_b) + \gamma_{cb})\rho_{cb} + i\frac{\Omega_{pr}}{2}\mathrm{e}^{i\omega_{pr}t}\rho_{ca} - i\frac{\Omega_{pu}}{2}\mathrm{e}^{-i\omega_{pu}t}\rho_{ab} \tag{5.60}$$

The convenient slow-variables in this case are:

$$\tilde{\rho}_{ab} = \rho_{ab}\mathrm{e}^{-i\omega_{pr}t} \tag{5.61}$$

$$\tilde{\rho}_{ac} = \rho_{ac}\mathrm{e}^{-i\omega_{pu}t} \tag{5.62}$$

$$\tilde{\rho}_{cb} = \rho_{cb}\mathrm{e}^{i(-\omega_{pr}+\omega_{pu})t} \tag{5.63}$$

Finally, we introduce the approximate populations of these 3-level system as: $\rho_{aa} \approx 1; \rho_{bb} \approx 0; \rho_{cc} \approx 0$, and in the steady state we obtain:

$$\tilde{\rho}_{ab} = \frac{i\frac{\Omega_{pr}}{2}}{-(i\delta_{pr} - \gamma_{ab}) + \frac{(i\Omega_{pu}/2)^2}{i(-\delta_{pr}+\delta_{pu})-\gamma_{bc}}} \times \left\{-1 + \frac{(i\Omega_{pu}/2)^2}{-(i\delta_{pu} + \gamma_{ac})(i(-\delta_{pr} + \delta_{pu}) - \gamma_{bc})}\right\}. \tag{5.64}$$

5.4 EIT - experimental results

In a EIT configuration, the refractive index depends on several parameters of the system, whose dependence for a Λ-system is indicated in Eq. (5.48). In fact, the refractive index depends on the atoms/molecules density, the atomic dipolar moment of the transition associated with the probe laser, the power of the pump laser, and the detuning of each laser as well as on the relaxation times of the coherences. In particular, the detuning of the probe laser, i.e. the difference $\delta_{pr} = \omega_{pr} - 2\pi c/\lambda_0$ has an important consequence: for $\delta_{pr} = 0$, i.e. at the centre of an EIT window, the transmission can reach 100%.

In Figs. 5.6 we observe experimental results for the transmission from other authors [38, 43, 114]. These graphs show a typical behaviour of the transmission under the EIT phenomenon; however they are different because each system has its own parameters and,

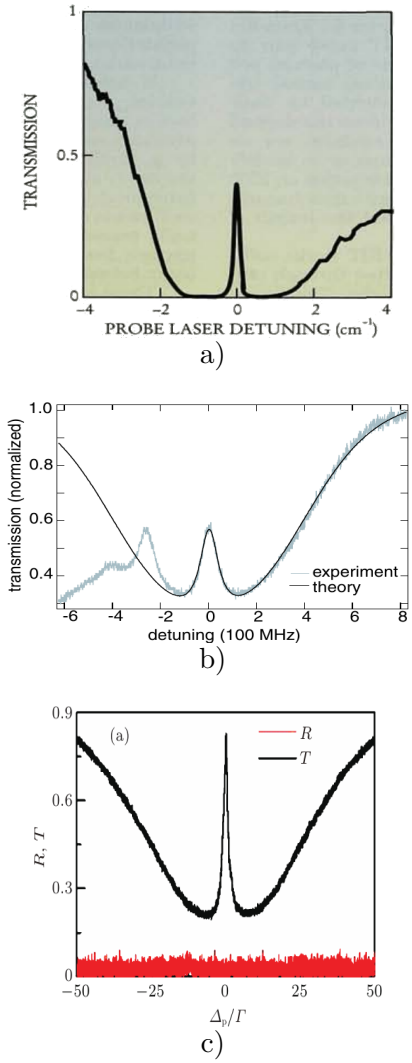

Fig. 5.6: EIT transmissions: a) S.E. Harris [43] result; b) S. Ghosh [38] result; and c) D. Wang [114] result.

in particular, in a) the material is strontium, in b) the material is rubidium, and in c) the material is cesium.

We have chosen to work with the rubidium material. The electron configuration of rubidium is: $1s^2\ 2s^2\ 2p^6\ 3s^2\ 3p^6\ 4s^2\ 3d^{10}\ 4p^6\ 5s^1$, where the upper numbers are the numbers of electrons in each orbital, whose sum is Z=37, the atomic number of rubidium. The valence electron of the level 5s has the quantum numbers n=5 (principal quantum number), l=0 (azimuthal quantum number), m=0 (magnetic quantum number), and s=1/2 (spin quantum number). Moreover, the 5s level has an hyperfine structure, so that this level is split into two levels with F=1 and F=2. The 3-main levels in our chosen Λ-system of rubidium are: $^5S_{1/2}$ F=1, $^5S_{1/2}$ F=2, and $^5P_{1/2}$, denoted by $|b\rangle$, $|c\rangle$, and $|a\rangle$, respectively. In Fig. 5.7 we plot the

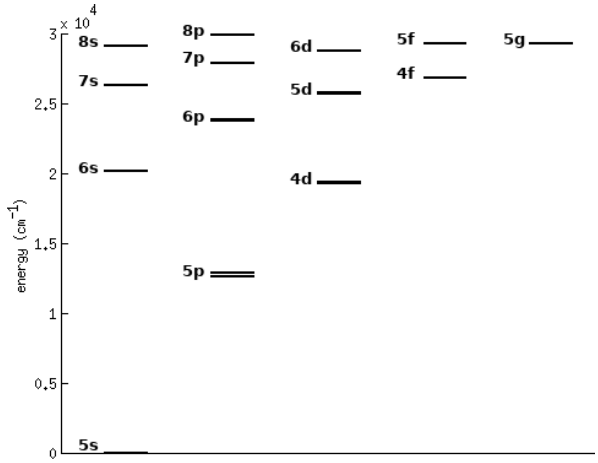

Fig. 5.7: Energy levels diagram of rubidium (considering the conversion reported in ref. [77] of $1\text{cm}^{-1} \leftrightarrow 1.98644561\times10^{-23}\text{J}$).

diagram of the levels of rubidium, whose data values where taken from a table in ref. [96, pp. 308-309].

– ***material*** **:**	
dipolar moments [103]:	$\mu_{ab} = 2.5377 \times 10^{-29}\text{Cm}$, probe transition for rubidium, $\Lambda - system$
	$\mu_{ac} = 2.5377 \times 10^{-29}\text{Cm}$, pump transition for rubidium, $\Lambda - system$
resonance wavelength:	$\lambda_0 = 0.794979\mu\text{m}$
atomic density [50]:	$n_{atoms} \rightarrow eg. : 2.7317764 \times 10^{14} m^{-3}$
atomic mass [74]:	85.4678 (rubidium)
– ***lasers*** **:**	
the intensity of the pump laser:	$\langle I_{pu} \rangle \rightarrow eg. : 1536.4\text{W/m}^2 \longrightarrow 77.8\text{nW}$
probe laser wavelength:	$\lambda_{pr} \rightarrow eg. : [0.7949786, 0.7949794]\mu\text{m}$
pump laser wavelength such that:	$\delta_{pu} = 0.000$
– ***of the system as a whole*** **:**	
γ_{ij}:	considering only population decay: [103]
	$\gamma_{ab} = 36.13/2 \times 10^6\text{Hz}$
	$\gamma_{cb} = 0.0\text{Hz}$
	considering energy-conserving relaxation: [38]
	$\gamma_{ab} \rightarrow eg. : 90 \times 10^6\text{Hz}$
	$\gamma_{cb} \rightarrow eg. : 24 \times 10^6\text{Hz}$
temperature:	Θ: 0.0K, 8.7K[1], or 293.0K

Table 5.1: Default parameters considered in our study of the EIT phenomenon - these parameters were used unless otherwise stated.

[1]The study case with the value of 8.7K was chosen to be at an equal temperature as in the experiment with cold atoms on ref. [94].

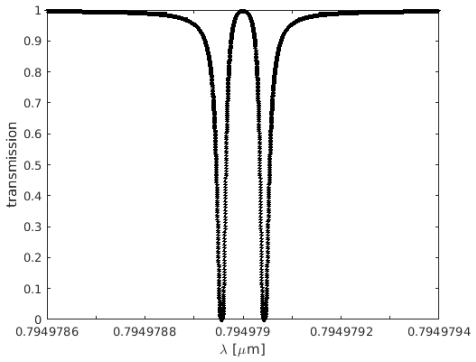

a)

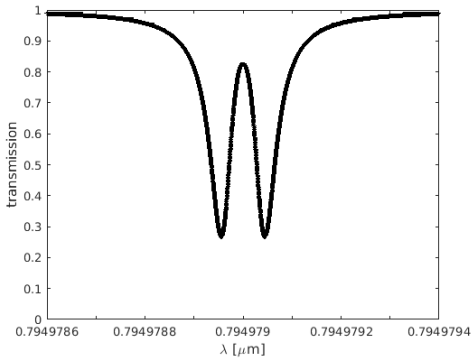

b)

Fig. 5.8: EIT transmission curves in rubidium, with l=0.100m, considering a pump intensity of 1536.4 Wm^{-2}, a) without collisions; b) with collisions.

The Table 5.1 shows some typical and our chosen values of a system with the EIT effect: the parameters of the gas, of the lasers, and of the system as a whole.

The decay rates, γ_{ij}, depend on the experimental conditions and are related to the existence of collisions in the system. When the atoms collide with each other or with the walls of the container, their quantum state suffers changes. This is in the model through the λ_{ij}: if the collisions are more frequent, the relaxation times are smaller and the λ_{ij} are higher. When there are no collisions, for instance at low temperatures, the relaxation times corresponding to γ_{ij} depend only on the spontaneous emissions; in that case for rubidium $\gamma_{ab} = 36.13/2 \times 10^6$Hz, and $\gamma_{cb} = 0.00$Hz. When there are collisions γ_{ij} take higher values.

In Figs. 5.8.a)-b) we observe typical figures of the transmission through rubidium under the EIT effect. Here, we have used Eq. (5.48) that gives the complex refractive index of the system, and the following relations for the material losses, α, and transmission of the medium, T:

$$\alpha = 2k \ \mathrm{Im}(n); \tag{5.65}$$

$$T = \exp(-\alpha l); \tag{5.66}$$

where k is the wavenumber, and l is the propagation length.

In Fig. 5.8.a), for a case without collisions, we observe that the medium becomes fully transparent at the resonant frequency of the rubidium; however, in Fig. 5.8.b), for a case with collisions, the phenomenon is not fully transparent, due to the loss of coherence during collisions. Thus, the shape of the graphs becomes different without or with collisions (in these cases the medium length was taken as 0.100 m).

Figs. 5.9-5.10 show the real and imaginary parts of the refractive index, n. We observe that the imaginary component is symmetrical relatively to the centre wavelength, which is not the case for the real component.

In Fig. 5.11 we observe the effect on the transmission of varying the intensity of the pump, for a medium without collisions. It can be observed that when the pump intensity becomes higher the EIT effect becomes more intense: the high loss sidebands become more separated and the EIT window becomes broader. The same effect is observed in Figs. 5.11.a)-e), in different perspectives. Fig. 5.11.b)-e) shows the transmission profiles for particular values of pump intensity: I=$\{19.7, 197.4, 1974.0, 19739.9\}$Wm^{-2}, which correspond to pump powers P_{pu}=$\{0.001, 0.010, 0.100, 1.000\}\mu$W, in the HC-MOF considered in the next section.

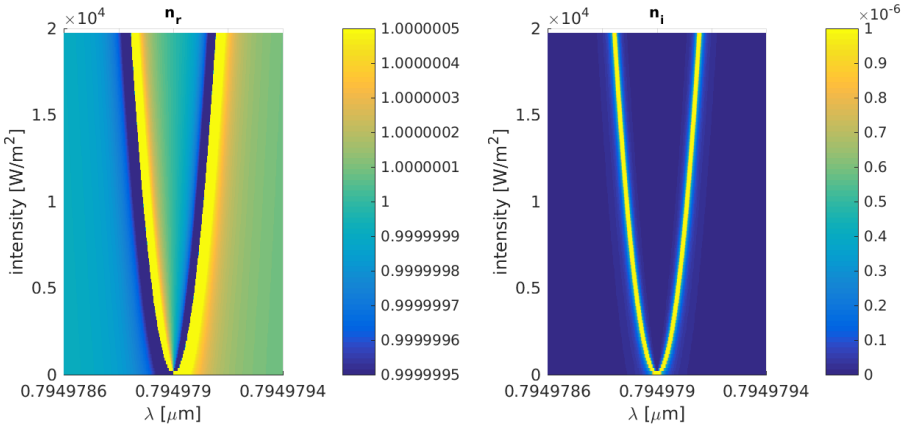

a) b)

Fig. 5.9: Real (a) and imaginary (b) parts of the refractive index for different probe wavelengths, λ, and different intensity of the pump laser, for a system without collisions - with parameters of Table 5.1.

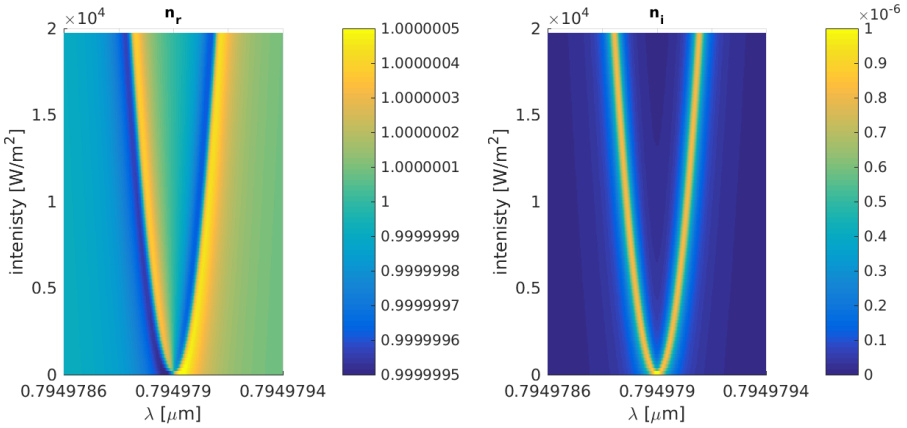

a) b)

Fig. 5.10: Real (a) and imaginary (b) parts of the refractive index for different probe wavelengths, λ, and different intensity of the pump laser, for a system with collisions - with parameters of Table 5.1.

In Fig. 5.12, we have plotted the material dispersion. Since n changes rapidly with frequency on the transparency window, the dispersion is very high and changes considerably.

In figures 5.13-5.14, the difference is that we have considered collisions, but the other parameters are identical to the ones considered for Figs. 5.11-5.12, respectively. The main differences in transmission are analogous to what have been observed between Figs. 5.8.a) and 5.8.b), as discussed above.

In Fig. 5.15 we show how the transmission and the group velocity for λ at the resonance (i.e. at $\lambda = \lambda_0$) vary with the intensity of the pumping laser. In a system without collisions

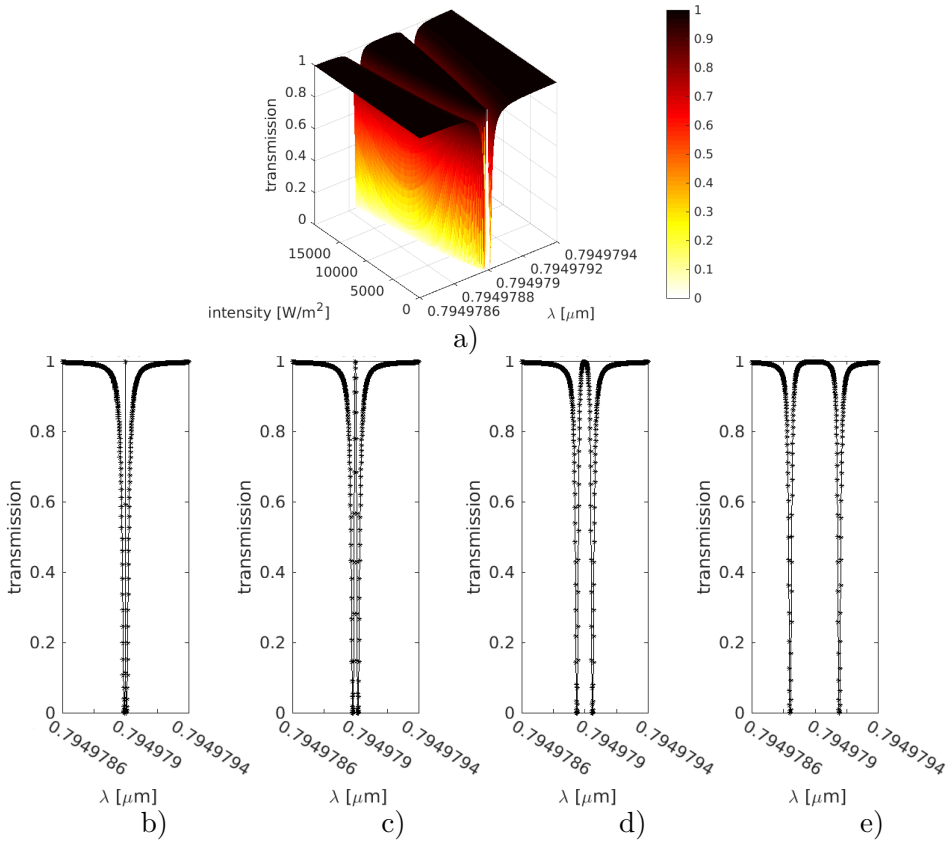

Fig. 5.11: EIT transmission without collisions: a) as a function of I_{pu}, b) I=19.7 Wm^{-2}, c) 197.4 Wm^{-2}, d) 1974.0 Wm^{-2}, e) 19739.9 Wm^{-2}.

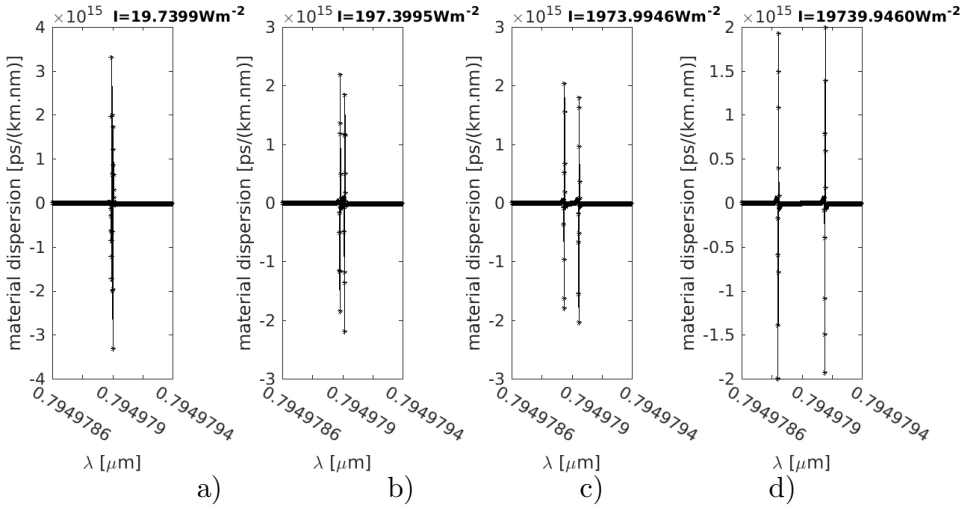

Fig. 5.12: Dispersion under the EIT effect, without collisions for different pump intensities - with parameters of Table 5.1.

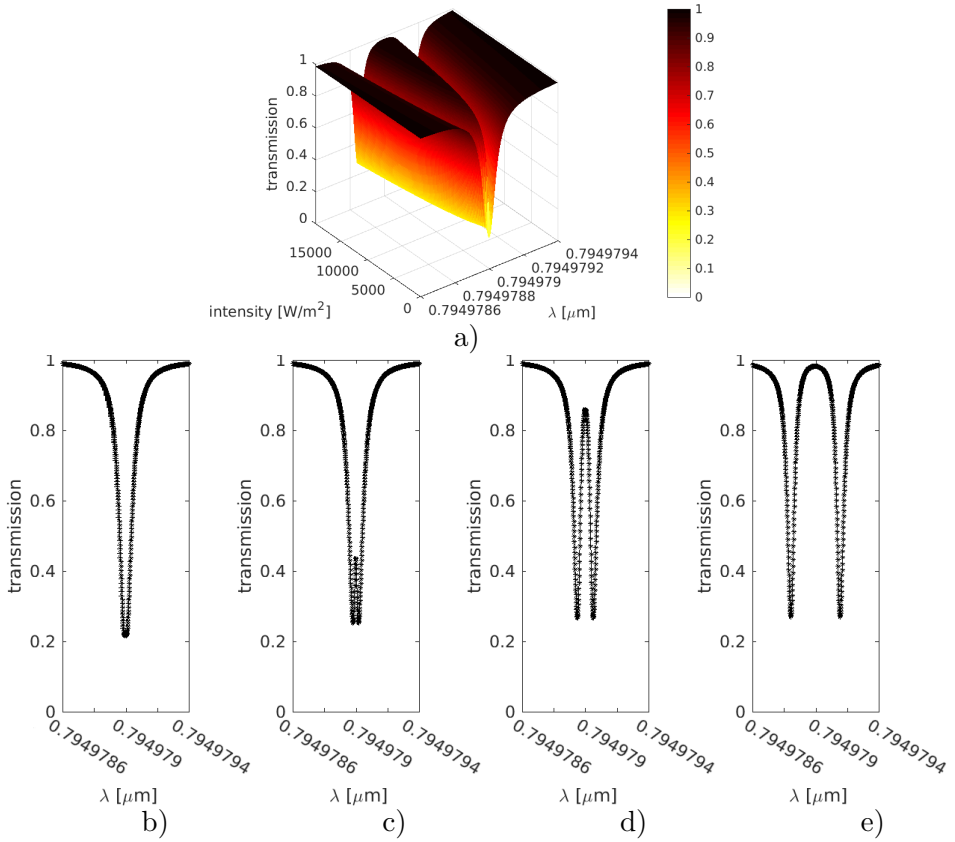

Fig. 5.13: EIT transmission with collisions: a) as a function of I_{pu}, b) I=19.7 Wm^{-2}, c) 197.4 Wm^{-2}, d) 1974.0 Wm^{-2}, e) 19739.9 Wm^{-2}.

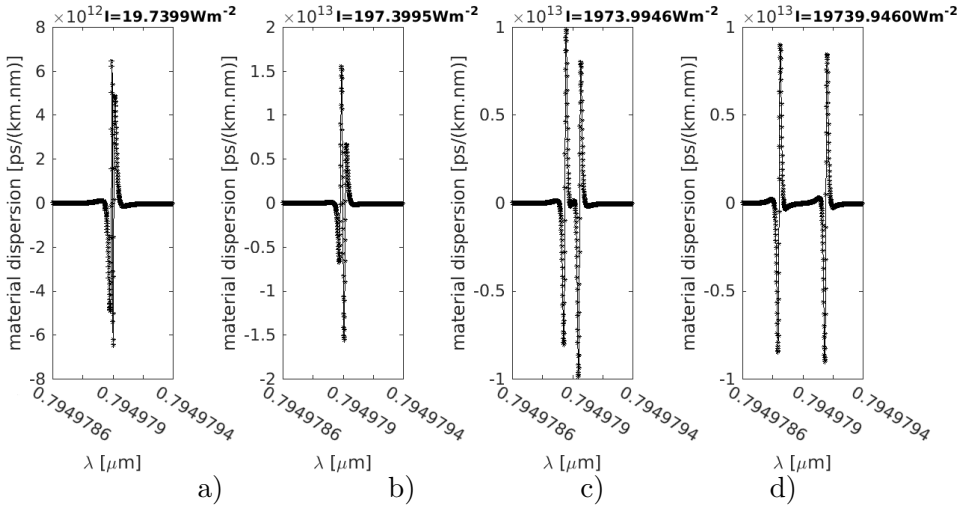

Fig. 5.14: Dispersion under the EIT effect, with collisions for different pump intensities - with parameters of Table 5.1.

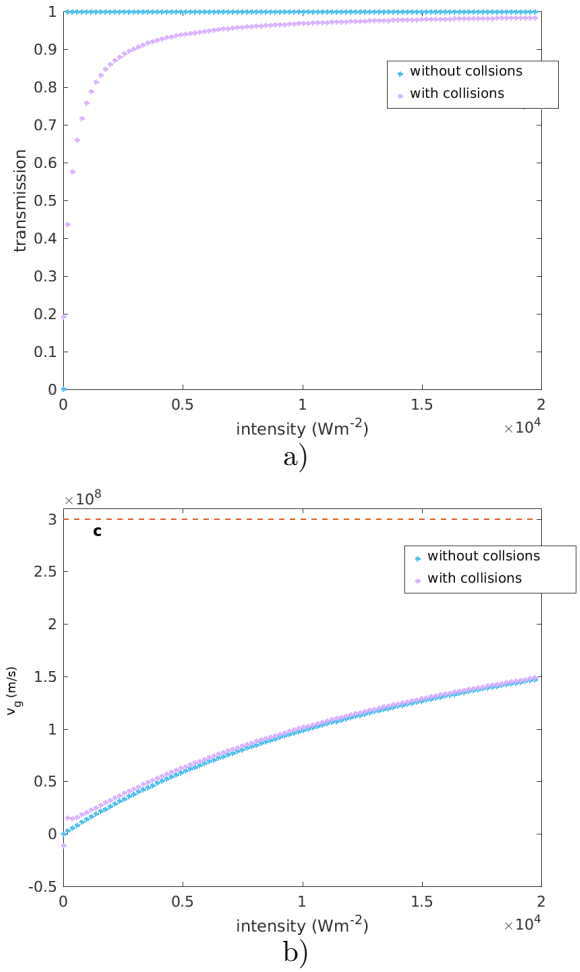

Fig. 5.15: Transmission (a) and group velocity (b), in the case of probe and pump lasers in perfect resonance with the transitions, as a function of the intensity of the pumping laser.

we always have transmission $T = 100\%$, but in a system with collisions the transmission vary with the intensity of the pump, increasing with it. The group velocity for $I_{pu} \gg 0$ is similar in both systems with and without collisions. We predict slow light, i.e. low group velocities in the middle of the EIT window, for low pump intensities. However, that group velocity increases with I_{pu}.

5.5 EIT in microstructured optical fibres

In this section, we aim to study how the guidance affects the EIT phenomena. For this purpose we will consider that the light of the pump laser travels in a hollow core microstructured optical fibre (HC-MOF), whose main parameters are presented in Table 5.2.

– ***fibre*** **:**	
fibre length:	$l \rightarrow eg.: 0.100\text{m}$
fibre's design:	HC-MOF, with Λ=4.0μm, d=3.9μm, and whose cladding is composed by silica and air.
core radius:	$r_{co} = 1.5\Lambda$,
	$a_{\text{eff}} = 5.0659 \times 10^{-11}\text{m}^2$

Table 5.2: HC-MOF parameters considered in our study of the EIT phenomenon; these parameters were used unless otherwise stated.

With Comsol multiphysics we obtained the fundamental mode of the fibre due to the pump laser. We assume that the level $|c\rangle$ is unpopulated, and therefore the pump is not affected by the rubidium: it observes a refractive index of $n = 1$. Then, we have modelled the radial dependence of the mode by a Gaussian function. This radial dependence of the mode field is crucial since it leads to distinct n felt by the probe for distinct values of the radial position, r, inside the fibre's core. The Rabi frequency in this case is:

$$\Omega_{pu} = \Omega_{pu}^{0} f, \tag{5.67}$$

with:

$$f = a_0 \exp\left\{ -\left(\frac{r - b_0}{c_0} \right)^2 \right\} \tag{5.68}$$

In this function a_0 is chosen to be equal to 1 because this means that the maximum of the Ω_{pu} is the Ω_{pu}^{0}; b_0 is chosen to be equal to 0 because this means that the Gaussian top is located at $r = 0$; and c_0 is the main parameter, which is related with the width of the Gaussian and was obtained by an adjustment to the pump mode, as in Figs. 5.16.a) and 5.17.

In Fig. 5.16.a) we show the fundamental mode of fibre for the pump signal which was adjusted to a Gaussian in Fig. 5.17 – for a fibre with core radius r_{co}=1.5Λ=6.0μm (where Λ is the pitch). The fitting parameters of the Gaussian are a_0=1; b_0=0; and c_0=4.083. We have used the same model for the pump field, the Gaussian of Fig. 5.17, for all the studied cases in this section. For other similar fibres we have verified that $c_0' \approx c_0 r_{co}'/r_{co}$, where c_0 and r_{co} are the parameters for the default fibre of Fig. 5.17, and here r_{co}' and c_0' are the parameters for a fibre differing on the scale.

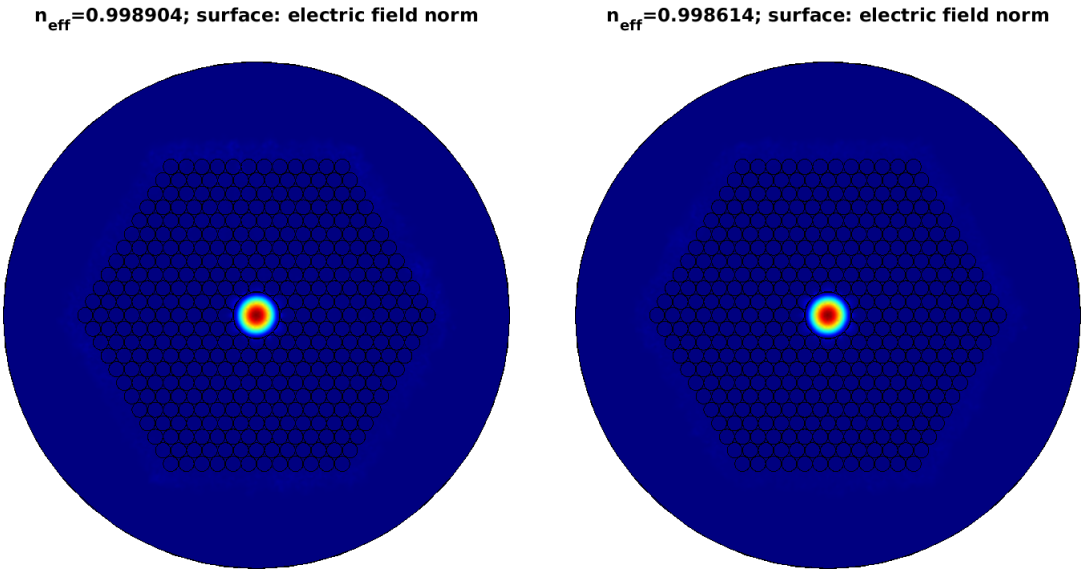

a) b)

Fig. 5.16: a) Fundamental mode of the pump signal, b) fundamental mode of the probe signal at $\lambda_{pu} = \lambda_{pu_0} \approx \lambda_{pr} = \lambda_{pr_0}$, i.e. with pump and probe lasers at perfect resonance conditions, for the fibre of Table 5.2.

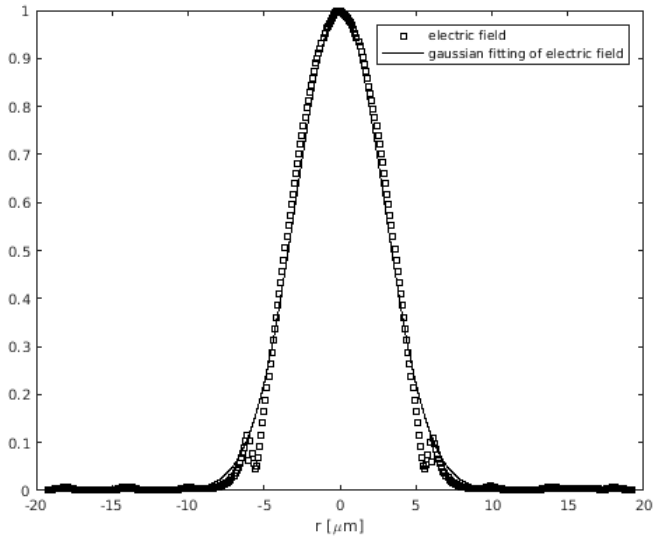

Fig. 5.17: Electric field (normalized) along the direction of the radial coordinate, r, of the fibre's fundamental mode at the pump wavelength, and its approximation by a Gaussian, for the fibre of Table 5.2.

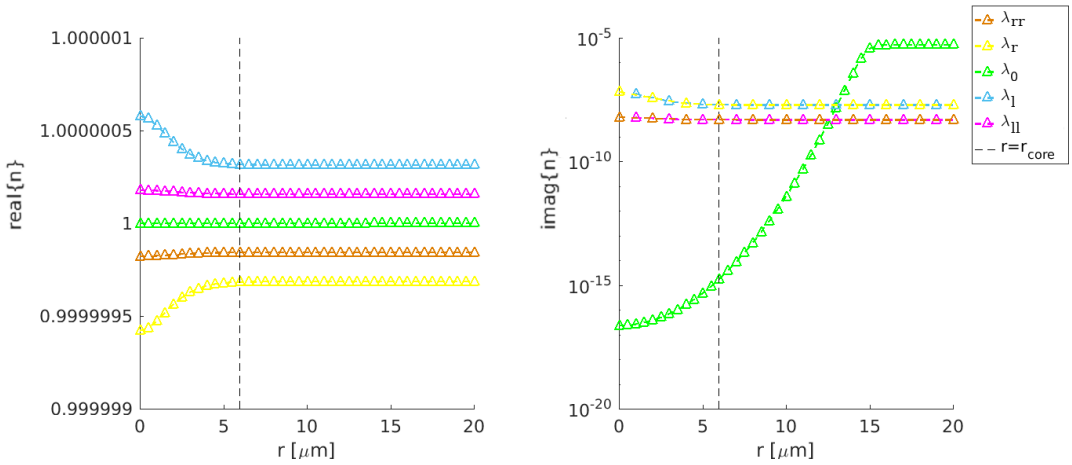

Fig. 5.18: Real and imaginary parts of the refractive index for the cases with λ_{ll}=0.7949788 μm, λ_l=0.7949789 μm, λ_0=0.7949790 μm, λ_r=0.7949791 μm, and λ_{rr}=0.7949792 μm, as a function of the radial coordinate r - without collisions, and with the same parameters as in Tables 5.1-5.2.

Then, we have searched for modes of the probe signal on the same fibre but whose core is filled with rubidium such that n is given by Eq. (5.48), and the fibre's cladding is composed by silica and holes of air. In Fig. 5.16.b) we see the fundamental probe mode for perfect resonance conditions.

As mentioned above, in EIT, the refractive index depends on the intensity of the pumping laser. In consequence, the refractive index felt by the probe varies along the value of the radial coordinate, r, on the fibre. In Fig. 5.18 we show this dependence of the refractive index on the radial coordinate, for a rubidium gas and the radial Gaussian distribution of the pump mode field. We note that the curves of the real part are all different; however curves for the imaginary part have a symmetry relatively to the centre wavelength λ_0, such that the curves for λ_{ll}=0.7949788 μm and λ_{rr}=0.7949792 μm coincide, and the curves for λ_l=0.7949789 μm and λ_r=0.7949791 μm coincide, i.e. they are superimposed.

We have found that the two scenarios: i) rubidium fills the core hole, and ii) rubidium fills the core and cladding holes are different. Here, we have chosen to work with the first scenario.

In Fig. 5.19, we show the local transmission at different points of the fibre along the radial position, r, for a system with collisions. The final transmission depends on the full design of a fibre, but here we also study what we call the local transmission for theoretical analysis purposes. The local transmission is the transmission at a specific r point, depending on the imaginary part of $n(r)$.

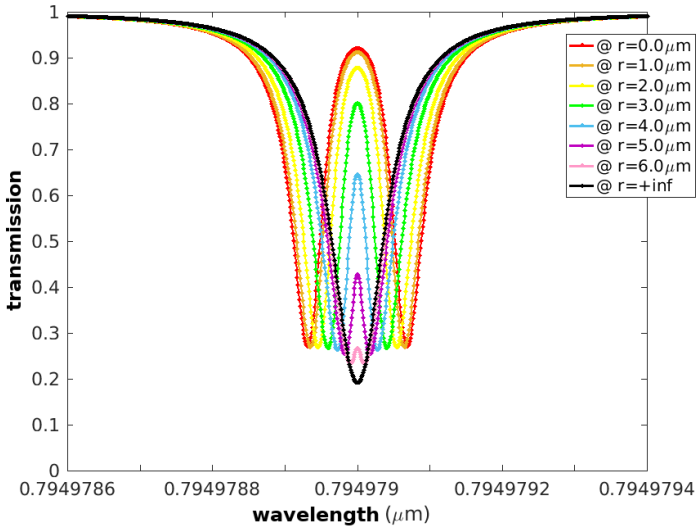

Fig. 5.19: The local transmission for the probe considering collisions, at different values of the radial coordinate, r, and with the parameters of Tables 5.1-5.2.

The radial variation of the mode intensity from $r = 0$ to $r = r_{co}$ for a fibre core filled by a rubidium gas has several consequences. In Fig. 5.20, we plot the local transmission but in a different perspective. We have fixed λ and we have plotted the local transmission all over the transverse section of the fibre's core. Here, we have obtained figures consistent with the results shown in our previous Figs. 5.11 and 5.13: – in Fig. 5.20 for 794.979 nm we see that for this fixed wavelength the local transmission decreases with r, which is due to the increasing of the imaginary part of n with r (as seen in Fig. 5.18); in fact, for an increase in the value of the radial coordinate from 0 to r_{co} there is a decrease of the I_{pu} from max(I_{pu}) to ≈0, which corresponds to moving down along a vertical line in Fig. 5.10.b).

With those plots we show a new characteristic of the EIT phenomena in fibres: the refractive index in an EIT medium filled HC-MOF can be adjusted such that it can have three different types of profiles, which leads to different transmission profiles as shown in Fig. 5.20. The first case shows the local transmission for a probe laser in perfect resonance, the second case shows the local transmission with a probe wavelength distinct but close to that of the resonance, and the third one is for a probe wavelength far from the resonance; the scenarios are clearly different. In particular, in Fig. 5.20.a) for λ =794.979nm we see that the local transmission decreases with r, which is due to the monotonous increase of the imaginary part of n. In Fig. 5.20.b), for λ=794.97903 nm, when increasing r, the imaginary part of the refractive index begins increasing until reaching a maximum value, after which it decreases again; given the symmetry of n_i the result for λ=794.97897 nm is identical. In Fig. 5.20.c),

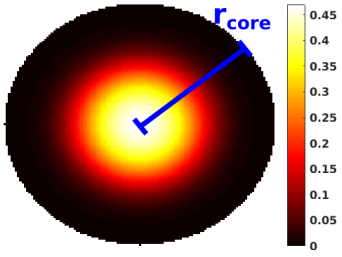

a)

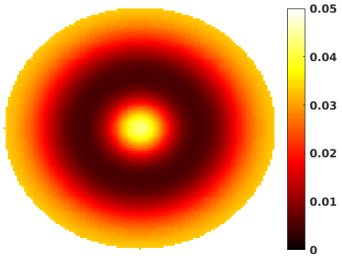

b)

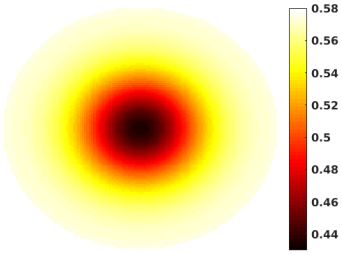

c)

Fig. 5.20: Transverse distribution of the local transmission in the core of the HC-MOF, for probe wavelengths: a) λ_0=794.97900 nm; b) λ=794.97903 nm; and c) λ=794.97910 nm.

for λ=794.97910 nm, the variation of the transmission is opposite to that observed in the first case; the result for λ=794.97890 nm is also identical to this one.

In Figs. 5.21.a)-d) we observe the refractive index of air, n, and the corresponding effective refractive index, n_{eff} for the air-filled HC-MOF. We have made this study to have an insight on how the guidance would affect the fibre's mode without EIT. We note that $\text{Re}\{n\}$ and $\text{Re}\{n_{\text{eff}}\}$ both decrease with $\Delta = -\delta_{pr} + \delta_{pu} = -(\omega_{pr} - 2\pi c/\lambda_0)$. We observe that the result in Fig. 5.21.c) of an air-filled HC-MOF is in agreement with the result in Fig. 5.21.a) of air. In addition, the imaginary part of n_{eff} for this fibre is not null and does not have a symmetrical behaviour relatively to $\lambda_{pr} = \lambda_0$. In fact, it has still some minimal losses due to the not perfect light confinement in the fibre. The behaviour seen on those figures leads to the transmission profiles shown in Figs. 5.22.

Figs. 5.23-5.24 show the effective refractive index obtained for a pump power of 190nW

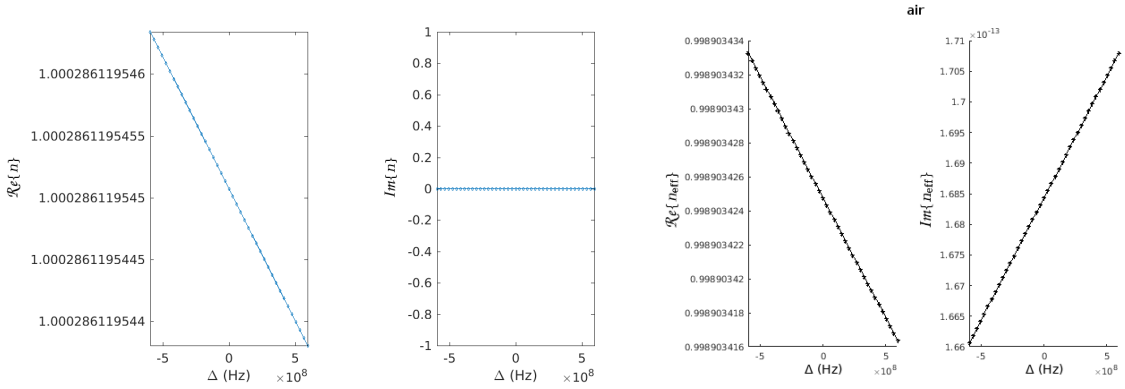

a) b) c) d)

Fig. 5.21: Refractive index of air: (a) real and (b) imaginary parts; effective refractive index of the air filled HC-MOF: (c) real and (d) imaginary parts.

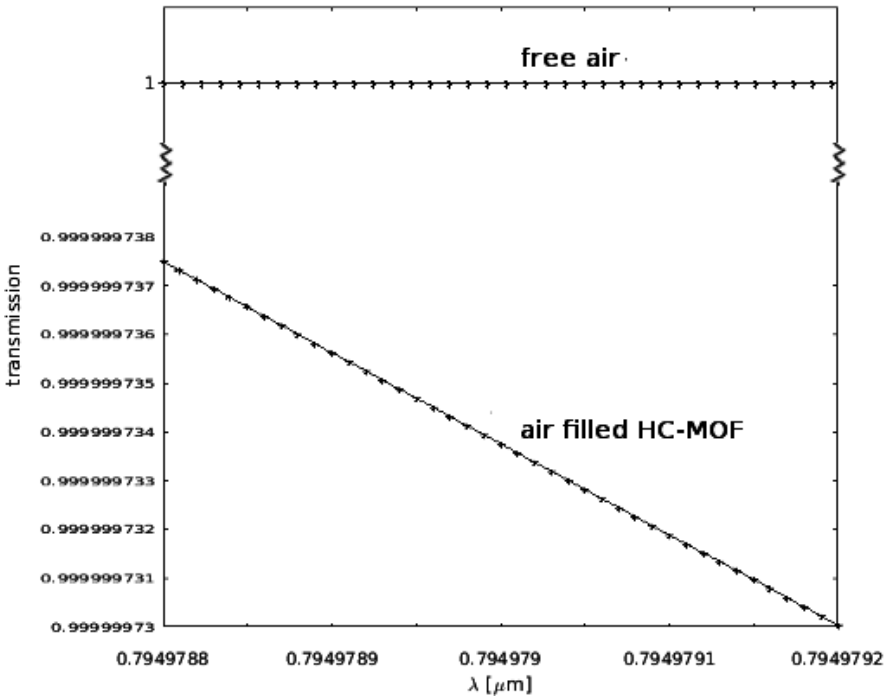

Fig. 5.22: Transmission of air, and transmission of an air filled HC-MOF (two different yy axis regions are shown).

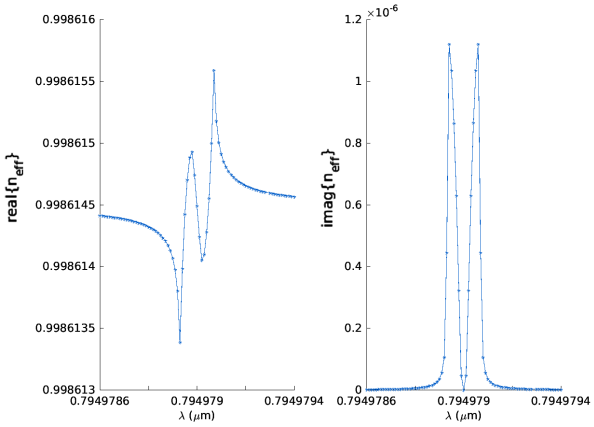

Fig. 5.23: Effective refractive index of a HC-MOF filled with rubidium, without considering collisions in the model.

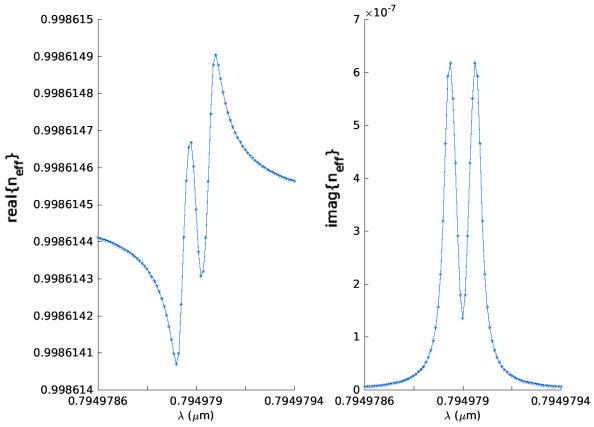

Fig. 5.24: Effective refractive index of a HC-MOF filled with rubidium, considering collisions in the model.

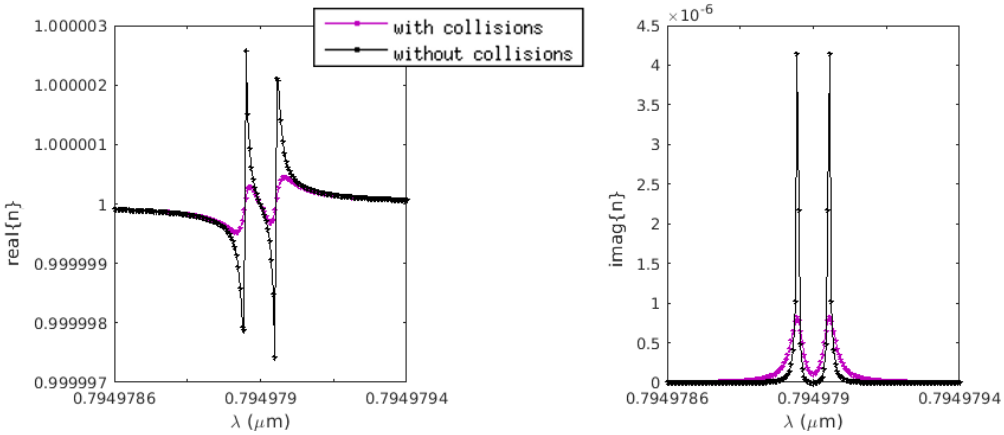

Fig. 5.25: Refractive index with I_{avg}, a) real part; b) imaginary part - with parameters of Tables 5.1-5.2.

not considering and considering collisions, respectively. In the case without collisions, at perfect resonance, the imaginary component of the refractive index vanishes, which leads to a transmission of 100%, whereas in the case with collisions the corresponding transmission is smaller. From the shape of the effective refractive index, the main properties of the system are obtained.

The two curves on Fig. 5.25 show the refractive index with an average intensity, I_{avg}, in the cases of without collisions and with collisions. Here, we observe that with collisions the graphs tend to be smoother.

Then, in Figs. 5.26-5.27 we may observe the transmission profile for Figs. 5.23-5.24. The dots correspond to the effective transmission assuming the Gaussian profile of the pump signal. The other 3 curves in Figs. 5.26 and 5.27 describe the transmission each one for a homogeneous intensity of the pump laser as: at $r = 0$, at $r = r_{co}$, and at an average intensity. In Fig. 5.26-5.27 we note that the transmission profile is different from that in the free gas. The transmission in a HC-MOF have similarities with the other three curves through a complex dependence on the $\text{Im}\{n(r)\}$, where $n(r)$ varies along r. That complex dependence does not have an analytical solution, but it is studied here by numerically solving the master equation for the full HC-MOF, Eq. (2.17), with n described by Eq. (5.48), with the inclusion of Eq. (5.67) which leads to a variation of the pump intensity with r.

In the following we will study the Doppler effect in our system. The Doppler effect is the change in the received frequency of a wave due to the motion of the source, or the motion of the receiver. The resultant frequency is [108]:

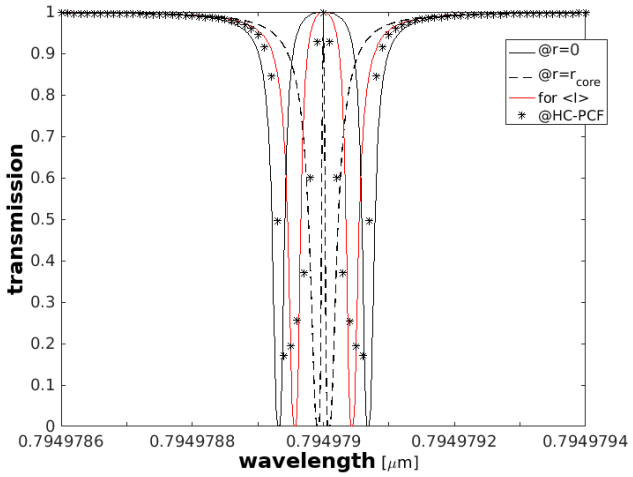

Fig. 5.26: Transmission of the probe after 0.1 m of HC-MOF considering a pump signal of 190 nW and without collisions; for comparison purposes we added three other curves corresponding to the unguided transmission for intensities as in $r = 0$, $r = r_{co}$, and equal to an average intensity.

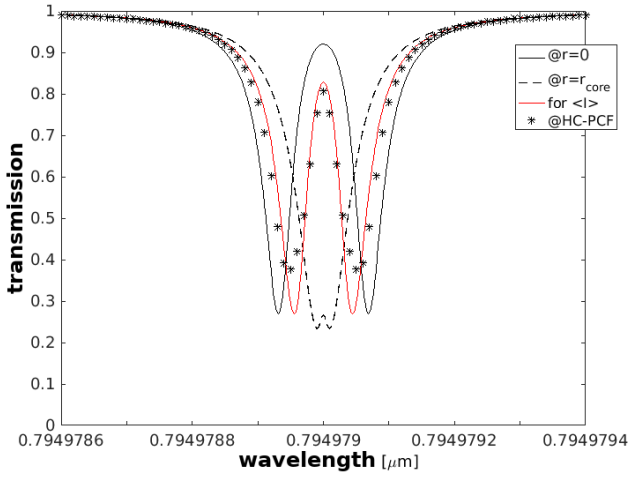

Fig. 5.27: Transmission of the probe after 0.1 m of HC-MOF considering a pump signal of 190 nW and with collisions; for comparison purposes we added three other curves corresponding to the unguided transmission for intensities as in $r = 0$, $r = r_{co}$, and equal to an average intensity.

$$f = \left(\frac{c \pm v_r}{c \pm v_s} \right) f_0, \tag{5.69}$$

which is mathematically equivalent to:

$$f = \left(1 \pm \frac{v_r - v_s}{c \pm v_s} \right) f_0, \tag{5.70}$$

where v_r is the velocity of the receiver, and v_s is the velocity of the source. For considering the Doppler effect on our EIT system we have done the following substitutions, which are valid for $v_s \ll c$:

$$\omega_{pr} = \left(1 + \frac{v_{at}}{c} \right) \omega_{pr0}, \tag{5.71}$$

$$\omega_{pu} = \left(1 + \frac{v_{at}}{c} \right) \omega_{pu0}, \tag{5.72}$$

where v_{at} is the velocity of the atoms or molecules of the gas in the direction of the light propagation.

In fact, Δ_0, δ_{pr0}, and δ_{pu0}, i.e. the values obtained without considering the Doppler effect, depend on ω_{pr} and /or on ω_{pu}. Therefore for including the Doppler effect, they should depend on v_{at}. We find out that we shall do the following substitutions:

$$\delta_{pr} = \delta_{pr0} + k_{pr} v_{at}; \tag{5.73}$$

$$\delta_{pu} = \delta_{pu0} + k_{pu} v_{at}; \tag{5.74}$$

which are valid for an EIT gas [58, chapt. 12].

Moreover, we have for the considered Λ-system of rubidium:

$$\Delta = \delta_{pu} - \delta_{pr} \approx \delta_{pu0} - \delta_{pr0}, \text{ for } k_{pr} \approx k_{pu}. \tag{5.75}$$

where the last equation is valid, since in our system $k_{pr} \approx k_{pu}$.

The distribution of the atomic speed is given by a Maxwellian distribution, whose atomic velocity component in a given direction has a Gaussian shape:

$$f_\Theta(v) = \frac{1}{v_\Theta \sqrt{\pi}} e^{-(v/v_\Theta)^2}, \tag{5.76}$$

where v_Θ is the mean value of the norm of the velocity of the atoms or molecules, which is given by:

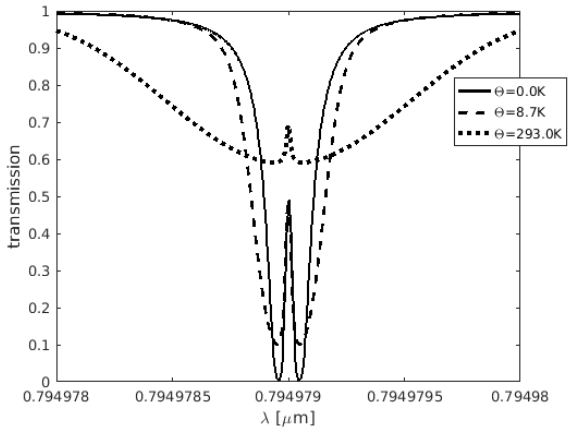

Fig. 5.28: Transmission profile for the probe not guided with /without the Doppler effect, for different temperatures, with collisions, and I_{avg}=1536.4 Wm^{-2}, in a 40 cm medium; the other parameters are those at the Table 5.1.

$$v_\Theta \equiv \langle ||v_{at}|| \rangle = \sqrt{2k_B\Theta/m}, \tag{5.77}$$

where k_B is the Boltzmann constant, Θ is the temperature and m is the mass of the atom of the gas in which we observe the EIT.

Some authors approximate the Gaussian by a Lorentzian function, which is mathematically more simple. In our work, we have considered both approaches, but we have selected the Gaussian model since it gives more accurate results. We start by defining $\tilde{\rho}'_{ab}$ as an integral representing an average through all the velocities each with a specific weight. This is given by the expression:

$$\tilde{\rho}'_{ab} = \int_{-\infty}^{+\infty} \tilde{\rho}_{ab}(v) f_\Theta(v) dv. \tag{5.78}$$

with $f_\Theta(v)$ described as above. As a consequence we obtain:

$$\tilde{\rho}'_{ab} = \Omega_{pr} \frac{\sqrt{\pi}}{2k_{pr}v_\Theta} e^{-z^2} (\text{Erfi}(z) - i), \tag{5.79}$$

with: $z = \left[(\delta_{pr0} + i\gamma_{ab}) + \frac{|\Omega_c|^2}{4(\Delta_0 - i\gamma_{bc})} \right] / (k_{pr}v_\Theta)$, where Erfi is the imaginary error function defined as: $\text{Erfi}(z) = -i\text{Erf}(iz)$, with:

$$\text{Erf}(z) = \frac{2}{\sqrt{\pi}} \int_0^z e^{-t^2} dt. \tag{5.80}$$

In Fig. 5.28 we show the EIT transmission profile under various temperatures, for which we observe different results. The transmission profile in the absence of the Doppler effect

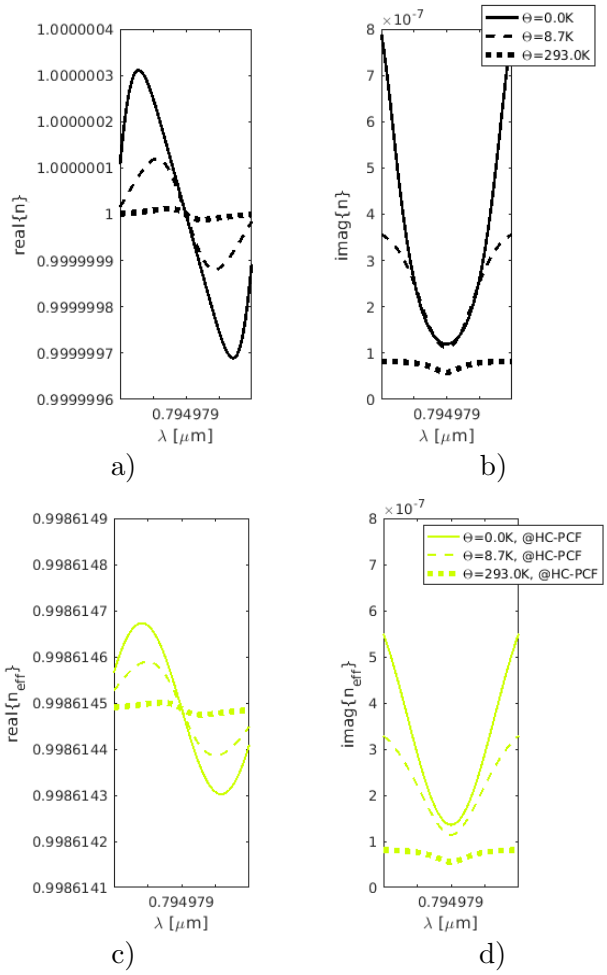

Fig. 5.29: Zoom-in on the EIT window of the refractive index [a)-b)] and effective refractive index on a HC-MOF [c)-d)], including the Doppler effect for various temperatures: 0.0 K, 8.7 K, and 293.0 K - with parameters of Tables 5.1-5.2.

(i.e. if temperature Θ=0.0 K) corresponds to the solid curve. With the Doppler effect, as we increase the temperature, the transmission profile becomes broader, and in the centre of the transmission window in our selected cases the transmission becomes higher (Fig. 5.28).

In Fig. 5.29 we observe a zoom-in window with the variation of the refractive index of free propagation in rubidium, and in the HC-MOF. The Re$\{n_{\text{eff}}\}$ is shifted compared to Re$\{n\}$, while the Im$\{n_{\text{eff}}\}$ is smaller than Im$\{n\}$ for each of the considered temperatures. We see an overall agreement between the properties of the free gas and of the HC-MOF: there is a qualitative similarity, but a quantitative difference. There are distinct characteristics due to the fibre confinement of the pump and probe lasers light.

In Figs. 5.30.a)-f), we present the following characteristics of our EIT system: the transmission, the dispersion, and the group velocity. We have done a zoom-in showing the central

region on which we are interested, where the EIT occurs. In addition, we have obtained effective mode areas that are almost the same for all our cases, which is due to the fact that the fibre's design is maintained the same and the probe laser wavelength is always very close to the centre wavelength λ_0.

The transmission changes when the effect is observed in a HC-MOF, accordingly also with Figs. 5.26-5.27. In Fig. 5.30.a)-b), we have included a zoom-in of the transmission curves for 10 cm, for the free propagation at the selected temperatures of 0 K, 8.7 K and 293 K, as well as for the guided propagation effect. In the middle of the EIT window, for the temperature of 0 K, we obtain a transmission of 47.0% in the case of free propagation, and a transmission of 42.4% in the case of guided light. Thus, we observe that in the case of T=0 K the transmission is slightly lower with guidance; However, in the case of T=293 K the transmission is slightly higher with guidance (70.5%) compared with the free propagation (69.1%), being both those values similar to each other. We also note that in the EIT middle point, at perfect resonance, the transmission increases with increasing temperature.

The dispersion shows a unique profile, such that from Fig. 5.30.c)-d) we deduce that by adjusting the temperature it may be possible to achieve flat dispersion in the exact resonance wavelength at the middle of the EIT window. In the case of the free propagation [Fig. 5.30.c)] we have an almost flat dispersion at the middle point for Θ=0 K, whereas in the case of guidance we have a dispersion curve with a negative slope [Fig. 5.30.d)]. Moreover, the amplitude of the dispersion variation is smaller in the case of guidance, which can be an advantage for the light propagation within a large range of wavelengths. At room temperature, the dispersion is less affected by the guidance.

From Fig. 5.30.e)-f) we observe an interesting behaviour: it is possible to achieve slow-light or fast light in HC-MOFs with EIT. This possibility of combining slow-light or fast-light due to EIT in fibres can find several applications, namely in optical signal processing. Fig. 5.30.e)-f) shows that, in all the studied cases, the centre of the EIT window permits slow light, while in the side-bands of the EIT window, the conditions are favourable for fast light. In particular, we note that for $\Theta \approx 0$ K there are discontinuities at the side-bands, whereas the curves for Θ=293 K are continuous and similar.

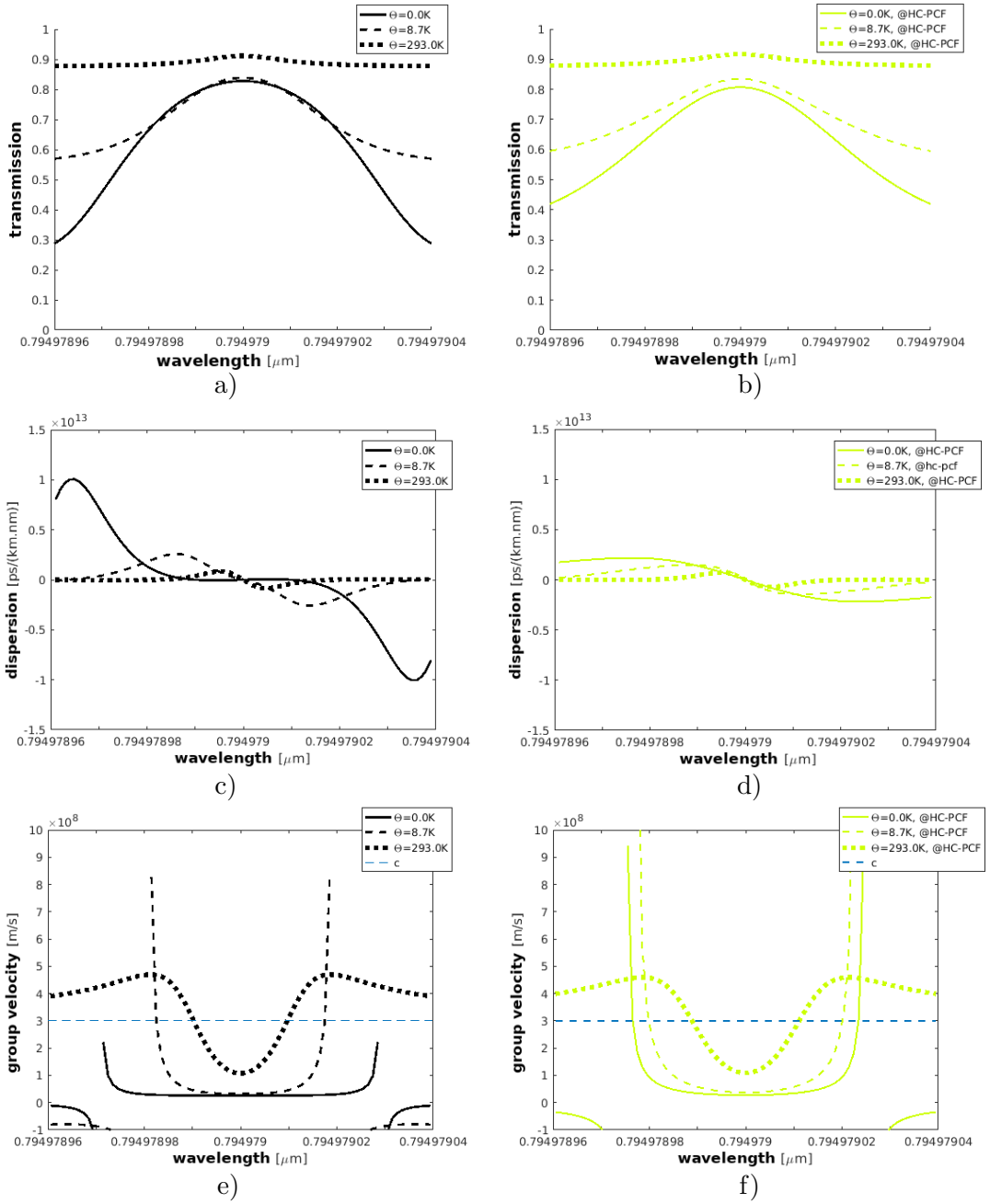

Fig. 5.30: – Transmission (a)-(b), dispersion (c)-(d), and group velocity (e)-(f) in the transparency window considering a system with collisions - at left: in free rubidium, at right: in rubidium confined in the HC-MOF with 10 cm.

5.6 Summary

The EIT phenomenon occurs when a pump field acting in a medium transforms the medium from opaque to transparent in a specific range of frequencies for a probe field. The transmission can reach values of 100%, depending on the systems parameters.

In this chapter we have considered a semi-classical approach: the atomic system is studied using the quantum mechanical formalism, whereas the electromagnetic field is treated by a classical formalism. We have then used the density matrix formalism. We have obtained the complex susceptibility of an EIT medium, for various types of systems: the so-called lambda systems, ladder systems, and vee systems.

The properties of an EIT configuration are well described by the refractive index, which depends on several parameters of the system.

The shape of a typical transmission EIT graph shows a peak in the middle of the window, with high transmission values in the zone of the central wavelength. We have studied the impact of considering the existence or the absence of collisions in the system, as well as the variation of other parameters. The window of the EIT effect has distinct properties, such as group velocity profiles corresponding to slow-light or fast-light.

We have studied the EIT in free gas or inside a hollow-core MOF, comparing both situations. We have made a theoretical fit which shows that the fundamental mode of the HC-MOF created by the pump laser has a transverse Gaussian shape. We have studied the dependence of the refractive index with the radial position of the fibre core that is filled with rubidium. We have investigated the consequences of light confinement on the EIT phenomenon.

The important parameters of an EIT system confined in a HC-MOF are the ones of the material (dipolar moments, resonance wavelength, atoms/molecules density, and atomic mass), the ones of the fibre (core radius, fibre length, and fibre's design), the ones of the lasers (intensity of the pump, probe laser wavelength, and pump laser wavelength), and the ones of the system as a whole (γ_{ij}, and temperature).

The dependence of the transmission of a HC-MOF on that fibre's design and on the several parameters of the system must be studied by computational methods.

Finally, we have studied also the impact of the Doppler effect in the EIT systems, and we have seen distinct profiles, namely: in dispersion, group velocities and transmission, considering both the propagation in free rubidium and the propagation in a HC-MOF.

6 CONCLUSIONS

6.1 Conclusions

We have presented the theoretical background about light propagation in microstructured optical fibres. The main mechanisms that can lead to light guidance in those fibres are the modified TIR, the photonic bandgap effect, or the low density of states. We have presented the equations for finding the propagation modes in fibres and for studying the propagation of pulses. The various microstructured optical fibres (MOFs) can be separated into two categories: the SC-MOFs and the HC-MOFs, accordingly to their core type. Due to the complex patterns that MOFs have, their study is more complicated than that of standard fibres. Thus, the computational methods should be adapted.

The computational methods that we have implemented include: the usage of Comsol multiphysics with Matlab for studying the main properties of the model, such as the mode field, the dispersion and the nonlinearity; the usage of Matlab for studying the pulses propagation; the usage of MPB with Scheme and Matlab for studying the bandgaps and the density of states of HC-MOFs. With such methods we have characterized the fibre's properties, and studied their mechanisms of guidance.

We then have studied various SC-MOFs and HC-MOFs. In particular, we have shown that the LS-MOF model unites adjustable dispersion and high nonlinearity. For a LS-MOF composed by silica and air, we have achieved a nonlinear parameter of $70.0\mathrm{W}^{-1}\ \mathrm{km}^{-1}$, with zero dispersion, simultaneously, at the telecom wavelength of 1.55μm. We have studied the impact of a combination of terms on the pulse propagation in a MOF, as well as the

consequences of isolating each term to perform a more detailed study, which is only possible with numerical methods. We have shown that with HC-MOFs the ZDWs can take values well above that of SC-MOFs. In addition, by changing the pressure of the gas, the ZDW can be further tailored. We have studied the SCG and UV-light generation in HC-MOFs, in particular in the kagomé fibre. Using the results of pulse propagation simulations we have determined the coherence evolution, as well as the quality of the output pulse and the efficiency of UV light conversion. We have made several simulations in order to tune the UV light and to find output spectra with high efficiency and high quality. The propagation simulations can be useful for giving insight on how to build new UV light sources.

Then, we have focused on the electromagnetically induced transparency (EIT) effect. We have made a comparison between the EIT effect in a free gas and in the same gas confined in a HC-MOF. The middle window of a typical EIT graph shows transparencies as high as 100%, and whose transparency depends on several parameters of the system: the atoms /molecules density, the atomic dipolar moments of pump and probe transitions, the power of the pump laser, the detuning of each laser, the temperatures, and the decay rates between different levels. We have studied the impact of varying several parameters of a system with the EIT effect. We have made an important study of the EIT effect in HC-MOFs. The transverse spatial profile of the pump inside the HC-MOF produces a refractive index for the probe that varies along the radial coordinate. Thus, we have observed that the resultant transmission in a HC-MOF has a complex dependence on the distribution of the pump laser field. In addition, we have observed how the temperature effect affects these phenomena.

6.2 Future perspectives

Following to work presented in this thesis, it would be interesting to study some other related subjects:

– to study HC-MOFs filled with liquids, different gases, or plasmas;

– to study the photonic bands of kagomé fibres in more detail, namely to analyse the DOS and evaluate the properties around each k-point;

– to extend our EIT numerical studies in HC-fibres to different fibres;

– to simulate the light propagation on HC-MOFs in the presence of EIT;

– to investigate the occurrence of nonlinear phenomena with Feynman diagrams; however that is computationally too much intensive for the hardware of current computers;

– to evaluate the possibility of usage of a generalized eikonal approximation for studies of light propagation in MOFs;

– to study participation media that have inhomogeneous index of refraction confined in HC-MOFs using scattering techniques inspired on: photon mapping, metropolis light transport, or path tracing.

A

APPENDIX: ADDITIONAL FORMULAS

A.1 Nonlinear wave equation

By taking the curl of Eq. (2.9), then identifying the relation to the time-derivative of the 1st term of Eq. (2.10), and using the vector identity $\nabla \times \nabla \times \vec{v} = \nabla(\nabla.\vec{v}) - \nabla^2\vec{v}$, we obtain:

$$\begin{aligned} \nabla(\nabla.\mathbf{E}) - \nabla^2\mathbf{E} &= \nabla \times \left(-\frac{\partial \mathbf{B}}{\partial t}\right) \\ &= -\frac{\partial}{\partial t}\left(\mu\left(\mathbf{J} + \frac{\partial \mathbf{D}}{\partial t}\right)\right) \\ &\approx -\frac{1}{\epsilon_0 c^2}\frac{\partial^2}{\partial t^2}\mathbf{D} \\ &= -\frac{1}{\epsilon_0 c^2}\frac{\partial^2}{\partial t^2}[\epsilon_0 \mathcal{F}^{-1}\{\epsilon_r \tilde{\mathbf{E}}\} + \mathbf{P}_{NL}] \end{aligned} \tag{A.1}$$

where the approximation is that we have considered a medium free of charges and non-magnetic. Thus, we achieve Eq. (2.14).

The polarization effects are not instantaneous in time, and because of that we have to describe them in the Fourier domain, by $\mathcal{F}^{-1}\{\tilde{\epsilon}_r\tilde{\mathbf{E}}\}$, given by:

$$\mathcal{F}^{-1}\{\tilde{\epsilon}_r\tilde{\mathbf{E}}\} = \mathcal{F}^{-1}\{\mathcal{F}\{\epsilon_r * \mathbf{E}\}\} = \epsilon_r * \mathbf{E} \quad = \int_{-\infty}^{t} \epsilon_r(\tau)\mathbf{E}(t-\tau)d\tau,$$

due to the time convolution theorem.

A.2 The master equation

We will prove here Eqs. (2.17)-(2.18). In a medium free of electrical charges and free of electrical currents, Eqs. (2.7)-(2.10) describe that system.

For monochromatic fields of frequency ω, in the Fourier domain we have:

$$\nabla \times \mathbf{E} - i\omega\mu_0\mathbf{H} = 0; \tag{A.2}$$

$$\nabla \times \mathbf{H} + i\omega\epsilon_0\epsilon_r\mathbf{E} = 0; \tag{A.3}$$

which leads to:

$$\Rightarrow \frac{1}{\epsilon_r(r)}\nabla \times \mathbf{H}(r) + i\omega\epsilon_0\mathbf{E}(r) = 0; \tag{A.4}$$

$$\Rightarrow \nabla \times \frac{1}{\epsilon_r(r)}\nabla \times \mathbf{H}(r) + i\omega\epsilon_0(i\omega\mu_0\mathbf{H}(r)) = 0; \tag{A.5}$$

$$\Rightarrow \nabla \times \frac{1}{n(r)^2}\nabla \times \mathbf{H}(r) - \frac{\omega^2}{c^2}\mathbf{H}(r) = 0; \tag{A.6}$$

where Eq. (A.6) leads to Eq. (2.17), that we wanted to prove.

A.3 The model for refractive index

In order to describe the refractive index of a medium we must analyse how the matter is affected by the light propagating on it. When an electric field propagates in a medium the valence electrons of the medium suffer a displacement that can be modelled as that of a classical spring. The valence electrons oscillate around their equilibrium position such that their equation of motion in the medium is:

$$m\frac{d^2}{dt^2}x(t) + m\zeta\frac{d}{dt}x(t) + kx(t) = qE(t), \tag{A.7}$$

where m is the mass of the electron, ζ is the damping coefficient, k is the coefficient of the restoring force (i.e. of the force between nucleus and the valence electron), $q = -e$ is the electron charge, and $E(t) = E_0e^{-i\omega t}$ is the external electric field.

The displacement function $x(t)$ is assumed to be of the form:

$$x(t) = x_0e^{-i\omega_0 t}, \tag{A.8}$$

because $x(t)$ changes periodically with the electrical field intensity. Substituting $x(t)$, and E(t) on Eq. (A.7) and introducing $\omega_0 = \sqrt{k/m}$, we obtain:

$$x_0 = q\frac{E_0}{m}\frac{1}{(\omega_0^2 - \omega^2 - i\omega\zeta)} \tag{A.9}$$

The dipolar moment of each dipole is:

$$p(t) = qx(t) = qx_0 e^{-i\omega_0 t}; \tag{A.10}$$

and the density of the polarization of the medium is:

$$\begin{aligned} p(t) &= lim_{\Delta v \to \delta}\frac{\sum_{j=1}^{n} q_j x_j(t)}{\Delta v} \\ &= nq^2/m \sum_j \frac{f_j}{\omega_j^2 - \omega^2 - i\omega\zeta_j} E(t), \end{aligned} \tag{A.11}$$

where n is the number of oscillators per unit volume and f_j is known as the oscillator strength of each resonant frequency w_j.

Far from resonances, the imaginary part can be neglected with $\zeta_j \approx 0$. Therefore, solving for $Re\{\chi\}$ we obtain:

$$Re\{\chi\} = \omega_p^2 \sum_j \frac{f_j}{\omega_j^2 - \omega^2}, \tag{A.12}$$

where $\omega_p = \sqrt{\frac{nq^2}{m\epsilon_0}}$.

After that, by substituting the frequencies we obtain:

$$\begin{aligned} Re\{\chi\} &= \omega_p^2 \sum_j \frac{f_j}{\left(\frac{2\pi c}{\lambda_j}\right)^2 - \left(\frac{2\pi c}{\lambda}\right)^2}. \\ &= \sum_j \frac{a_j \lambda^2}{\lambda^2 - b_j}, \end{aligned} \tag{A.13}$$

where a_j is the magnitude of the resonance with $\lambda_j^2 = b_j$.

The refractive index of the material is then given by:

$$\begin{aligned} n &= \sqrt{1 + \chi} \\ &= \sqrt{1 + \sum_j \frac{a_j \lambda^2}{\lambda^2 - b_j}}. \end{aligned} \tag{A.14}$$

This eq. is called the Sellmeier equation, whose coefficients are determined experimentally.

A.4 GNLSE with self-steepening

We will consider an electric-field described by:

$$E = f(x,y)a(z,t)e^{-i\omega_0 t + i\beta_c z} \rightarrow \tilde{E} = f(x,y)\tilde{a}(z,\omega-\omega_0)e^{i\beta_c z} \tag{A.15}$$

Using the wave equation in the Fourier domain we have:

$$\nabla^2\tilde{E} + \frac{\omega^2}{c^2}(1+\tilde{\chi}^{(1)}(\omega))\tilde{E} = \mu_0\mathcal{F}\left(\frac{\partial^2 P_{NL}}{\partial t^2}\right); \tag{A.16}$$

$$\nabla^2\tilde{E} + \frac{\omega^2}{c^2}(n^2+2n\Delta n)\tilde{E} = 0, \tag{A.17}$$

where Δn includes the nonlinear effects in a perturbative form. Therefore we can write down:

$$\tilde{a}\nabla_t^2 f e^{i\beta_c z} + f\left(\frac{\partial^2\tilde{a}}{\partial z^2} + 2i\beta_c\frac{\partial\tilde{a}}{\partial z} - \beta_c^2\tilde{a}\right)e^{i\beta_c z} + \frac{\omega^2}{c^2}(n^2+2n\Delta n)f\tilde{a}e^{i\beta_c z} = 0. \tag{A.18}$$

Then, dividing both sides by $\tilde{a}fe^{i\beta_c z}$, we obtain:

$$\frac{1}{f}\nabla_t^2 f + \frac{\omega^2}{c^2}(n^2+2n\Delta n) = -\frac{1}{\tilde{a}}\left(\frac{\partial^2\tilde{a}}{\partial z^2} + 2i\beta_c\frac{\partial\tilde{a}}{\partial z} - \beta_c^2\tilde{a}\right). \tag{A.19}$$

We can see that the left hand-side of this equation only depends on x and y, whereas the right hand-side of this equation only depends on z. Therefore we can equal each side of this equation to a constant, which we will call $\tilde{\beta}^2$.

Therefore we obtain two equations:
- the equation from the left hand-side is the equation for the transversal distribution of the field, giving the propagation modes, and propagation constants;
- the equation from the right hand-side is the evolution equation for the envelope depending on time.

Let us proceed with the equation from the right hand-side:

$$\frac{\partial^2\tilde{a}}{\partial z^2} + 2i\beta_c\frac{\partial\tilde{a}}{\partial z} + \left(\tilde{\beta}^2 - \beta_c^2\right)\tilde{a} = 0. \tag{A.20}$$

$$\Rightarrow \frac{\partial^2\tilde{a}}{\partial z^2} + 2i\beta_c\frac{\partial\tilde{a}}{\partial z} + \left((\beta+\Delta\beta)^2 - \beta_c^2\right)\tilde{a} = 0, \tag{A.21}$$

where the $\Delta\beta$ represents a perturbation given by [1]:

$$\Delta\beta = \frac{k_0\iint\Delta n|f(x,y)|^2dxdy}{\iint|f(x,y)|^2dxdy}, \tag{A.22}$$

Here we can replace β by its Taylor series, around ω_0:

$$\beta = \beta_c + \beta_c'(\omega - \omega_0) + \tilde{d}, \tag{A.23}$$

where $\tilde{d}$ represents the sum of the other terms of that Taylor series.

Therefore we have that:

$$\begin{aligned}&(\beta + \Delta\beta)^2 \\ &= (\beta_c + \beta_c'(\omega - \omega_0) + \tilde{d} + \Delta\beta)^2\end{aligned} \tag{A.24}$$

$= \beta_c^2 + 2\beta_c\beta_c'(\omega - \omega_0) + 2\beta_c\tilde{d} + 2\beta_c\Delta\beta + (\beta_c')^2(\omega - \omega_0)^2 + 2\beta_c'(\omega - \omega_0)\tilde{d} + 2\beta_c'(\omega - \omega_0)\Delta\beta + \tilde{d}^2 + 2\tilde{d}\Delta\beta + \Delta\beta + \Delta\beta^2$.

Then, by discarding the small terms, we obtain:

$$\frac{\partial^2\tilde{a}}{\partial z^2} + 2i\beta_c\frac{\partial\tilde{a}}{\partial z} + \left(2\beta_c\beta_c'(\omega - \omega_0) + 2\beta_c\tilde{d} + 2\beta_c\Delta\beta + (\beta_c')^2(\omega - \omega_0)^2 + 2\beta_c'(\omega - \omega_0)\tilde{d}\right)\tilde{a} = 0, \tag{A.25}$$

which can be expressed in the time-domain as:

$$\left(\frac{\partial^2 a}{\partial z^2} + 2i\beta_c\frac{\partial a}{\partial z} + 2i\beta_c\beta_c'\frac{\partial a}{\partial t} + 2\beta_c\sum_{n\geq 2}\frac{(-i)^n}{n!}\frac{\partial^n}{\partial t^n}a + 2\beta_c\Delta\beta a - (\beta_c')^2\frac{\partial^2 a}{\partial t^2} + 2\beta_c' i\frac{\partial}{\partial t}\sum_{n\geq 2}\frac{(-i)^n}{n!}\frac{\partial^n}{\partial t^n}a\right)e^{i\omega_0 t}$$

$= 0;$

(A.26)

or:

$$\frac{\partial^2 a}{\partial z^2} + 2i\beta_c\frac{\partial a}{\partial z} + 2i\beta_c\beta_c'\frac{\partial a}{\partial t} + 2\beta_c da + 2\beta_c\Delta\beta a - (\beta_c')^2\frac{\partial^2 a}{\partial t^2} + 2i\beta_c' d\frac{\partial a}{\partial t} = 0. \tag{A.27}$$

We now make a change of variable $\tau = t - \beta_c' z$, and we get:

$$\left[\frac{\partial^2}{\partial z^2} - 2\beta_c'\frac{\partial^2}{\partial z\partial\tau} + (\beta_c')^2\frac{\partial^2}{\partial\tau^2}\right]a + 2i\beta_c\left[\frac{\partial}{\partial z} - \beta_c'\frac{\partial}{\partial\tau}\right]a + 2i\beta_c\beta_c'\frac{\partial a}{\partial\tau} + 2\beta_c da - (\beta_c')^2\frac{\partial^2 a}{\partial\tau^2} + 2i\beta_c' d\frac{\partial a}{\partial\tau} \tag{A.28}$$

$$= -2\beta_c\Delta\beta a; \tag{A.29}$$

which can be simplified to:

$$\left[-2\beta_c'\frac{\partial^2}{\partial z\partial\tau}\right]a + 2i\beta_c\left[\frac{\partial}{\partial z}\right]a + 2\beta_c da + 2i\beta_c' d\frac{\partial a}{\partial\tau} = -2\beta_c\Delta\beta a, \tag{A.30}$$

if we use the slowly varying envelope approximation: $\frac{\partial^2}{\partial z^2}a \approx 0$.

After that we transform the last equation into:

$$2i\beta_c\frac{\partial}{\partial z}\left(1+\frac{i}{\omega_0}\frac{\partial}{\partial\tau}\right)a+2\beta_c\left(1+\frac{i}{\omega_0}\frac{\partial}{\partial\tau}\right)da=-2\beta_c\Delta\beta a. \tag{A.31}$$

where we have used that $\beta_c = n_{\text{eff}}\omega_0/c \Rightarrow \beta_c' \approx n_{\text{eff}}/c$.

Then we will treat the nonlinear perturbative term. We consider that:

$$P_{NL}=\frac{3}{4}\epsilon_0\chi^{(3)}E\int R(t')|E(t-t')|^2dt'. \tag{A.32}$$

with:

$$\frac{\omega^2}{c^2}2n\Delta n=-\mu_0\mathcal{F}\left\{\frac{\partial^2}{\partial t^2}P_{NL}\right\}/(afe^{i\beta_c z}); \tag{A.33}$$

$$\Rightarrow \Delta n=\frac{3}{8n}\chi^{(3)}|f|^2\left(\left(1+\frac{i}{\omega_0}\frac{\partial}{\partial t}\right)^2\right)\int R(t')|a(t-t')|^2dt'. \tag{A.34}$$

We can now substitute Eq. (A.34) into Eq. (A.22), obtaining that:

$$\Delta\beta=\frac{k_0 3\chi^{(3)}}{8n}\frac{\iint|f|^4dxdy}{\iint|f|^2dxdy}\left(1+\frac{i}{\omega_0}\frac{\partial}{\partial t}\right)^2\int R(t')|a(t-t')|^2dt'; \tag{A.35}$$

after that, inserting this result in Eq. (A.30), and simplifying we obtain:

$$\frac{\partial a}{\partial z}-ida=i\frac{k_0 3\chi^{(3)}}{8n}\frac{\iint|f|^4dxdy}{\iint|f|^2dxdy}\left(1+\frac{i}{\omega_0}\frac{\partial}{\partial t}\right)\int R(t')|a(t-t')|^2dt'a. \tag{A.36}$$

Then, we make the substitution $u = ba$, with $b=\sqrt{\frac{1}{2}\epsilon_0 cn\iint|f(r,\phi)|^2rdrd\phi}$, such that:

$$\frac{\partial u/b}{\partial z}-idu/b=i\frac{k_0 3\chi^{(3)}}{8n}\frac{1}{a_{\text{eff}}}\left(1+\frac{i}{\omega_0}\frac{\partial}{\partial t}\right)\int R(t')\frac{|u(t-t')|^2}{|1/2\epsilon_0 cn|}dt'u/b; \tag{A.37}$$

$$\frac{\partial u}{\partial z}-idu=i\gamma\left(1+\frac{i}{\omega_0}\frac{\partial}{\partial t}\right)\int R(t')|u(t-t')|^2dt'u, \tag{A.38}$$

which is the GNLSE with self-steepening, where:

$$\gamma=\frac{k_0 3\chi^{(3)}}{4n^2\epsilon_0 ca_{\text{eff}}}. \tag{A.39}$$

Here, by using the Kerr coefficient given by [1]:

$$n_2^I=2n_2/(\epsilon_0 cn)=\frac{3}{4}\frac{\chi^{(3)}}{n^2\epsilon_0 c}, \tag{A.40}$$

the expression on Eq. (A.39) is in agreement with Eq. (2.25), for nonlinear parameter, γ.

A.5 The primitive and reciprocal lattice vectors

In order to derive the theoretical formula for building the primitive reciprocal lattice vectors [54], we start by looking at the functions that are periodic, which are described by:

$$f(r) = f(\mathbf{r} + \mathbf{r}_t), \tag{A.41}$$

where $\mathbf{r}$ is any point in the primitive space, and $\mathbf{r}_t$ is a translation vector that translates the lattice into itself. Then, we must apply the condition of the periodicity to the Fourier transforms of these functions, $\tilde{f}(\mathbf{r}) = \tilde{f}(\mathbf{r} + \mathbf{r}_t)$, that yields:

$$\int g(\mathbf{q}) e^{i\mathbf{q}.\mathbf{r}} d^3q = \int g(\mathbf{q}) e^{i\mathbf{q}.(\mathbf{r}+\mathbf{r}_t)} d^3q, \tag{A.42}$$

where $\mathbf{q}$ stands for all the wave-vectors, and $g(\mathbf{q})$ is the coefficient of the wave-vector $\mathbf{q}$. From this we have:

$$e^{i\mathbf{q}.\mathbf{r}_t} = 1 \tag{A.43}$$

$$\Rightarrow \mathbf{q}.\mathbf{r}_t = 2\pi n_c,$$

with n_c an integer constant.

The vectors $\mathbf{q}$ for such that this condition is satisfied are called the reciprocal lattice vectors. For a 3d space we would have:

$$\mathbf{q}.r_t = (la_1 + ma_2 + na_3).(lb_1 + mb_2 + nb_3) = 2\pi n_c \tag{A.44}$$

where $\mathbf{a}_i$ are the primitive vectors of the lattice and $\mathbf{b}_j$ are the primitive vectors of the reciprocal lattice. We can satisfy the above condition for some n_c. The preferred solution is such that the value of n_c is equal to the dimension number of the system, with:

$$a_i.b_j = 2\pi\delta_{ij}, \tag{A.45}$$

where δ_{ij} is the Kronecker delta. It can be proven that, if we know all a_i, then by solving Eq. (A.44) for finding all b_j for 2-dimensions (or 3-dimensions) we obtain that:

- the vectors b_j are such that the 2x2 (or 3x3) matrix whose columns are b_j is 2π times the inverse of the transpose of the matrix whose columns are a_i. [54]

For instance, in the case of a 2-dimensional hexagonal lattice, which has $\mathbf{a}_1 = \left(\frac{\sqrt{3}}{2}, \frac{1}{2}\right)$, and $\mathbf{a}_2 = \left(\frac{\sqrt{3}}{2}, -\frac{1}{2}\right)$, we have:

$$2\pi\left(\begin{bmatrix} \frac{\sqrt{3}}{2} & \frac{\sqrt{3}}{2} \\ \frac{1}{2} & \frac{-1}{2} \end{bmatrix}^T\right)^{-1} \underset{\text{normalized}}{=} \begin{bmatrix} \frac{1}{2} & \frac{1}{2} \\ \frac{\sqrt{3}}{2} & \frac{-\sqrt{3}}{2} \end{bmatrix}.$$

Thus, according to the above result, for the considered hexagonal geometry, $b_1 = \left(\frac{1}{2}, \frac{\sqrt{3}}{2}\right)$, and $b_2 = \left(\frac{1}{2}, -\frac{\sqrt{3}}{2}\right)$.

B

APPENDIX: FLOW CHARTS

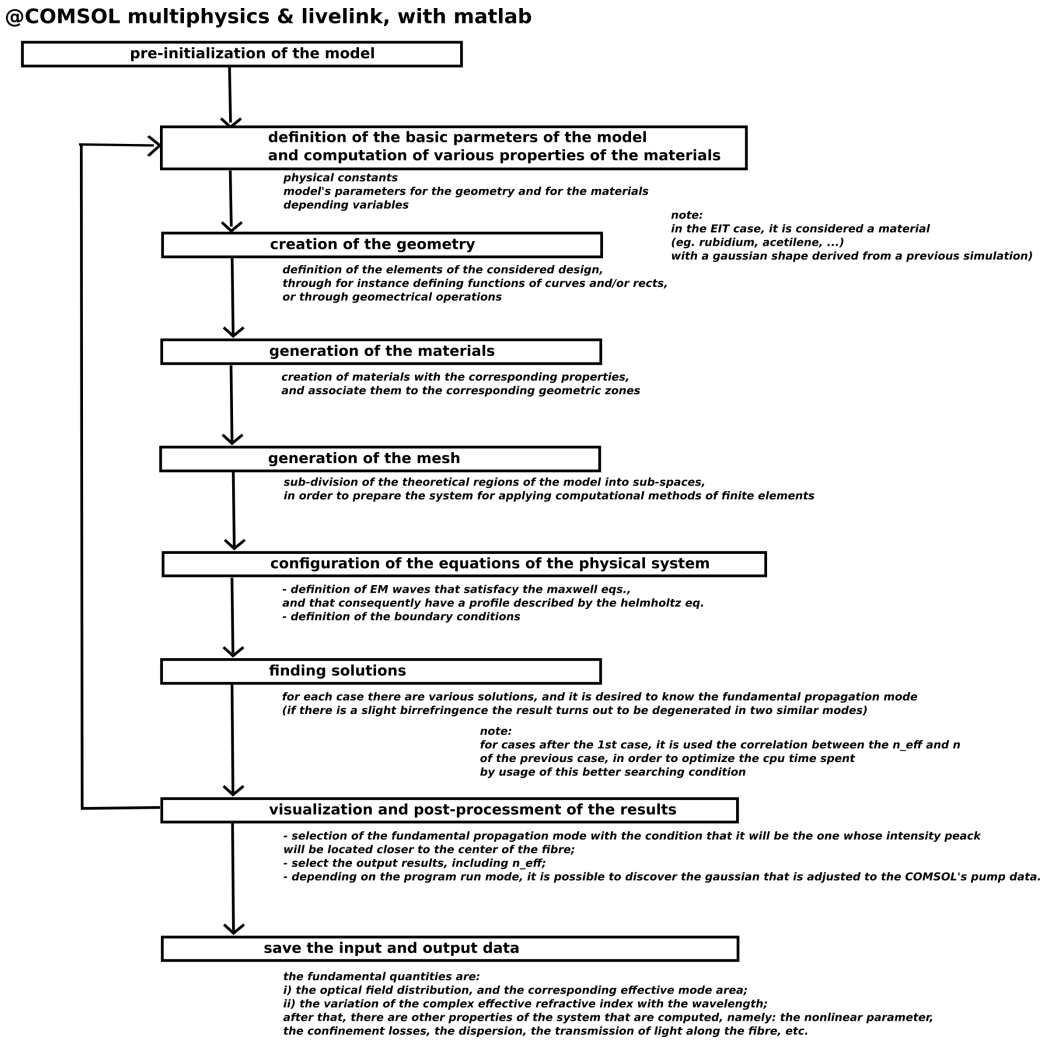

Fig. B.1: Flow chart for the code developed with Comsol multiphysics and livelink TM, and Matlab, for obtaining the propagation modes and their properties.

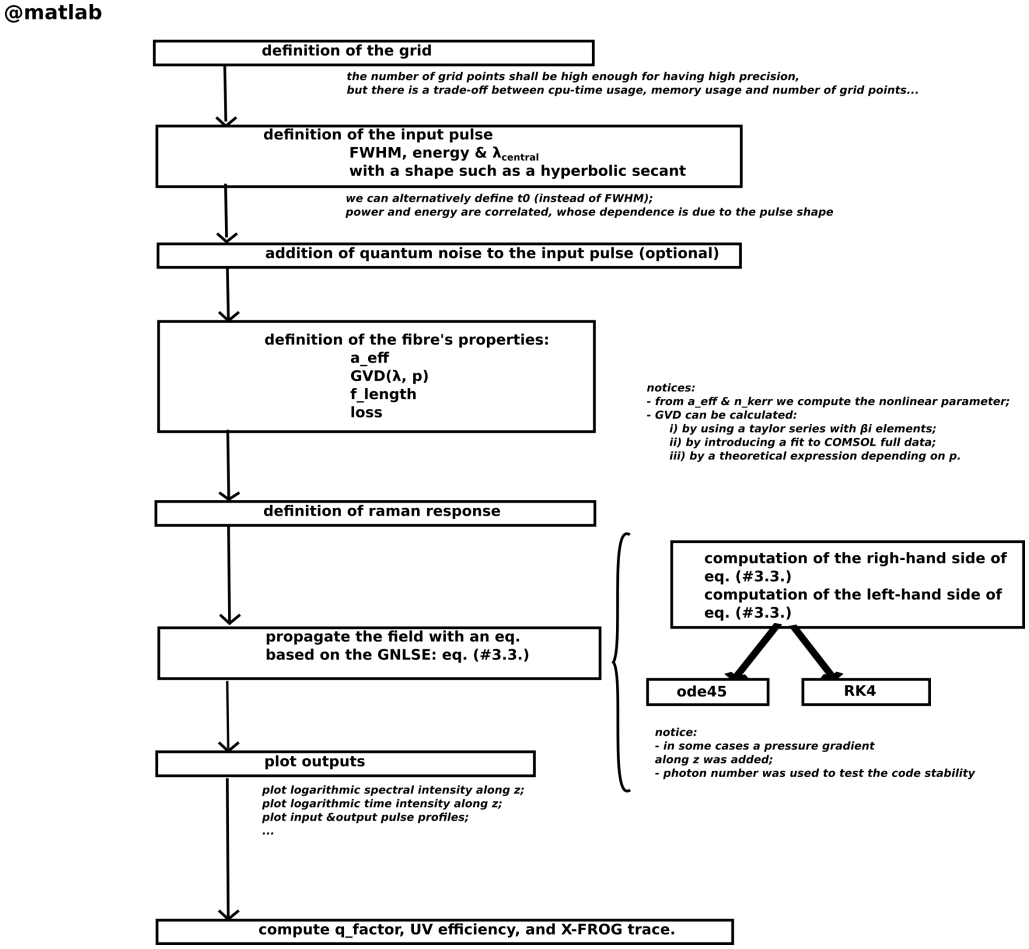

Fig. B.2: Flow chart for the beam propagation code developed in Matlab (and C++), for solving the GNLSE.

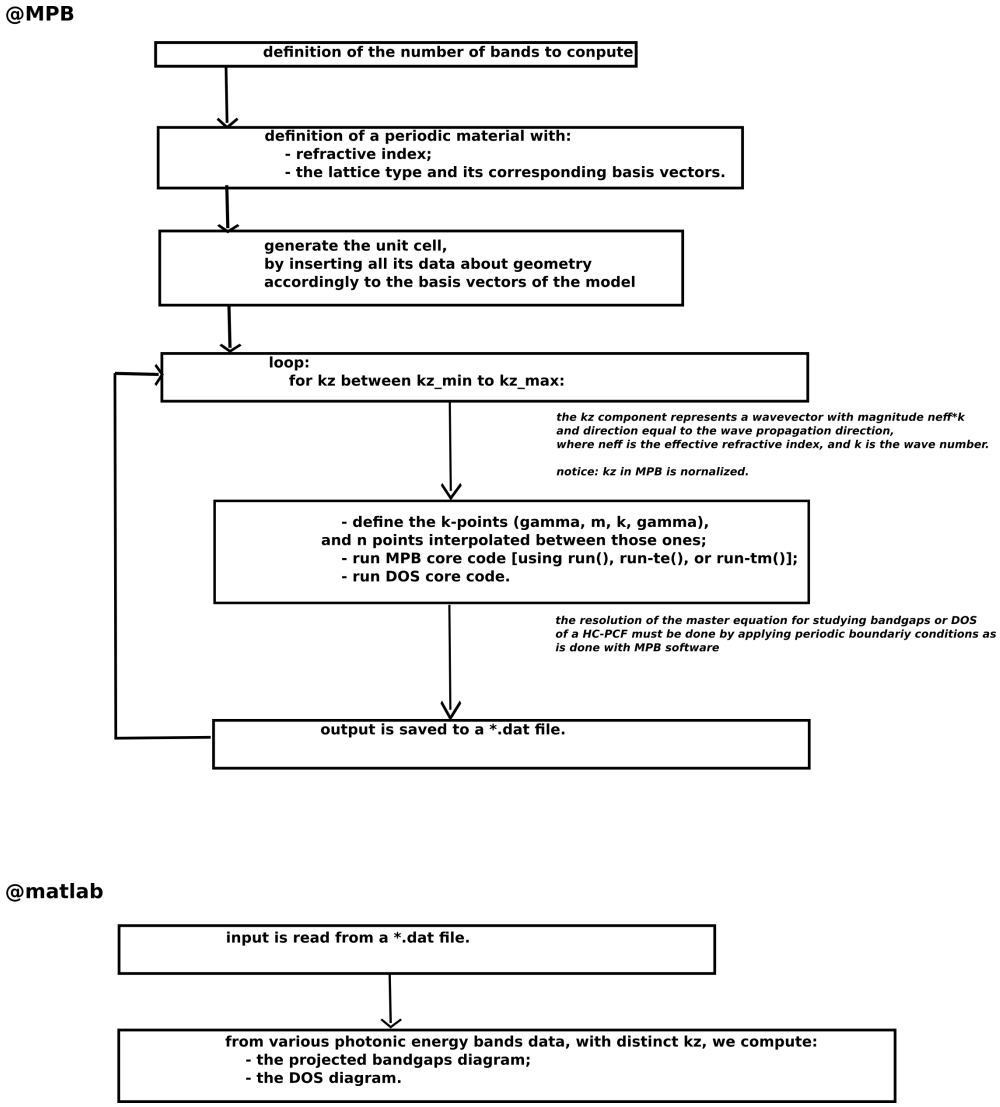

Fig. B.3: Flow chart for the code developed with MIT photonic bands (MPB), and Matlab, for computing the bands, projected bands and DOS of the claddings of HC-MOFs.

BIBLIOGRAPHY

[1] Agrawal, G. P. *Nonlinear fiber optics.* Academic Press; 3rd edition, 2001.

[2] Ainslie, B., and Day, C. A review of single-mode fibers with modified dispersion characteristics. *Journal of Lightwave Technology vol. 4*, 8 (1986), pp. 967–979.

[3] Akhmediev, N., and Karlsson, M. Cherenkov radiation emitted by solitons in optical fibers. *Phys. Rev. A vol. 51*, 3 (1995), pp. 2602–2607.

[4] Azhar, M., Wong, G. K., Chang, W., Joly, N. Y., and Russell, P. S. Raman-free nonlinear optical effects in high pressure gas-filled hollow core pcf. *Opt Express vol. 21*, 4 (2013), pp. 4405–4410.

[5] Barrientos-García, A., Sukhoivanov, I. A., Andrade-Lucio, J. A., Hernandez-Garcia, J. C., Ramos-Ortiz, G., Ibarra-Manzano, O. G., and Guryev, I. V. Numerical analysis of supercontinuum generation in photonic-crystal fibers with zero dispersion wavelengths in telecommunication windows. *Optik vol. 127*, 22 (2016), pp. 10981–10990.

[6] Benabid, F. Hollow-core photonic bandgap fibre: new light guidance for new science and technology. *Phil. Trans. R. Soc. A vol. 364*, 1849 (2006), pp. 3439–3462.

[7] Benabid, F., Knight, J. C., Antonopoulos, G., and Russell, P. S. J. Stimulated raman scattering in hydrogen-filled hollow-core photonic crystal fiber. *Science vol. 298* (2002), pp. 399–402.

[8] Bhagwat, A. R., and Gaeta, A. L. Nonlinear optics in hollow-core photonic bandgap fibers. *Opt. Express vol. 16*, 7 (2008), pp. 5035–5047.

[9] Bjarklev, A., Broeng, J., and Bjarklev, A. S. *Photonic crystal fibres*. Springer; 1st edition, 2003.

[10] Boller, K. J., Imamoglu, A., and Harris, S. E. Observation of electromagnetically induced transparency. *Phys. Rev. Lett. vol. 66*, 20 (1991), pp. 2593–2596.

[11] Boyd, R. W. *Nonlinear optics*. Academic Press; 3rd edition, 2008.

[12] Broeng, J., Mogilevstev, D., Barkou, S. E., and Bjarklev, A. Photonic crystal fibers: a new class of optical waveguides. *Optical Fiber Technology vol. 5*, 3 (1999), pp. 305–330.

[13] Browneester, D., Ekert, A. K., and Zeilinger, A. *The physics of quantum information: quantum cryptography, teleportation and quantum computation*. Springer, 2000.

[14] Brée, C. *Nonlinear optics in the filamentation regime*. PhD thesis, Springer Theses (recognizing outstanding Ph.D. research), Humboldt University of Berlin, Germany, 2012.

[15] Börzsönyi, A., Heiner, Z., Kalashnikov, M. P., Kovács, A. P., and Osvay, K. Dispersion measurement of inert gases and gas mixtures at 800 nm. *Applied Optics vol. 47* (2008), pp. 4856–4863.

[16] Börzsönyi, A., Heiner, Z., Kovács, A. P., Kalashnikov, M. P., and Osvay, K. Measurement of pressure dependent nonlinear refractive index of inert gases. *Opt. Express vol. 18*, 25 (2010), pp. 25847–25854.

[17] Carusotto, I., and Ciuti, C. Quantum fluids of light. *Rev. Mod. Phys. vol. 85*, 1 (2013), pp. 299–366.

[18] Chang, D. E., Vuletić, V., and Lukin, M. D. Quantum nonlinear optics — photon by photon. *Nature Photonics vol. 8*, 9 (2014), pp. 685–694.

[19] Cohen, L. G., Lin, C., and French, W. G. Tailoring zero chromatic dispersion into the 1.5–1.6μm low-loss spectral region of single-mode fibres. *Electron. Lett. vol. 15*, 12 (1979), pp. 334–335.

[20] Correa, R. A. *Development of hollow-core photonic bandgap fibres free of surface modes*. PhD thesis.

[21] Crisp, J., and Elliott, B. *Introduction to fiber optics.* Newnes; 3rd edition, 2005.

[22] Domachuk, P., Wolchover, N. A., Cronin-Golomb, M., A. Wang, A. K., George, Cordeiro, C. M. B., Knight, J. C., and Omenetto, F. G. Over 4000 nm bandwidth of mid-ir supercontinuum generation in sub-centimetre segments of highly nonlinear tellurite pcfs. *Optics Express vol. 16*, 10 (2008), pp. 7161–7168.

[23] Dong, L., Thomas, B. K., and Fu, L. Highly nonlinear silica suspended core fibers. *Optics Express vol. 16*, 12 (2008), pp. 16423–16430.

[24] Dudley, J. M., and Coen, S. Numerical simulations and coherence properties of supercontinuum generation. *IEEE Journal of selected topics in quantum electronics vol. 8*, 3 (2002), pp. 651–659.

[25] Dudley, J. M., Genty, G., and Coen, S. Supercontinuum generation in photonic crystal fiber. *Reviews of Modern Physics vol. 78*, 4 (2006), pp. 1135–1184.

[26] Dudley, J. M., and Taylor, J. R. *Supercontinuum generation in optical fibers.* Cambridge University Press; 1st edition, 2010.

[27] Ebendorff-Heidepriem, H., Petropoulos, P., Asimadis, S., and Finazzi, V. Bismuth glass holey fibers with high nonlinearity. *Opt. Express vol. 12*, 0 (2002), pp. 5082–5087.

[28] Ebendorff-Heidepriem, H., Petropoulos, P., Asimakis, S., Finazzi, V., Moore, R. C., Frampton, K., Koizumi, F., Richardson, D. J., and Monro, T. M. Bismuth glass holey fibers with high nonlinearity. *Optics Express vol. 12*, 21 (2004), pp. 5082–5087.

[29] $editor - in - chief$ M. Bass et al. *Handbook of optics.* McGraw-Hill; 3rd edition, 2009.

[30] Ermolov, A., Mak, K. F., Frosz, M. H., Travers, J. C., and Russell, P. S. J. Supercontinuum generation in the vacuum ultraviolet through dispersive-wave and soliton-plasma interaction in a noble-gas-filled hollow-core photonic crystal fiber. *Phys. Rev. A vol. 92*, 0 (2015), pp. 033821.

[31] Ferreira, M. F. S. *Nonlinear effects in optical fibers.* John Wiley & Sons - OSA; 1st edition, 2011.

[32] Field, J. E., Hahn, K. H., and Harris, S. E. Observation of electromagnetically induced transparency in collisionally broadened lead vapor. *Phys. Rev. Lett. vol. 67*, 22 (1991), pp. 3062.

[33] Finazzi, V., Monro, T. M., and Richardson, D. J. Small-core silica holey fibers: nonlinearity and confinement loss trade-offs. *J. Opt. Soc. Am. B vol. 20*, 7 (2003), pp. 1427–1436.

[34] Fleischhauer, M., Imamoglu, A., and Marangos, J. P. Electromagnetically induced transparency: optics in coherent media. *Rev. Mod. Phys. vol. 77*, 2 (2005), pp. 633.

[35] Foster, M., Moll, K., and Gaeta, A. Optimal waveguide dimensions for nonlinear interactions. *Opt. Express vol. 12*, 0 (2004), pp. 2880–2887.

[36] Gao, W., Amraoui, M. E., Liao, M., Kawashima, H., Duan, Z., Deng, D., Cheng, T., Suzuki, T., Messaddeq, Y., and Ohishi, Y. Mid-infrared supercontinuum generation in a suspended-core as2s3 chalcogenide microstructured optical fiber. *Optics Express vol. 21*, 8 (2013), pp. 9573–9583.

[37] Garcia-Adeva, A. Band gap atlas for photonic crystals having the symmetry of the kagomé and pyrochlore lattices. *New J. Phys. vol. 8*, 6 (2006), pp. 86.

[38] Ghosh, S., Bhagwat, A. R., Renshaw, C. K., Goh, S., Gaeta, A. L., and Kirby, B. J. Low-light-level optical interactions with rubidium vapor in a photonic band-gap fiber. *Phys. Rev. Lett. vol. 97*, 2 (2006), 023603.

[39] Granzow, N., Schmidt, M. A., Chang, W., Wang, L., Coulombier, Q., Troles, J., Toupin, P., Hartl, I., Lee, K. F., Fermann, M. E., Wondraczek, L., and Russell, P. S. J. Mid-infrared supercontinuum generation in as2s3-silica "nano-spike" step-index waveguide. *Optics Express vol. 21*, 9 (2013), pp. 10969–10977.

[40] Granzow, N., Stark, S. P., Schmidt, M. A., Tverjanovich, A. S., Wondraczek, L., and Russell, P. S. J. Supercontinuum generation in chalcogenide-silica step-index fibers. *Optics Express vol. 19*, 21 (2011), pp. 21003–21010.

[41] Han, X., You, C., Dai, S., Zhang, P., Wang, Y., Guo, F., Xu, D., Luo, B., Xu, P., and Wang, X. Mid-infrared supercontinuum generation in a three-hole

ge20sb15se65 chalcogenide suspended-core fiber. *Optical Fiber Technology vol. 34*, 0 (2017), pp. 74–79.

[42] Harbold, J. M., Ilday, F. O., Wise, F. W., Sanghera, J. S., Nguyen, V. Q., Shaw, L. B., and Aggarwal, I. D. Highly nonlinear as–s–se glasses for all-optical switching. *Optics Letters vol. 27*, 2 (2002), pp. 119–121.

[43] Harris, S. E. Electromagnetically induced transparency. *Phys. Today vol. 50*, 7 (1997), pp. 36.

[44] Harris, S. E., Field, J. E., and Imamoglu, A. Nonlinear optical processes using electromagnetically induced transparency. *Phys. Rev. Lett. vol. 64* (1990), pp. 1107.

[45] Harris, S. E., and Hau, L. V. Nonlinear optics at low light levels. *Phys. Rev. Lett. 82* (1999), 4611–4614.

[46] Hasegawa, A., and Kodama, Y. *Solitons in optical communications.* Oxford University Press, 1995.

[47] Hasegawa, A., and Tappert, F. Transmission of stationary nonlinear optical pulses in dispersive dielectric fibers. i. anomalous dispersion. *Appl. Phys. Lett. vol. 23*, 3 (1973), pp. 142–144.

[48] Hecht, J. *City of light: the story of fiber optics.* Oxford University Press, 1999.

[49] Holzer, P., Chang, W., Travers, J. C., Nazarkin, A., Nold, J., Joly, N. Y., Saleh, M., Biancalana, F., and Russel, P. S. J. Femtosecond nonlinear fiber optics in the ionization regime. *Phys. Rev. Lett. vol. 107*, 20 (2011), pp. 203901.

[50] Hopkins, S. A., Usadi, E., Chen, H. X., and Durrant, A. V. Electromagnetically induced transparency of laser-cooled rubidium atoms in three-level Λ-type systems. *Optics Communications vol. 138* (1997), pp. 185–192.

[51] Hölzer, P. *Nonlinear fiber optics in gases and dilute plasmas.* PhD thesis, MPL: Max-Plank-Institute für die Physik des Lichts, 2012.

[52] Im, S. J., Husakou, A., and Herrmann, J. Guiding properties and dispersion control of kagome lattice hollow-core photonic crystal fibers. *Optics Express vol. 17*, 15 (2009), pp. 13050–13058.

[53] Ippen, E. P. Low-power quasi-cw raman oscillator. *Appl. Phys. Lett. vol. 16* (1970), pp. 303–305.

[54] Joannopoulos, J. D., Johnson, S. G., Winn, J. N., and Meade, R. D. *Photonic crystals: molding the flow of light.* Princeton University Press, 2nd edition, 2008.

[55] John, S. Strong localization of photons in certain disordered dielectric superlattices. *Phys. Rev. Lett. vol. 58*, 23 (1987), pp. 2486–2489.

[56] Kao, K. C., and Hockham, G. A. Dielectric-fibre surface waveguides for optical frequencies. *Proceedings of the IEE vol. 113*, 7 (1966), pp. 1151–1158.

[57] Kasapi, A., Jain, M., Yin, G. Y., and Harris, S. E. Electromagnetically induced transparency: propagation dynamics. *Phys. Rev. Lett. vol. 74* (1995), pp. 2447.

[58] Khurgin, J. B., and Tucker, R. S. *Slow light: science and applications.* CRC Press, 2008.

[59] Knight, J. C. Photonic crystal fibres. *Nature vol. 424* (2003), pp. 847–851.

[60] Knight, J. C., Birks, T. A., Russell, P. S. J., and de Sandro, J. P. Properties of photonic crystal fiber and the effective index model. *JOSA A vol. 15*, 3 (1998), pp. 748–752.

[61] Knight, J. C., Broeng, J., Birks, T. A., and Russell, P. S. J. Photonic band gap guidance in optical fibers. *Science vol. 282*, 5393 (1998), pp. 1476–1478.

[62] Kodama, Y., and Hasegawa, A. Nonlinear pulse propagation in a monomode dielectric waveguide. *IEEE J. Quant. Elect. vol. QE23*, 0 (1987), pp. 510–524.

[63] Kumar, V. V. R. K., George, A. K., Knight, J. C., and Russel, P. S. J. Tellurite photonic crystal fiber. *Opt. Express vol. 11*, 0 (2003), pp. 2641–2645.

[64] Kumar, V. V. R. K., George, A. K., Reeves, W. H., Knight, J. C., Russell, P. S. J., Omenetto, F. G., and Taylor, A. J. Extruded soft glass photonic crystal fiber for ultrabroad supercontinuum generation. *Opt. Express vol. 10*, 0 (2002), pp. 1520–1525.

[65] Larsen, T. T., and Bjarklev, A. Optical devices based on liquid crystal photonic bandgap fibres. *Opt. Express vol. 11*, 20 (2003), pp. 2589–2596.

[66] Leong, J. Y. Y., Petropoulos, P., Price, J. H. V., Ebendorff-Heidepriem, H., Asimakis, S., Moore, R. C., Frampton, K. E., Finazzi, V., Feng, X., Monro, T. M., and Richardson, D. J. High-nonlinearity dispersion-shifted lead-silicate holey fibers for efficient 1-μm pumped supercontinuum generation. *Journal of Lightwave Technology vol. 24*, 1 (2006), pp. 183–190.

[67] Lin, C., and Stolen, R. H. New nanosecond continuum for excitedstate spectroscopy. *Appl. Phys. Lett. vol. 28*, 4 (1976), pp. 216–218.

[68] Loudon, R. *The quantum theory of light.* Oxford University Press; 3rd edition, 2000.

[69] Lukin, M. D., and Imamoğlu, A. Controlling photons using electromagnetically induced transparency. *Nature vol. 413* (2001), pp. 273.

[70] Mak, K. F. *Nonlinear optical effects in gas-filled hollow-core photonic-crystal fibers.* PhD thesis, MPL: Max-Plank-Institute für die Physik des Lichts, 2014.

[71] Mak, K. F., Travers, J. C., Hölzer, P., Joly, N. Y., and Russell, P. S. J. Tunable vacuum-uv to visible ultrafast pulse source based on gas-filled kagome-pcf. *Optics Express vol. 21*, 9 (2013), pp. 10942–10953.

[72] Marangos, J. P. Topical review: electromagnetic induced transparency. *J. Mod. Optics vol. 45*, 3 (1998), pp. 471–503.

[73] Medjouri, A., Meraghni, E.-B., Hathroubi, H., Abed, D., Simohamed, L. M., and Ziane, O. Design of zblan photonic crystal fiber with nearly zero ultra-flattened chromatic dispersion for supercontinuum generation. *Optik - International Journal for Light and Electron Optics vol. 135*, 0 (2017), pp. 417–425.

[74] Meija, J., et al. Atomic weights of the elements, 2013 (iupac tech. rep.). *Pure and Applied Chemistry vol. 88*, 3 (2016), pp. 265–291.

[75] Mitschke, F. *Fiber optics: physics and technology.* Springer Verlag; 1st edition, 2009.

[76] Miya, T., Terunuma, Y., Hosaka, F., and Miyoshita, T. Ultimate low-loss single-mode fibre at 1. 55μm. *Electron. Lett. vol. 15*, 4 (1979), pp. 106–108.

[77] Mohr, P. J., and Taylor, B. N. CODATA recommended values of the fundamental physical constants: 2002. *Rev. Mod. Phys. vol. 77*, 1 (2005), pp. 1–107.

[78] Mollenauer, L. F., Stolen, R. H., and Gordon, J. P. Experimental observation of picosecond pulse narrowing and solitons in optical fibers. *Phys. Rev. Lett. vol. 45*, 13 (1980), pp. 1095–1098.

[79] Mouawad, O., Picot-Clémente, J., Amrani, F., Strutynski, C., Fatome, J., Kibler, B., Désévédavy, F., Gadret, G., Jules, J. C., Deng, D., Ohishi, Y., and Smektala, F. Multioctave midinfrared supercontinuum generation in suspended-core chalcogenide fibers. *Optics Letters vol. 39*, 9 (2014), pp. 2684–2687.

[80] Nagasaka, K., Liu, L., Tuan, T. H., Cheng, T., Matsumoto, M., Tezuka, H., Suzuki, T., and Ohishi, Y. Numerical investigation of highly coherent mid-infrared supercontinuum generation in chalcogenide double-clad fiber. *Optical Fiber Technology vol. 36*, 0 (2017), pp. 82–91.

[81] New, G. *Introduction to nonlinear optics.* Cambridge University Press; 1st edition, 2011.

[82] Okamoto, K. *Fundamentals of optical waveguides.* Academic Press; 2nd edition, 2005.

[83] Park, J., Kang, D. E., Paulson, B., Nazari, T., and Oh, K. Liquid core photonic crystal fiber with low-refractive-index liquids for optofluidic applications. *Opt. Express vol. 22*, 14 (2014), pp. 17320–17330.

[84] Patnaik, A. K., Liang, J. Q., and Hakuta, K. Slow light propagation in a thin optical fiber via electromagnetically induced transparency. *Phys. Rev. A vol. 66*, 6 (2002), pp. 063808.

[85] Pearce, G. J., Wiederhecker, G. S., Poulton, C. G., Burger, S., and Russell, P. S. J. Models for guidance in kagome-structured hollow-core photonic crystal fibres. *Opt. Express vol. 15*, 20 (2007), pp. 12680–12685.

[86] Petropoulos, P., Ebendorff-Heidepriem, H., Finazzi, V., Moore, R. C., Frampton, K., Richardson, D. J., and Monro, T. M. Highly nonlinear and anomalously dispersive lead silicate glass holey fibers. *Optics Express vol. 11*, 26 (2003), pp. 3568–3573.

[87] Phillips, D. F., Fleischhauer, A., Mair, A., Walsworth, R. L., and Lukin, M. D. Storage of light in atomic vapor. *Phys. Rev. Lett. 86* (2001), 783–786.

[88] Press, W. H., Teukolsky, S. A., Vetterling, W. T., and Flannery, B. P. *Numerical recipes in C++: the art of scientific computing*. Cambridge University Press; 2nd edition, 2002.

[89] Price, J. H. V., Monro, T. M., Ebendorff-Heidepriem, H., Poletti, F., Horak, P., Finazzi, V., Leong, J. Y. Y., Petropoulos, P., Flanagan, J. C., Brambilla, G., Feng, X., and Richardson, D. J. Mid-ir supercontinuum generation from nonsilica microstructured optical fibers. *IEEE Journal of Selected Topics in Quantum Electronics vol. 13*, 3 (2007), pp. 738–749.

[90] Purves, G. T. *Absorption and dispersion in atomic vapours: applications to interferometery*. PhD thesis, Dep. of Physics, University of Durham, 2006.

[91] Rodrigues, S., Facão, M., Latas, S., and Ferreira, M. Soliton related effects in supercontinuum generation. In *Solitons: interactions, theoretical and experimental challenges and perspectives*, M. Williams, Ed. Nova Publishers, 2013, ch. 4, pp. 135–154.

[92] Rodrigues, S. M., Facão, M. M., Latas, S. C., and Ferreira, M. F. Highly nonlinear layered spiral microstructured optical fiber. *Photonics and Nanostructures - Fundamentals and Applications vol. 11*, 3 (2013), pp. 226–233.

[93] Russell, P. S. J. Photonic-crystal fibers. *JLT vol. 24*, 12 (2006), pp. 4729–4749.

[94] Safavi-Naeini, A. H., Alegre, T. P. M., Chan, J., Eichenfield, M., Winger, M., Lin, Q., Hill, J. T., Chang, D. E., and Painter, O. Electromagnetically induced transparency and slow light with optomechanics. *Nature vol. 472* (2011), pp. 69–73.

[95] Saitoh, K., and Koshiba, M. Numerical modeling of photonic crystal fibers. *Journal of Lightwave Technology vol. 23*, 11 (2005), pp. 3580–3590.

[96] Sansonetti, J. E. Wavelengths, transition probabilities, and energy levels for the spectra of rubidium (Rb I through Rb XXXVII). *J. Phys. Chem. Ref. Data vol. 35*, 1 (2006), pp. 301–421.

[97] Saruwatari, M. All-optical signal processing for terabit/second optical transmission. *IEEE J. Sel. Top. Quantum Electron. vol. 6*, 6 (2000), pp. 1363–1374.

[98] Schliesser, A., Picqué, N., and Hänsch, T. W. Mid-infrared frequency combs. *Nature Photonics vol. 6*, 7 (2012), pp. 440–449.

[99] Serebryannikov, E. E., and Zheltikov, A. M. Ionization-induced effects in the soliton dynamics of high-peak-power femtosecond pulses in hollow photonic-crystal fibers. *Phys. Rev. A vol. 76*, 1 (2007), pp. 013820.

[100] Shen, Y. R. *The principles of nonlinear optics.* Wiley-Interscience; 1 edition, 2002.

[101] Smirnov, S. V., Ania-Castanon, J. D., Ellingham, T. J., Kobtsev, S. M., Kukarin, S., and Turitsyn, S. K. Optical spectral broadening and supercontinuum generation in telecom applications. *Optical Fiber Technology vol. 12*, 2 (2006), pp. 122–147.

[102] Soljacić, M., and Joannopoulos, J. D. Enhancement of nonlinear effects using photonic crystals. *Nature Materials vol. 3* (2004), pp. 211–219.

[103] Steck, D. A. Rubidium 87 d line data, online at http://steck.us/alkalidata (revision 2.1.4, 23 december 2010). Tech. rep.

[104] Su, J. J., and Yu, I. A. The study of coherence-induced phenomena using double-sided feynman diagrams. *Chinese journal of physics vol. 41*, 6 (2003), pp. 627–642.

[105] Swidersky, J. High-power mid-infrared supercontinuum sources: current status and future perspectives. *Progress in Quantum Electronics vol. 38*, 5 (2014), pp. 189–235.

[106] Tani, F. *Extreme nonlinear optics in gas-filled hollow-core fibres.* PhD thesis.

[107] Tatian, B. Fitting refractive-index data with the sellmeier dispersion formula. *Applied Optics vol. 23*, 24 (1984), pp. 4477–4485.

[108] Tipler, P. A., and Mosca, G. *Physics for scientists and engineers.* W.H. Freeman; 6th edition, 2007.

[109] Travers, J. C., Chang, W., Nold, J., Joly, N. Y., and Russel, P. S. J. Ultrafast nonlinear optics in gas-filled hollow-core photonic crystal fibers. *JOSA B vol. 28*, 12 (2011), pp. A11–A26.

[110] Trebino, R., and Kane, D. J. Using phase retrieval to measure the intensity and phase of ultrashort pulses: frequency-resolved optical gating. *J. Opt. Soc. Am. A vol. 10*, 5 (1993), pp. 1101–1111.

[111] Tyndall, J. On some phenomena connected with the motion of liquids. *Proc. R. Inst. vol. 1* (1854), pp. 446–448.

[112] Uranus, H. P., Hoekstra, H. J. W. M., and van, E. G. Modes of an endlessly single-mode photonic crystal fiber: a finite element investigation. In *Proc. of the 9th Annual Symp. IEEE/LEOS Benelux - 2004* (2004), pp. 311–314.

[113] Vieweg, M., Gissibl, T., Pricking, S., Kuhlmey, B. T., Wu, D. C., Eggleton, B. J., and Giessen, H. Ultrafast nonlinear optofluidics in selectively liquid-filled photonic crystal fibers. *Opt. Express vol. 18*, 24 (2010), pp. 25232–25240.

[114] Wang, D., Wu, J. Z., and Zhang, J. X. Optical control of light propagation in photonic crystal based on electromagnetically induced transparency. *Chin. Phys. B vol. 25*, 6 (2016), 064202.

[115] Wheeler, N. V., Light, P. S., Couny, F., and Benabid, F. EIT-based slow and fast light in an all-fiber system. *Proc. SPIE 7612, Advances in Slow and Fast Light III*, 0 (2010).

[116] Xie, S., Tani, F., Travers, J. C., Uebel, P., Caillaud, C., Troles, J., Schmidt, M. A., and Russell, P. S. J. As2s3–silica double-nanospike waveguide for mid-infrared supercontinuum generation. *Optics Letters vol. 39*, 17 (2014), pp. 5216–5219.

[117] Xiong, C., Magi, E., Luan, F., Dekker, S., Sanghera, J. S., Shaw, L. B., Aggarwal, I. D., and Eggleton, B. J. Raman response in chalcogenide as2s3 fiber. *14th Optoelectronics and Communications Conference* (2009).

[118] Yablonovitch, E. Inhibited spontaneous emission in solid-state physics and electronics. *Phys. Rev. Lett. vol. 58*, 20 (1987), pp. 2059–2062.

[119] Zolla, F., Renversez, G., Nicolet, Kuhlmey, Guenneau, and Felbacq, D. *Foundations of photonic crystal fibres*. Imperial College Press, 2005.

[120] (online). COMSOL multiphysics, user's guide v4.2: http://www.comsol.com.

[121] (online). MIT photonic bands (MPB) software, freely available at: http://ab-initio.mit.edu/wiki/index.php.

[122] (ONLINE). refractiveindex.info - refractive index database:
https://refractiveindex.info/?group=schott&material=sf57.